FORMAL BAYESIAN APPROACHES TO THE SENSE AND GRAPPA PARALLEL FMRI RECONSTRUCTION TECHNIQUES ALONG WITH THEIR COMBINATION

by

Chase Joseph Sakitis, M.S.

A Dissertation submitted to the Faculty of the Graduate School,
Marquette University,
in Partial Fulfillment of the Requirements for
the Degree of Doctor of Philosophy

Milwaukee, Wisconsin

May 2024

ABSTRACT
FORMAL BAYESIAN APPROACHES TO THE SENSE AND GRAPPA PARALLEL FMRI RECONSTRUCTION TECHNIQUES ALONG WITH THEIR COMBINATION

Chase Joseph Sakitis, M.S.

Marquette University, 2024

In fMRI, capturing cognitive temporal dynamics is dependent on how quickly volume brain images are acquired. The sampling time for an array of spatial frequencies to reconstruct an image is the limiting factor in the fMRI process. Parallel imaging techniques Sensitivity Encoding (SENSE), which operates in the image space domain, and GeneRalized Autocalibrating Partial Parallel Acquisition (GRAPPA), which operates in the spatial frequency domain, have been utilized to greatly reduced image acquisition time. In SENSE image reconstruction, coil sensitivities are estimated once from *a priori* calibration images and used as fixed "known" coil sensitivities for image reconstruction of every subsequent image. This technique utilizes complex-valued least squares estimation via the normal equations to estimate voxel values for the reconstructed image. This method can encounter difficulty in estimating voxel values when the SENSE design matrix is not well conditioned. In GRAPPA, localized weights are utilized to interpolate the missing lines of the subsampled spatial frequency (k-space) coil arrays. These weights are assessed from *a priori* calibration spatial frequency arrays and are applied to every point the fMRI time series. This dissertation introduces Bayesian approaches to both SENSE and GRAPPA where prior distributions for the unobserved parameters are assessed from the *a priori* calibration information. For SENSE, the unobserved parameters are the unaliased voxel, coil sensitivities, and image noise variance, and for GRAPPA, the unobserved parameters are the missing spatial frequencies, localized weights, and the k-space noise variance. These parameters are jointly estimated *a posteriori* via the Iterated Conditional Modes algorithm and Markov chain Monte Carlo using Gibbs sampling. In addition, variability estimates and hypothesis testing is possible. This dissertation also explores fusing the GRAPPA and SENSE reconstruction technique along with applying a Bayesian approach to this fused technique. The Bayesian reconstruction techniques utilize prior image information to reconstruct images from the posterior distributions. The traditional image reconstruction techniques and the Bayesian techniques are extensively evaluated using a simulation study and experimental fMRI data.

ACKNOWLEDGEMENT

Chase Joseph Sakitis, M.S.

I would like to express my deepest appreciation to my advisor, Dr. Daniel B. Rowe, for being a wondrous mentor. You have provided me the guidance and encouragement to not only attain the scholarly accomplishments that I have achieved, but also inspiring me in finding a path in life that I am happy to be on. This endeavor would not have been possible without your invaluable patience and feedback which I am extremely grateful for.

I would like to thank Dr. Mehdi Maadooliat for the advice and encouragement throughout my journey at Marquette. I am thankful for Dr. D. Andrew Brown for the help and support that you have given me throughout our collaboration. I would also like to thank Dr. Cheng-Han Yu and Dr. Iain P. Bruce for serving on my doctoral committee.

I owe my heartfelt thanks to my fiancé, Meghan Jacoby, for being by my side throughout this journey and providing endless support and understanding. I would like to thank my Mom and Dad for giving me reassurance and confidence in myself to get to where I am today. I am grateful for my lab partners, Ke Xu and John Bodenschatz, for offering tremendous support in working through research challenges and experiences. Finally, I would like to Dr. Mehdi Razzaghi. As my undergraduate mentor, you have always offered me remarkable advice and provided me the opportunity to begin scholarly journey that led to Marquette.

TABLE OF CONTENTS

LIST OF FIGURES

CHAPTER 1: Introduction

1.1 Background

Magnetic Resonance Imaging (MRI) is a type of medical imaging that creates internal anatomic body images using strong magnetic fields. Functional Magnetic Resonance Imaging (fMRI) was developed in the early 1990's as a technique to noninvasively observe the human brain in action without exogenous contrast agents (Bandettini et al., 1993). This procedure examines brain activity by detecting changes in the blood oxygenation using the blood-oxygen-level dependent (BOLD) contrast (Ogawa et al., 1990). When a neuron fires, the blood oxygenation changes in the proximity of the neuron and is thus a correlate for neuronal firing. In MRI, the machine does not directly measure the images. Measurements from the machine are arrays of complex-valued spatial frequencies called k-space (Kumar et al., 1975). These k-space arrays are then reconstructed into images using an inverse Fourier transform (IFT) producing brain images. The reconstructed brain images are made up of complex-valued voxels which contain the signal intensity (magnitude) and a measure of local magnetic field (phase) for each pixel in the image.

Since the k-space array is complex-valued, as depicted in Figure 1.1 (column 2), there is a real part (first row) and an imaginary part (second row). An inverse Fourier transform matrix is depicted in Figure 1.1 (column 1) to illustrate the pre-multiplication of the k-space array with a real part (first row) and an imaginary part (second row). The real part of the IFT matrix is a graphical depiction of the cosine waves at different frequencies, and the imaginary part of the IFT matrix is a graphical depiction of the sine waves at different frequencies. Then the transpose of an IFT, depicted in Figure 1.1 (column 3), is used to post-multiply k-space with a real part (first row) and an imaginary part (second row). This

results in a reconstructed image (column 4) with a real part (first row) and an imaginary part (second row). Since the magnitude (first row, column 5) and the phase (second row, column 5) of the reconstructed images are observed for fMRI analysis (Rowe and Logan, 2004; Rowe, 2005), they are also shown in Figure 1.1. Despite the phase images generally being discarded using only the magnitude images for fMRI analysis, the phase images are utilized for this research. Producing magnitude and phase images is simply a conversion to polar coordinates from Cartesian coordinates in the complex plane. Since the voxel values are complex-valued, it forms a vector on a complex plane with the real part indicating the length in the x-direction and the imaginary part indicating the length in the y-direction. Converting to polar coordinates would give us the magnitude (the length) and the phase (the angle) of the voxel vector. For this research, the concentration will be on Cartesian k-space sampling, with the conversion to polar coordinates used for image depiction purposes.

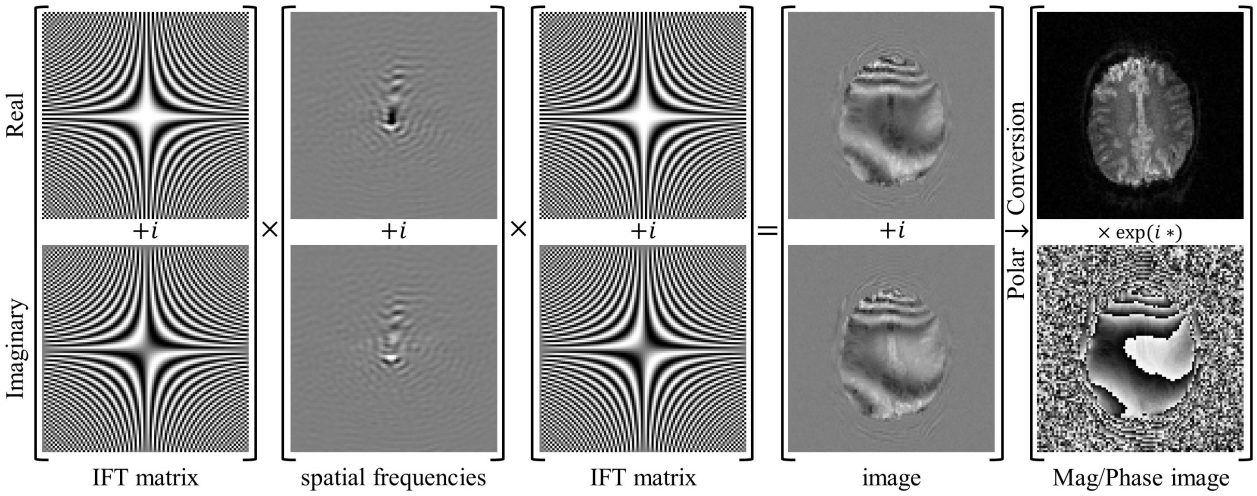

Figure 1.1: Inverse Fourier transform image reconstruction of a complex-valued k-space array to a complex-valued image (first and second row). Inverse Fourier transform image reconstruction of a complex-valued k-space array to a magnitude and phase image (third and fourth row).

In fMRI, obtaining hundreds of volume images is necessary to statistically detect activation in the brain. This series of observations are of the same underlying volume image taken over time with each image being measured individually through time. Measuring full arrays

of data for all slices required to form volume images takes a considerable amount of time due to the size of a dataset from a single experiment. For example, the experimental data used for this dissertation contain nine slices of 96×96 images with 510 time points yielding 41,472,000 complex-valued voxel values. Acquiring fully sampled k-space arrays limits the temporal resolution of the reconstructed images which can diminish the power of capturing brain activity.

Measuring full arrays of data for all the slices that form the volume image typically takes about one to two seconds, limiting the temporal resolution of the acquired images. The acquisition of k-space arrays to make up a volume image can take a considerable amount of time. A great deal of work has been dedicated to reducing the scan time of the fMRI process by accelerating the number of images acquired per unit of time. Hyde et al. (1986), Pruessmann et al. (1999), and Griswold et al. (2002) all explore parallel imaging techniques to reduce the scan time in MRI.

1.2 Previous Approaches

Historically, a single channel coil receiver has been utilized in fMRI to measure fully sampled k-space data arrays. The drawbacks of acquiring fully sampled k-space arrays directed fMRI research to increase the number of images acquired per unit of time. More recently, the focus of research has been to acquire more images per unit of time by measuring less data without losing the ability to form a full image. To accomplish this, multiple receiver coils are utilized in parallel to each measure spatial frequencies. With multiple receiver coils, we can skip lines in the acquisition of the k-space arrays which yields subsampled spatial frequency arrays for each coil. This subsampling reduces the acquisition time of the k-space arrays, but causes the images, after using the IFT, to be aliased, or appear "folded over," rendering them unusable. This requires the multiple aliased coil images to be unaliased and

combined into a single, full field-of-view (FOV) brain image.

There are two common parallel imaging techniques that accomplish this: SENSitivity Encoding (SENSE) (Pruessmann et al., 1999) and GeneRalized Autocalibrating Partial Parallel Acquisition (GRAPPA) (Griswold et al., 2002). SENSE operates in image space after the IFT utilizing estimated coil sensitivities (coil weightings) to unalias and combine the aliased coil measurements into a single FOV image. GRAPPA operates on the subsampled k-space prior to the IFT by estimating localized weights that are used to interpolate the unacquired spatial frequencies for each coil.

The SENSE method uses complex-valued linear regression with a fixed design matrix and a least squares solution to estimate the unknown parameters, which would be the voxel values of the single, full brain image. This approach for parameter estimation can be difficult because the complex-valued design matrix, generally, is ill-conditioned. This can cause aliasing artifacts, low image quality, and signal-to-noise ratio (SNR) degradation in the final reconstructed image, which has led to variations of the traditional technique (King and Angelos, 2001; Liang et al., 2001; Lin et al., 2004; Liu et al., 2009). These variations have deficiencies that hardly mitigate the limitations of the traditional maximum likelihood SENSE procedure. In Chapter 2, we develop a Bayesian approach to SENSE that will incorporate more prior information and does not use a single *a priori* fixed complex-valued sensitivity matrix, yielding increased SNR, no aliasing artifacts, and increased image quality with improved task detection results.

For the GRAPPA method, once the unacquired spatial frequencies are interpolated, the full k-space arrays (acquired plus estimated) for each coil are averaged to yield a single, full spatial frequency array. Then the averaged, full k-space array is inverse Fourier transformed into a full brain image. GRAPPA has its deficiencies, such as low image quality, a low SNR,

and diminished task detection power with higher acceleration factors. Also, since GRAPPA averages the full coil k-space arrays, this technique does not incorporate the sensitivities of the coils which results in a markedly lower overall signal intensity for each voxel. Bayesian methodologies have been utilized in k-space to improve spatial resolution and image quality (Kornak et al., 2010), but here we aim to reconstruct subsampled k-space data to produce full brain images. In Chapter 3, we develop a Bayesian approach to GRAPPA that will incorporate prior information, yielding increased SNR and image quality, with improved task detection power.

CHAPTER 2: Bayesian SENSE (BSENSE)

2.1 SENSE Technique

To motivate the proposed Bayesian approach, in this section we first consider single-coil full k-space inverse Fourier transform image reconstruction. Then the multi-coil fully sampled k-space IFT image reconstruction with SENSE image combination, and finally multi-coil subsampled k-space with SENSE image combination.

2.1.1 Single Coil, No Acceleration Factor

As mentioned in Section 1.2, fMRI historically utilized a single channel receiver coil as illustrated in Figure 2.1. With a single channel coil, the height of the receiver is taller than the size of the subject's head, shown in the three-dimensional depiction in Figure 2.1a. Both parts a and b of Figure 2.1 show the single coil receiver wraps completely around the subject's head starting from posterior to anterior and connects back at the posterior. The gray square with the red depicts the FOV of a single slice in both parts of Figure 2.1.

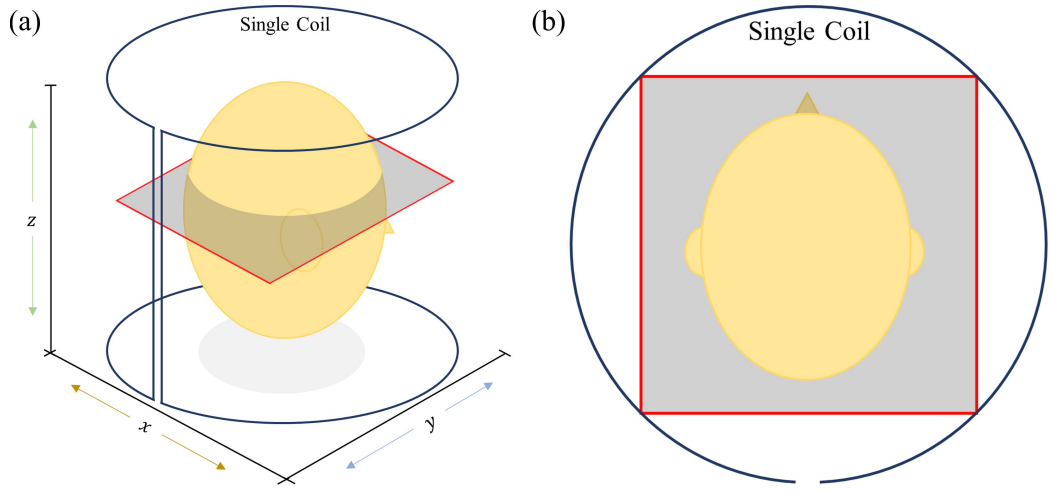

Figure 2.1: (a) Illustration of a three-dimensional single coil channel along with (b) the top-down view of the coil receiver.

From the single channel coil, the k-space arrays are acquired along a trajectory as shown in Figure 2.2 (top left) where the machine starts in the bottom left corner and moves across the row (in the x-direction) measuring complex-valued spatial frequencies along the Cartesian grid. At the end of each row, you move up one line (in the y-direction) and the process is repeated in the opposite direction. As the trajectory changes to move up one line in the y-direction, the machine continues to acquire the spatial frequency points outside the Cartesian grid called turnaround points. The acquisition of the complex-valued spatial frequencies continue until all the rows of the k-space array are obtained for each slice in the volume spatial frequency array. Then the turnaround points outside the square array are omitted yielding fully sampled k-space depicted in Figure 2.2 (top right). These complex-

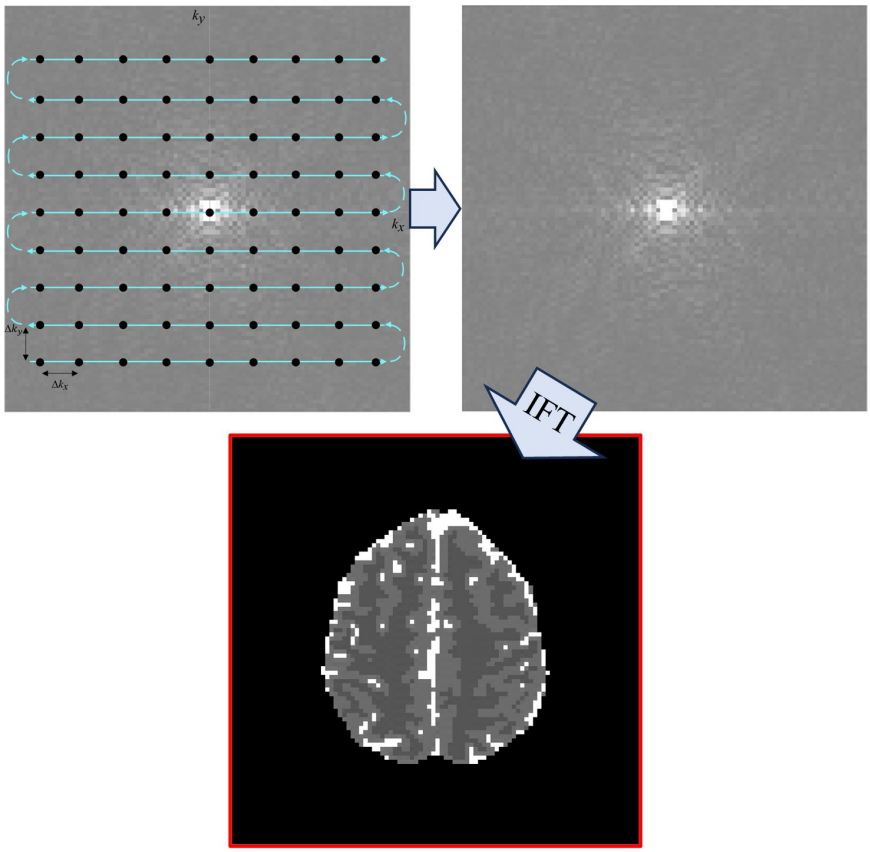

Figure 2.2: Fully sampled k-space zig-zag coverage (top left) with the finalized full k-space array after omitting the turn-around points (top right) and the reconstructed brain image using the IFT (bottom).

valued spatial frequency arrays are then reconstructed into full FOV real and imaginary then magnitude and phase brain images using the IFT (bottom of Figure 2.2). The reconstructed phase image is not illustratively shown.

2.1.2 Multi-Coil, No Acceleration Factor

To acquire more images per unit of time, $n_C > 1$ receiver coils are utilized instead of a single channel coil. An example of a four-channel coil arrangement is illustrated in Figure 2.3. The three-dimensional depiction of the multi-coil arrays in Figure 2.3a show the height of the receiver coils being taller than the head of the subject. In Figure 2.3b, starting with coil 1 at the anterior of the subject, the coils increment clockwise with coil 2 on the right lateral, coil 3 on the posterior, and coil 4 on the left lateral of the subject's head. Each of the four coils can measure full sampled k-space arrays, as exhibited in Figure 2.2, in parallel which does not increase the acquisition time compared to the single channel coil array.

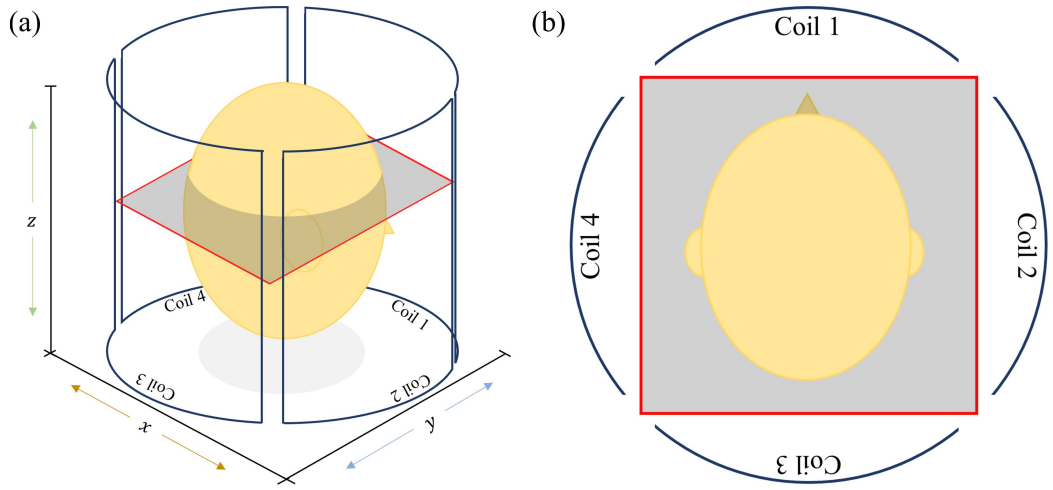

Figure 2.3: (a) Illustration of a three-dimensional multi-coil channel with four receivers along with (b) the top-down view of the multiple coils.

Each channel receiver coil possesses a depth sensitivity profile which depends on its size and location. This means that each coil can only "see" parts of the object with a particular depth sensitivity that decreases as we move farther from the coil. The same four-channel

coil configuration in Figure 2.3b is displayed in Figure 2.4 (center image with four coils on each side) showing how the coils would look around a single slice brain image. Figure 2.4 gives an illustrative example of image slices with $n_C = 4$ coils (top, bottom, left, right) and their respective depth sensitivity to the true image slice (the four corners of the figure). In Figure 2.4, the magenta outline of the brain can be seen in each coil sensitivity image (top, bottom, left, right) showing the placement of the true slice image in accordance with the coil. Typically, the sensitivities outside the brain are masked out but are left in Figure 2.4 to visualize how the depth sensitivity decreases for voxels the are further from the respective voxels. The images for Figure 2.4 are magnitude images used to visualize how the linear model is designed. In Figure 2.4, the top right corner image displays the true image point-wise multiplied by the depth sensitivity profile of coil 1 which is located at the front of the brain. The resulting image shows that the signal intensity of the image decreases as you move farther from the coil location towards the posterior of the brain (bottom of the top right image). When examining a single complex-valued voxel in the weighted brain image for coil 1, the complex-valued voxel from the true image (center) is multiplied by the complex-valued weighted sensitivity, S_{1c}, to get $a_{1c} = S_{1c}v_c + \varepsilon_{1c}$ with some additive measurement error. The other three coils follow the same operation creating the system of equations $a_c = S_c v_c + \varepsilon_c$ where $a_c \in \mathbb{C}^{n_C \times 1}$, $S_c \in \mathbb{C}^{n_C \times 1}$, $v_c \in \mathbb{C}^{1\times 1}$, and $\varepsilon_c \in \mathbb{C}^{n_C \times 1}$ as expressed in Eq. 2.1.

$$\begin{bmatrix} a_{1c} \\ a_{2c} \\ a_{3c} \\ a_{4c} \end{bmatrix} = \begin{bmatrix} S_{11c} \\ S_{21c} \\ S_{31c} \\ S_{41c} \end{bmatrix} \begin{bmatrix} v_c \end{bmatrix} + \begin{bmatrix} \varepsilon_{1c} \\ \varepsilon_{2c} \\ \varepsilon_{3c} \\ \varepsilon_{4c} \end{bmatrix}. \tag{2.1}$$

With this system of equations, a_c (the "aliased" voxel values in the corner images in Figure 2.4) are the observed measurements, after applying the IFT, from the machine that

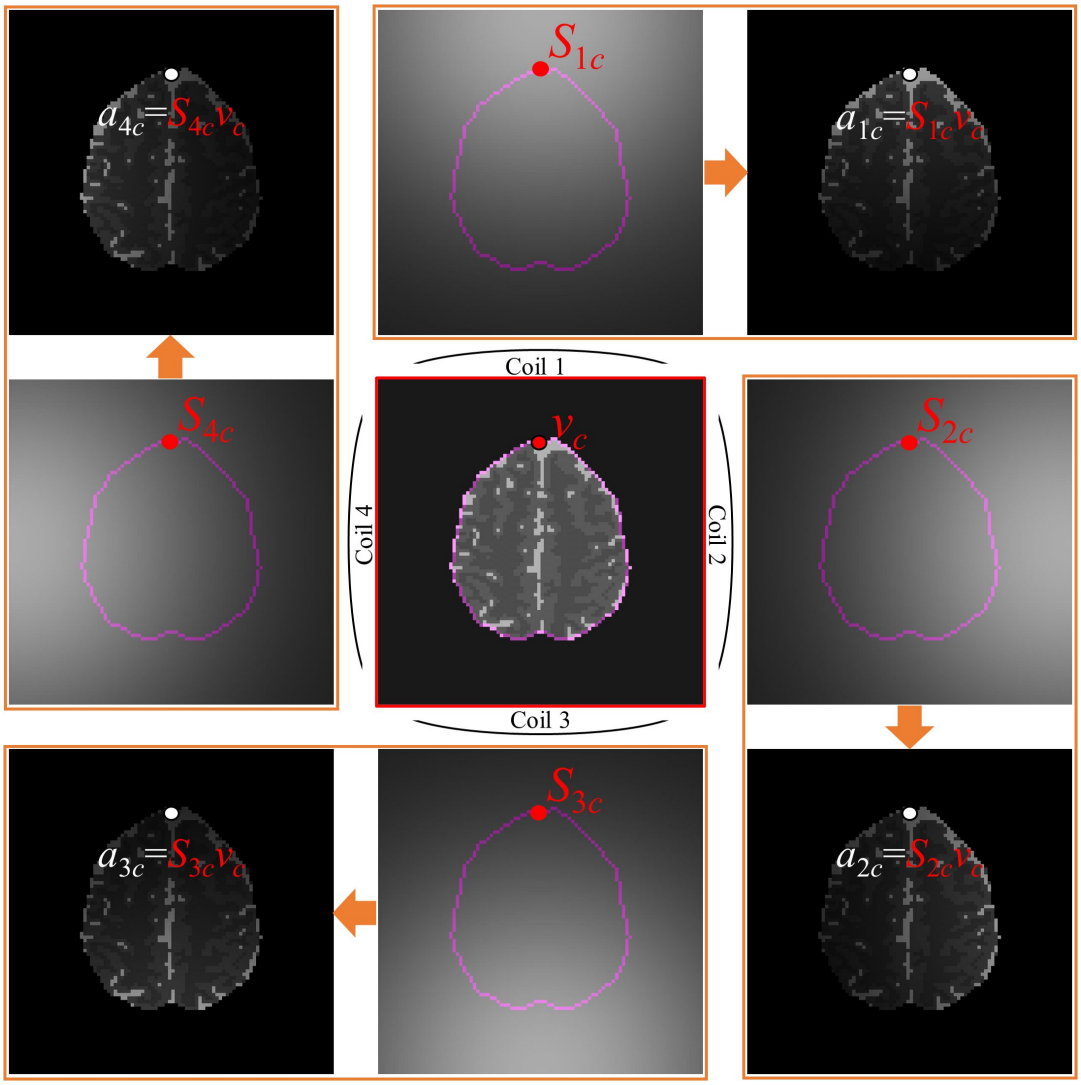

Figure 2.4: True slice image (center) along with the coil sensitivity profiles (top, bottom, left, right) and sensitivity weighted true images (the four corners). The coil sensitivity profiles are typically masked outside the brain but left here to show how the sensitivity decreases with voxels that are further from the coil.

need to be combined into a single, composite brain image. Since voxels are spatially discrete, this process is repeated for the rest of the voxels in the coil measurements.

2.1.3 Multi-Coil with an Acceleration Factor

Increasing the number of receiver coils to be greater than 1 decrease the SNR of the final reconstructed image but allows for subsampling of the k-space arrays. As previously noted,

the primary goal of parallel MR imaging is to increase the number of images acquired per unit of time which can be attained by measuring less data. This can be accomplished by skipping lines in the k-space array, i.e. subsampling, as displayed in Figure 2.5 (left). Skipping lines in k-space introduces what is called an acceleration factor, n_A. The acceleration factor indicates the fraction of lines of data in k-space that are measured and how much sampling time is reduced for a volume image. For example, with an acceleration factor of $n_A = 2$, every other line horizontally in k-space is measured as exhibited on the left side of Figure 2.5. This would result in each slice of the volume k-space arrays to be 48×96 (top right of Figure 2.5) instead of the full 96×96. If it took one second to obtain a full k-space, with $n_A = 2$, the subsampled volume image would take half a second, doubling the rate at which we can observe brain dynamics. If an acceleration factor of $n_A = 3$ is used, a third of the points along the horizontal lines of k-space are measured yielding each slice of the volume image to be 32×96 which means three subsampled volume images would be observed in the time it would take to observe one fully sampled volume image.

However, skipping lines in k-space causes reconstructed coil-weighted brain images to appear folded over itself, or aliased, because the IFT cannot uniquely map the downsampled signals. We can see an example of this in Figure 2.5 (bottom right) where the IFT of the subsampled k-space (top right), with $n_A = 2$, causes the image to be aliased (bottom right). The depiction in Figure 2.5 only shows the aliasing for one of the coils, and since multiple coils are utilized in parallel imaging, a weighted aliased image transpires for each coil. It only shows the magnitude images as associated phase images are not illustratively shown.

Figure 2.6 shows a similar depiction of the full coil-weighted magnitude brain images to Figure 2.4 but introduces an acceleration factor of $n_A = 3$. The sequential subsampling pattern follows one similar to that shown in Figure 2.5 (left) but measuring every third line of k-space instead of every other line, resulting in aliased coil-weighted brain images.

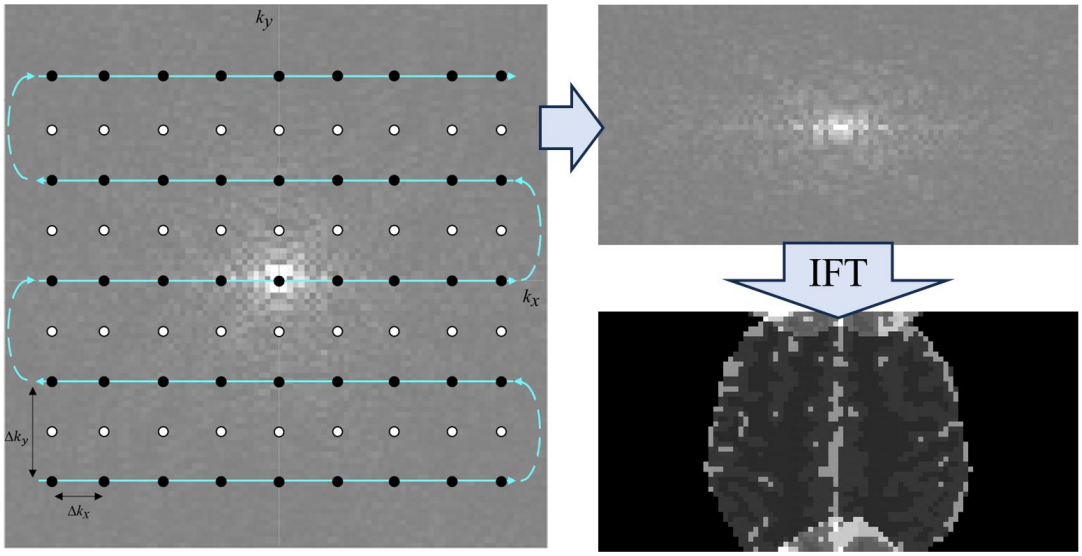

Figure 2.5: Subsampled k-space zig-zag coverage with $n_A = 2$ acceleration factor (left), the finalized subsampled k-space array after omitting the turnaround points (top right) and the aliased brain image after reconstruction using IFT (bottom right).

In Figure 2.6, the aliased image (top right) is the point-wise multiplication of the given voxels (center) by the sensitivity profile for coil 1 (top middle) summed for the three strips, $a_{1c} = S_{11c}v_{1c} + S_{12c}v_{2c} + S_{13c}v_{3c}$. This process is repeated for a_{2c} in coil 2 (bottom right), a_{3c} in coil 3 (bottom left), and a_{4c} in coil 4 (top left). This depiction of four acquired, complex-valued voxel values in the aliased images, $a_c \in \mathbb{C}^{n_C \times 1}$, along with the unacquired, complex-valued coil sensitivities, $S_c \in \mathbb{C}^{n_C \times n_A}$, the unacquired complex-valued unaliased voxel values, $v_c \in \mathbb{C}^{n_A \times 1}$, and the complex-valued measurement error, $\varepsilon_c \in \mathbb{C}^{n_C \times 1}$, create a linear system of complex-valued equations, shown in Eq. 2.2.

$$\begin{bmatrix} a_{1c} \\ a_{2c} \\ a_{3c} \\ a_{4c} \end{bmatrix} = \begin{bmatrix} S_{11c} & S_{12c} & S_{13c} \\ S_{21c} & S_{22c} & S_{23c} \\ S_{31c} & S_{32c} & S_{33c} \\ S_{41c} & S_{42c} & S_{43c} \end{bmatrix} \begin{bmatrix} v_{1c} \\ v_{2c} \\ v_{3c} \end{bmatrix} + \begin{bmatrix} \varepsilon_{1c} \\ \varepsilon_{2c} \\ \varepsilon_{3c} \\ \varepsilon_{4c} \end{bmatrix}. \tag{2.2}$$

Since the unaliased voxel values, v_c, are the parameter of interest, SENSE estimates the

coil sensitivities, S_c, treats it as a known parameter, and models the process as a complex-valued regression model.

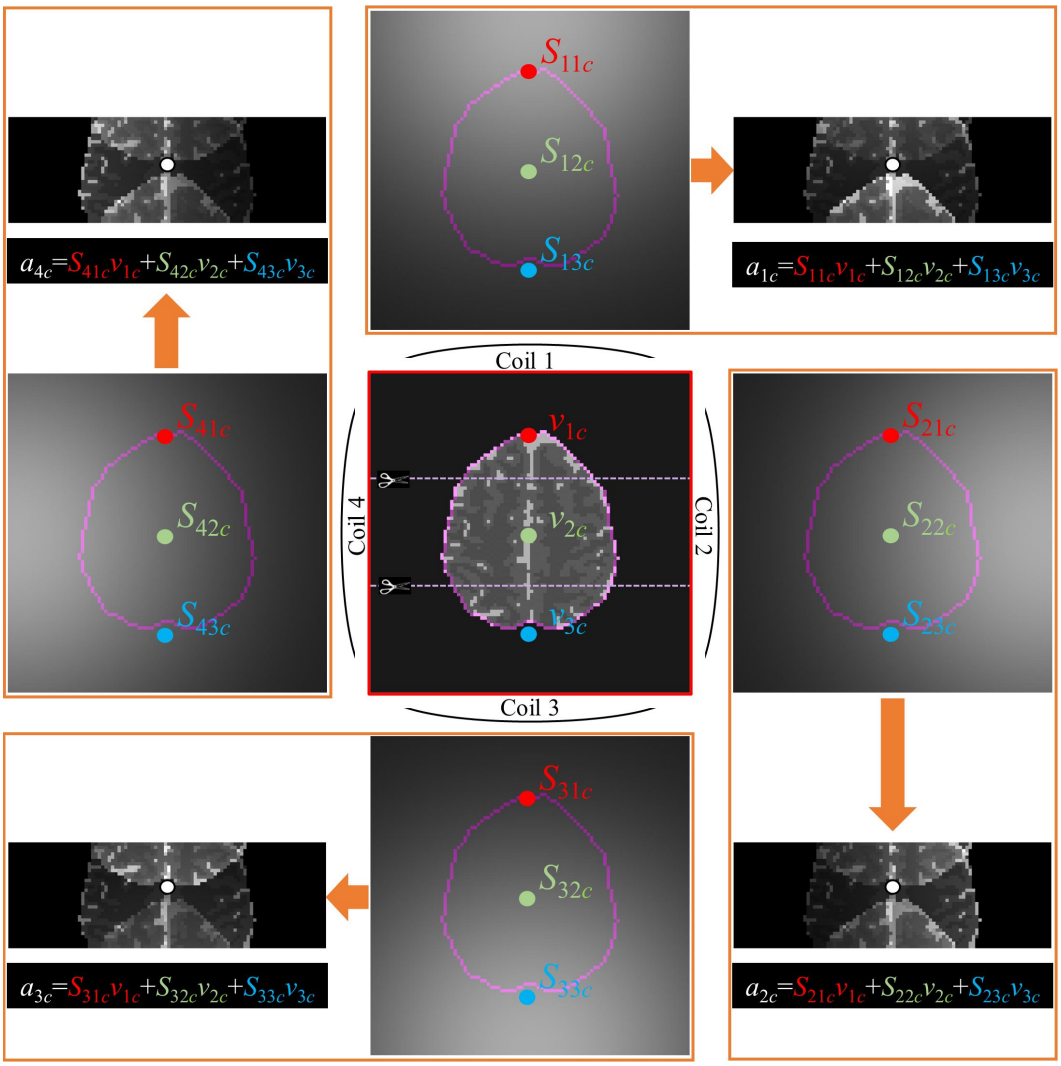

Figure 2.6: True slice image (center) along with the coil sensitivity profiles (top, bottom, left, right) and sensitivity weighted true aliased images (the four corners). The coil sensitivity profiles are typically masked outside the brain but left here to show how the sensitivity decreases with voxels that are further from the coil.

2.1.4 Model

Traditional SENSE performs image reconstruction via the relationship

$$a_c{}^{(\nu)} = S_c{}^{(\nu)} v_c{}^{(\nu)} + \varepsilon_c{}^{(\nu)}, \qquad \nu = 1, ..., K \tag{2.3}$$

where $a_c \in \mathbb{C}^{n_C \times 1}$ is the acquired complex-valued aliased coil measurements, $S_c \in \mathbb{C}^{n_C \times n_A}$ is the matrix of unacquired complex-valued coil sensitivities, $v_c \in \mathbb{C}^{n_A \times 1}$ is the unacquired complex-valued unaliased voxel values, $\varepsilon_c \in \mathbb{C}^{n_C \times 1}$ is the additive complex-valued noise where $\varepsilon_c \sim N(0, \sigma^2(1+i))$, and K is the total number of voxels in the full image divided by the acceleration factor n_A yielding the total number of voxels in the aliased image. Prior to an fMRI experiment, a short non-task based set of n_{cal} full k-space volume arrays for the n_C coils can easily be obtained. These commonly measured full k-space volume arrays are inverse Fourier transformed into full pre-scan coil calibration images similar to Figure 2.4. From these pre-scan calibration images, an estimate of the complex-valued coil sensitivities $\hat{S}_c$ can be obtained. The SENSE least squares estimator of v_c from Eq. 2.4 is given by

$$\hat{v}_c^{(\nu)} = (\hat{S}_c^{(\nu)^\dagger} \hat{S}_c^{(\nu)})^{-1} \hat{S}_c^{(\nu)^\dagger} a_c^{(\nu)}, \qquad \nu = 1, ..., K. \tag{2.4}$$

where † is the Hermitian or conjugate transpose. The SENSE process is repeated for each voxel in the aliased image to estimate the unaliased voxel values v_c yielding a single full FOV brain image. The design matrix S_c is generally ill-conditioned which causes SNR, a ratio that measures that signal intensities in imaging to background noise, to degrade. This can also cause aliasing artifacts in the final reconstructed image under SENSE (Pruessmann et al., 1999).

In SENSE image reconstruction, the use of a regularizer such as ridge or lasso regression, can be used to address issues with aliasing artifacts or SNR degradation. However, the regularization has been shown to introduce bias, resulting in blurred images (King and Angelos, 2001; Liang et al., 2001; Lin et al., 2004). These deficiencies motivate our Bayesian approach, which allows for a more general and automated method for image reconstruction. With the use of all available prior information, our Bayesian approach provides full distributions for the unaliased voxel values, coil sensitivities, and residual image variance.

2.2 SENSE vs. SENSE-ITIVE

We now consider the true complex-valued version of the scenarios described in the previous subsection, as k-space data acquired by the MRI scanner is not real-valued. Traditional SENSE performs reconstruction while the data values are still in complex-valued form shown in Eq 2.5.

$$(a_R + ia_I) = (S_R + iS_I)(v_R + iv_I) + (\varepsilon_R + i\varepsilon_I). \tag{2.5}$$

Bruce et al. (2012) shows that the complex-valued model in Eq. 2.5 can be expressed by a real-valued isomorphic representation called the SENSE-ITIVE model conveyed by Eq. 2.6.

$$\begin{bmatrix} a_R \\ \hdashline a_I \end{bmatrix} = \left[\begin{array}{c:c} S_R & -S_I \\ \hdashline S_I & S_R \end{array}\right] \begin{bmatrix} v_R \\ \hdashline v_I \end{bmatrix} + \begin{bmatrix} \varepsilon_R \\ \hdashline \varepsilon_I \end{bmatrix}, \qquad (\varepsilon_R, \varepsilon_I)' \sim N(0, \sigma^2 I_{2n_C}). \tag{2.6}$$

Eq. 2.6 characterizes the design matrix S as being skew-symmetric. The proposed BSENSE model will use the real-valued isomorphism instead of the complex-valued representation (Bruce et al., 2012). Continuing the illustrative use of $n_C = 4$ receiver coils displayed in Figures 2.3, 2.4, and 2.6, the depth sensitivity profiles for each coil now contain a real part and an imaginary part. Each coil measures a complex-valued sensitivity weighted true image slice that is dependent on the location and size of the coil plus complex-valued noise. Figure 2.7, similar to Figure 2.6, shows the true noiseless complex-valued image slices with $n_C = 4$ coils (top, bottom, left, right) and their respective depth sensitivity to the aliased true image slice (the four corners of the figure) with the real parts on the left and the imaginary parts on the right. In Figure 2.7 (top right) the aliased image is the pointwise multiplication of the given voxel by the sensitivity profile for coil 1 summed for the three strips. The linear equations for the real component and the imaginary component are

expressed in Figure 2.7 (top right). This process is repeated for coil 2 (bottom right), coil 3 (bottom left), and coil 4 (top left), displayed in Figure 2.7, with the respective real and imaginary equations.

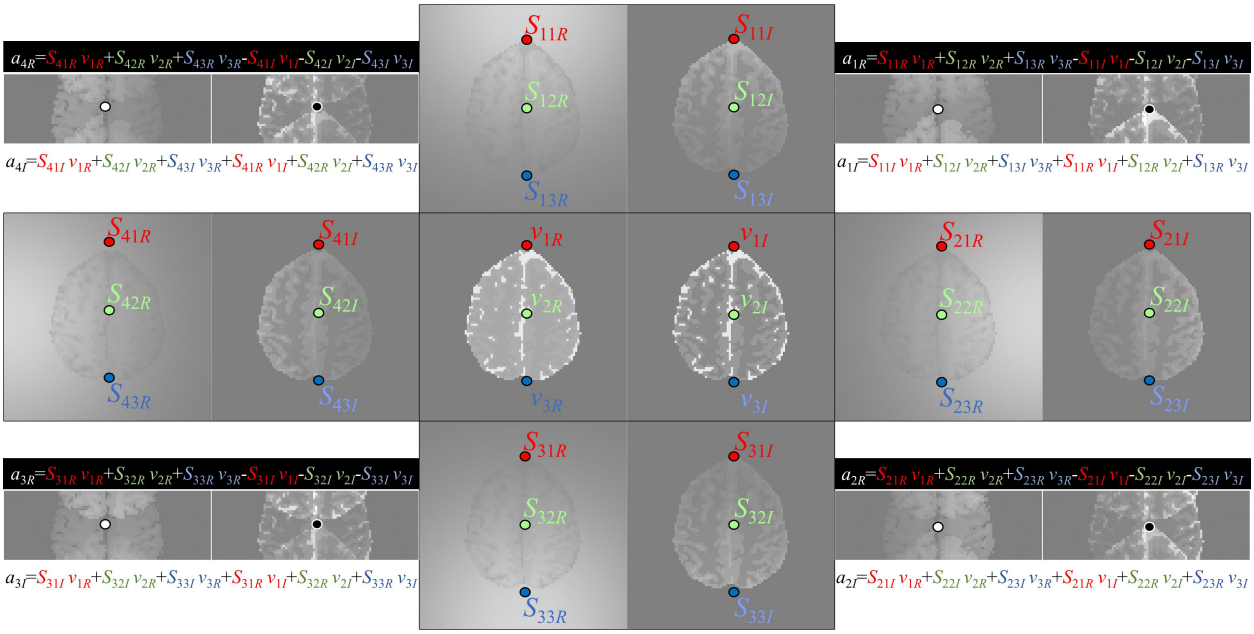

Figure 2.7: True real and imaginary slice image (center) along with real and imaginary coil sensitivity profiles (top, bottom, left, right) and sensitivity weighted real and imaginary true aliased images (the four corners).

The $n_C = 4$ coil measurements create a system of equations which can be expressed in matrix form as shown in Eq. 2.7, where the a's are acquired aliased coil measurements, the S's are unacquired coil sensitivities, and the v's are unacquired true slice voxel values. Likewise in Eq. 2.6 this representation creates a skew symmetric design matrix for S. This equation is a latent variable model but complex-valued and can be more compactly written as $a = Sv + \varepsilon$ where $a \in \mathbb{R}^{2n_C \times 1}$, $S \in \mathbb{R}^{2n_C \times 2n_A}$, $v \in \mathbb{R}^{2n_A \times 1}$ and $\varepsilon \in \mathbb{R}^{2n_C \times 1}$ are the real-valued isomorphic representations of a_c, S_c, v_c, and ε_c respectively. Our proposed model uses

this real-valued representation.

$$\left[\begin{array}{c} a_{1R} \\ a_{2R} \\ a_{3R} \\ a_{4R} \\ \hdashline a_{1I} \\ a_{2I} \\ a_{3I} \\ a_{4I} \end{array}\right] = \left[\begin{array}{ccc:ccc} S_{11R} & S_{12R} & S_{13R} & -S_{11I} & -S_{12I} & -S_{13I} \\ S_{21R} & S_{22R} & S_{23R} & -S_{21I} & -S_{22I} & -S_{23I} \\ S_{31R} & S_{32R} & S_{33R} & -S_{31I} & -S_{32I} & -S_{33I} \\ S_{41R} & S_{42R} & S_{43R} & -S_{41I} & -S_{42I} & -S_{43I} \\ \hdashline S_{11I} & S_{12I} & S_{13I} & S_{11R} & S_{12R} & S_{13R} \\ S_{21I} & S_{22I} & S_{23I} & S_{21R} & S_{22R} & S_{23R} \\ S_{31I} & S_{32I} & S_{33I} & S_{31R} & S_{32R} & S_{33R} \\ S_{41I} & S_{42I} & S_{43I} & S_{41R} & S_{42R} & S_{43R} \end{array}\right] \left[\begin{array}{c} v_{1R} \\ v_{2R} \\ v_{3R} \\ \hdashline v_{1I} \\ v_{2I} \\ v_{3I} \end{array}\right] + \left[\begin{array}{c} \varepsilon_{1R} \\ \varepsilon_{2R} \\ \varepsilon_{3R} \\ \varepsilon_{4R} \\ \hdashline \varepsilon_{1I} \\ \varepsilon_{2I} \\ \varepsilon_{3I} \\ \varepsilon_{4I} \end{array}\right]. \tag{2.7}$$

2.3 BSENSE Technique

For the proposed Bayesian approach, we use the same data generating mechanism as SENSE-ITIVE (and SENSE). That is $a = Sv + \varepsilon$ where $\varepsilon \in \mathbb{R}^{2n_C \times 1}$ is the real-valued representation of the measurement error with the real part ε_R stacked on top of the imaginary part ε_I. In this work, two different representations of the coil sensitivities will be used. The first representation is $S \in \mathbb{R}^{2n_C \times 2n_A}$ as demonstrated in Eq. 2.7 is necessary for the proper skew symmetric design matrix for complex-valued multiplication. The second is $H = [S_R,\ S_I]$, used in the prior distribution and ultimately for parameter estimation of the coil sensitivities, since S_R and S_I uniquely determine S and do not need to be duplicated.

2.3.1 Data Likelihood, Prior and Posterior Distributions

Similar to SENSE, we assume that the residual error is normal and independent and identically distributed in the real and imaginary components. The likelihood for the aliased

voxel measurements for the n_C coils becomes

$$P(a|S,v,\sigma^2)\propto(\sigma^2)^{-\frac{2n_C}{2}}\exp\Big[-\frac{1}{2\sigma^2}(a-Sv)'(a-Sv)\Big]. \tag{2.8}$$

We can quantify available prior information about the unobserved parameters of the voxel intensities v, the coil sensitivities S, and the residual variance σ^2 in the likelihood with assessed hyperparameters of prior distributions. The voxel values v are specified to have a normal prior distribution, expressed in Eq. 2.9, since the real and imaginary components of fMRI data are assumed to be normally distributed (Henkelman, 1985; Lindquist, 2008). The coil sensitivities, represented as H, are also specified to have a normal prior distribution (Eq. 2.10) and the noise variance σ^2 is specified to have an inverse gamma distribution (Eq. 2.11).

$$P(v|n_v,v_0,\sigma^2)\propto(\sigma^2)^{-\frac{2n_A}{2}}\exp\Big[-\frac{n_v}{2\sigma^2}(v-v_0)'(v-v_0)\Big], \tag{2.9}$$

$$P(H|n_S,H_0,\sigma^2)\propto(\sigma^2)^{-\frac{2n_Cn_A}{2}}\exp\Big[-\frac{n_S}{2\sigma^2}tr(H-H_0)'(H-H_0)\Big], \tag{2.10}$$

$$P(\sigma^2|\alpha,\beta)\propto(\sigma^2)^{-(\alpha+1)}\exp\left[-\frac{\beta}{\sigma^2}\right], \tag{2.11}$$

where tr is the trace of the $(H-H_0)'(H-H_0)$ matrix. The hyperparameters n_S, H_0, n_v, v_0, α, and β are automatically assessed from the pre-scan calibration images, but can also be determined using a fully subjective approach. The joint posterior distribution of the true slice voxel values v, the coil sensitivities S (as H), and the noise variance σ^2 is

$$P(v,H,\sigma^2|a)\propto P(a|S,v,\sigma^2)P(v|n_v,v_0,\sigma^2)P(H|n_S,H_0,\sigma^2)P(\sigma^2|\alpha,\beta), \tag{2.12}$$

with the distributions specified from Equations 2.8, 2.9, 2.10, and 2.11.

2.3.2 Hyperparameter Determination

The full pre-scan coil calibration images can be utilized to fully assess appropriate hyperparameters for the prior distributions in an automated way. For example, the n_{cal} coil calibration images (top left of Figure 2.8) can be averaged together to give us full complex-valued coil images. A magnitude v_{0M} of the prior mean can be estimated for each voxel in the unaliased image by computing the Euclidean norm shown in the top right of Figure 2.8.

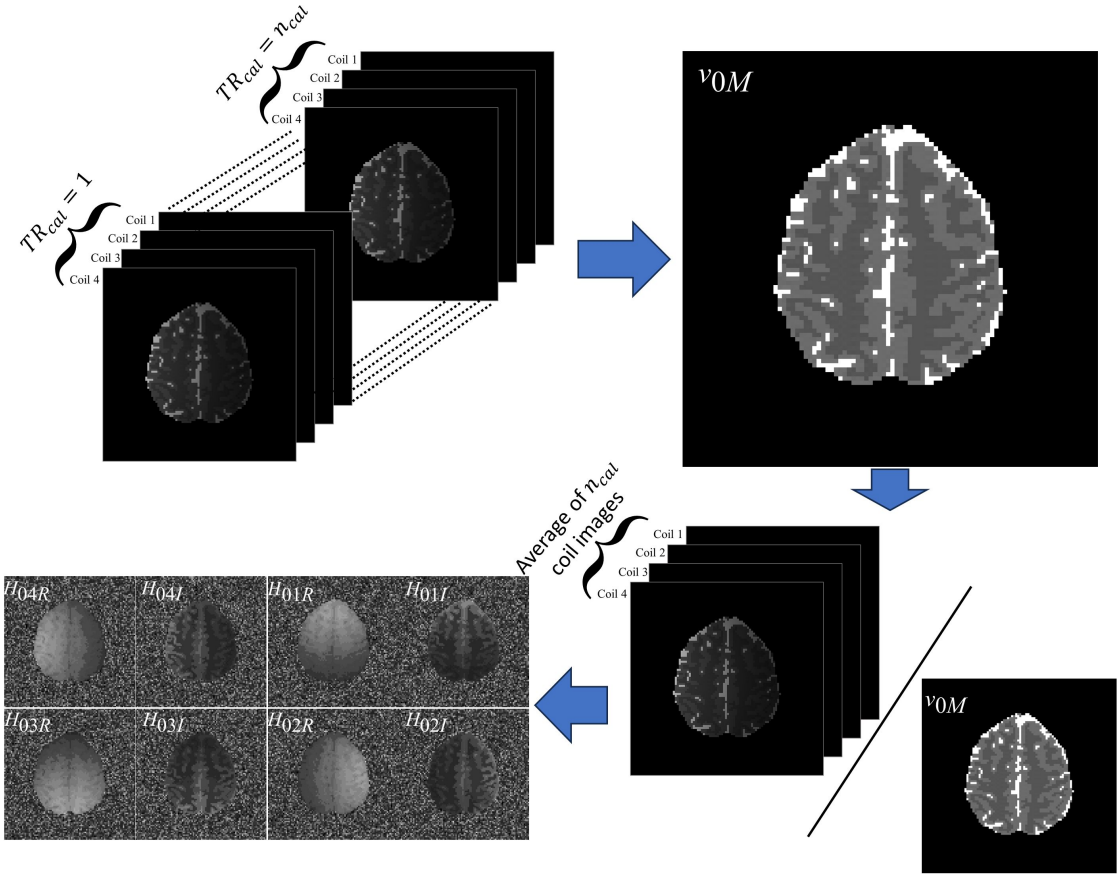

Figure 2.8: The n_{cal} calibration coil images (top left) are averaged through time and the Euclidean norm is taken yielding a prior mean for the magnitude unaliased voxel values v_{0M} (top right). The average of the coil calibration images is then point-wise divided by v_{0M} resulting in prior means for the real and imaginary parts of the coil sensitivities H_{0R} and H_{0I}, respectively.

The n_c averaged coil calibration images can then be point-wise divided by v_{0M} to obtain a prior mean for the real and imaginary coil sensitivities, as displayed in the bottom of Figure

2.8. The phase of the coil sensitivities is assessed by $arctan(I/R)/2$ where R and I are the real and imaginary components of the coil sensitivities, respectively. This phase is utilized to assess complex-valued prior means for the coil sensitivities, H_0. These coil sensitivity hyperparameters, H_0, along with the full averaged calibration coil images are used to assess complex-valued prior means for the voxel values, v_0.

The hyperparameters n_S and n_v, which are the scalar weights of the prior means, are assessed to be the number of calibration images n_{cal}. The average residual variance over the voxels of the calibration images is calculated to obtain a prior for the noise variance σ_0^2. The hyperparameters α (shape parameter of the inverse gamma) and β (scale parameter of the inverse gamma) are assessed to be $\alpha = n_{cal} - 1$ and $\beta = (n_{cal} - 1)\sigma_0^2$. This prior information is incorporated to reconstruct each voxel measurement in the aliased coil image into the unaliased voxel values at every time point in the fMRI series.

2.3.3 Parameter Estimation

Using the posterior distribution in Eq. 2.12, two approaches are used to estimate the unaliased voxel values v, coil sensitivities S, and residual variance σ^2: Maximum *a posteriori* (MAP) estimation using the Iterated Conditional Modes (ICM) optimization algorithm (Lindley and Smith, 1972; O'Hagan, 1994) to find the joint posterior mode, and marginal posterior mean (MPM) estimation via Markov chain Monte Carlo (MCMC) Gibbs sampling (Geman and Geman, 1984; Gelfand and Smith, 1990). Beginning with the initial estimates of the each parameter, ICM iterates over the parameters, calculating its posterior conditional mode and converges to a maximum of the joint posterior density. Since each of the posterior conditionals are unimodal, the ICM will produce the global maximum, the MAP. The conditional modes are

$$\hat{v} = (S'S + n_v I_{2n_A})^{-1}(S'a + n_v v_0), \tag{2.13}$$

$$\hat{H} = (V'V + n_S I_{2n_A})^{-1}(VY' + n_S H_0), \tag{2.14}$$

$$\hat{\sigma}^2 = \frac{\Theta}{2(2n_C + 2n_A + \alpha + 2n_C n_A + 1)}, \tag{2.15}$$

where $\Theta = (a - Sv)'(a - Sv) + n_v(v - v_0)'(v - v_0) + \alpha\beta + n_S tr[(H - H_0)(H - H_0)']$, $Y = [a_R, a_I]$ and $V \in \mathbb{R}^{2n_A \times 2}$ is a skew symmetric matrix representation of the unaliased voxel values v as expressed by

$$V = \begin{bmatrix} v_R & v_I \\ -v_I & v_R \end{bmatrix}. \tag{2.16}$$

The full conditional distributions are given by

$$v|S, \sigma^2, a \sim N\{\hat{v}, \sigma^2(S'S + n_v I_{2n_A})^{-1}\}, \tag{2.17}$$

$$H|v, \sigma^2, a \sim MN\{\hat{H}, \sigma^2(V'V + n_S I_{2n_A})^{-1}\}, \tag{2.18}$$

$$\sigma^2|v, S, a \sim IG\{\alpha_*, \beta_*\}, \tag{2.19}$$

where $\alpha_* = n_C n_A + n_C + n_A + \alpha$ and $\beta_* = [(a - Sv)'(a - Sv) + n_v(v - v_0)'(v - v_0) + n_S tr((H - H_0)(H - H_0)') + 2\beta]/2$. What distinguishes the MAP estimate from a penalized MLE is more available prior information is incorporated in the reconstruction of the aliased coil images. This process is also completely objective providing a fully automated method without having to calculate a subjective penalty. Our Bayesian approach, however, is flexible enough to include subjective priors if desired. Because we are using available prior information from the calibration images, we expect the subsequent estimators to have smaller variance and higher SNR. To illustrate this, extensive realistic simulations are performed in Chapter 5 of this dissertation.

CHAPTER 3: Bayesian GRAPPA (BGRAPPA)

3.1 GRAPPA Technique

3.1.1 Reconstruction Process

Like SENSE, GRAPPA is a parallel image reconstruction technique that produces full images from subsampled k-space data. However, SENSE image reconstruction operates in

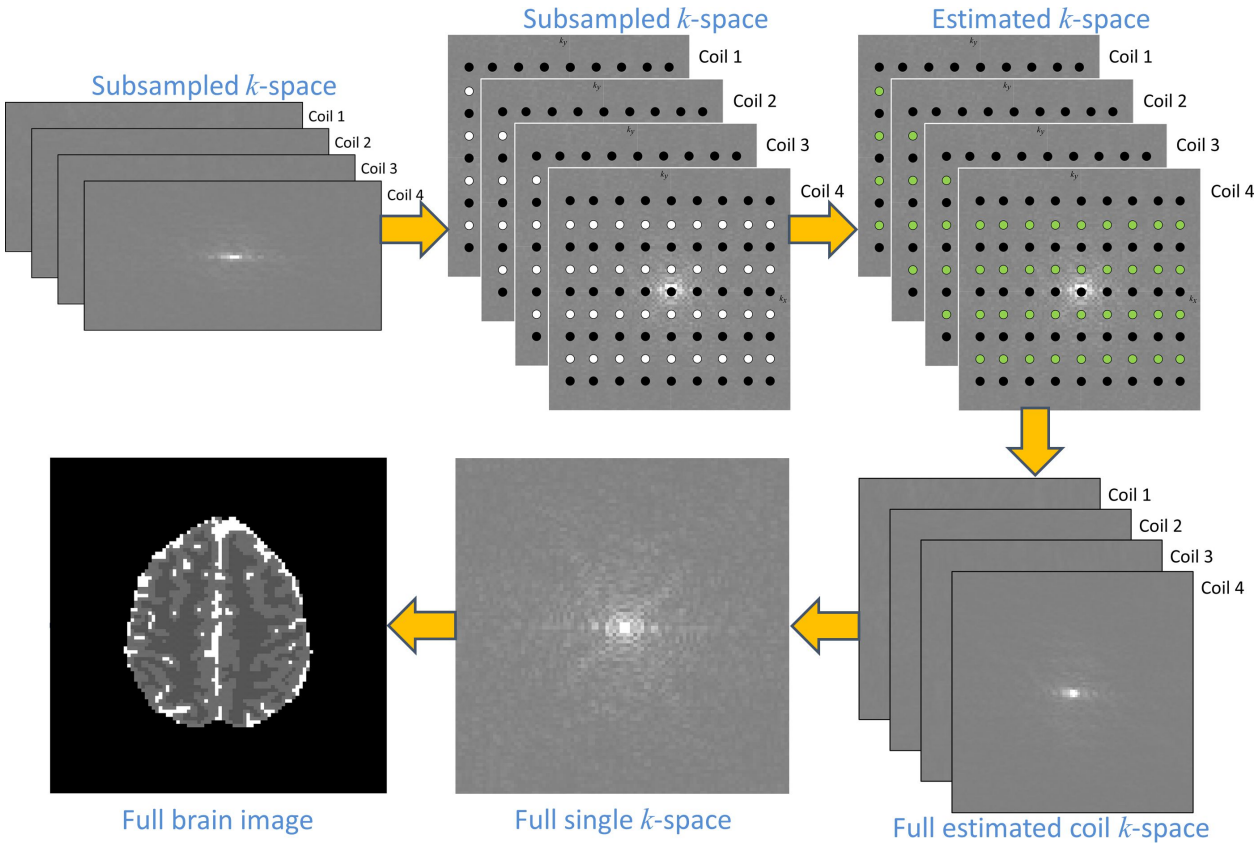

Figure 3.1: Subsampled k-space coil arrays (top left) that are spread out to show a full k-space array where the black dots are the acquired spatial frequencies, and the white dots are the unacquired spatial frequencies (top middle). The missing spatial frequencies are then estimated (green dots in the top right) yielding full coil k-space arrays (bottom right). The full coil k-space arrays are averaged together to produce a full spatial frequency array (bottom middle) which is then transformed into a full brain image (bottom left) using the IFT.

the image domain while GRAPPA operates in the spatial frequency domain. The process for GRAPPA is exhibited in Figure 3.1 with an illustrative example of using $n_C = 4$ coils. The machine acquires subsampled spatial frequency arrays for each of the four coils shown in the top left of Figure 3.1. The top middle of Figure 3.1 displays the subsampled k-space arrays as full arrays with the black dots indicating the acquired spatial frequencies and the white dots indicating the unacquired spatial frequencies. The unacquired spatial frequencies are estimated using GRAPPA image reconstruction, displayed as green dots in the top right of Figure 3.1. This yields full coil k-space arrays as shown in the bottom right of Figure 3.1. To get a single full spatial frequency array (bottom middle), the full coil spatial frequency arrays are averaged together. The full spatial frequency is then IFT reconstructed into a single, full FOV brain image (bottom left of Figure 3.1).

3.1.2 Model

For GRAPPA reconstruction, localized weights are assessed to interpolate the unacquired spatial frequencies. There are two different methods of assessing the weights used for interpolation. The first method is from acquiring extra lines within the center portion of k-space, known as auto-calibration signal (ACS) measurements, when subsampling the k-space arrays. An autocalibration pulse sequence is more difficult and there is no information for higher k_y spatial frequencies (further from the center of the array). The second, preferred, method is acquiring full FOV calibration k-space arrays pre-scan like the calibration images obtained for SENSE without using the IFT to transform the spatial frequency arrays into the image domain. For this research, we will continue with using pre-scan full FOV calibration information for prior information. This allows you to reconstruct with SENSE, GRAPPA, or both.

To calculate the localized weights used for interpolation, a kernel with k_{row} rows and

k_{col} columns is placed around the acquired spatial frequency points closest to the calibration point. There are four kernel sizes that will be used for this research: 2×1, 4×1, 2×3, and 4×5. A visual of these kernel sizes are displayed in Figure 3.2 with an illustrative use of $n_A = 2$ acceleration factor. Using a larger kernel allows for more data points to be averaged together which can result in an increase in the accuracy of the interpolated value. However, this can cause higher correlations with more local voxels than a smaller kernel would encounter and can be more computationally expensive. These thoughts are taken into consideration when determining which kernel size to use.

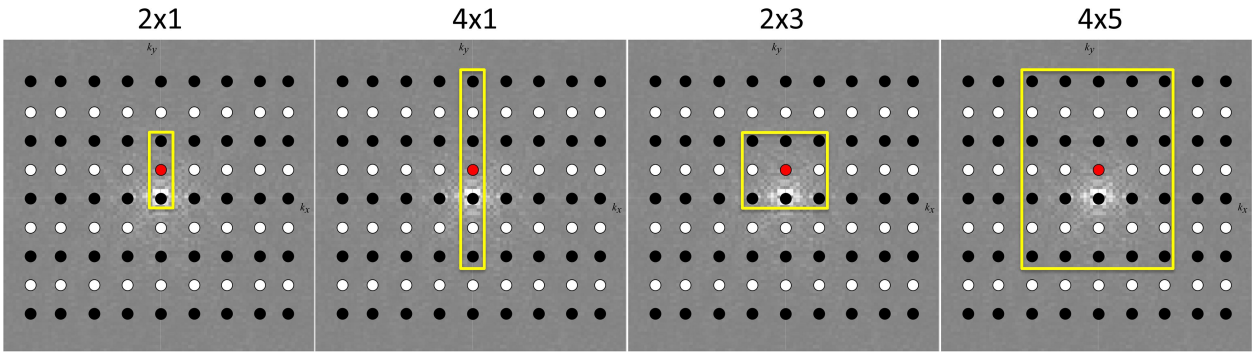

Figure 3.2: Different kernel sizes used for estimating localized weights: 2×1, 4×1, 2×3, and 4×5.

Figure 3.3 illustrates how a 2×1 kernel is utilized to estimate the weights from the full coil calibration spatial frequencies with a four-channel coil array. In Figure 3.3, all the complex-valued data points are acquired, but are treated differently depending on the location of the data point. The black data points, f_l, are utilized as the "acquired" complex-valued spatial frequency values, the red points, f_{calib}, are the complex-valued calibration spatial frequency points, and the white points are ignored for the calculation of those weights associated with the current f_{calib} points. The white dots represent the spatial frequencies that would be unacquired during the fMRI experiment but are used as calibration points to estimate the complex-valued weights for those spatial frequencies.

The calibration points f_{calib} and the "acquired" spatial frequencies f_l along with the

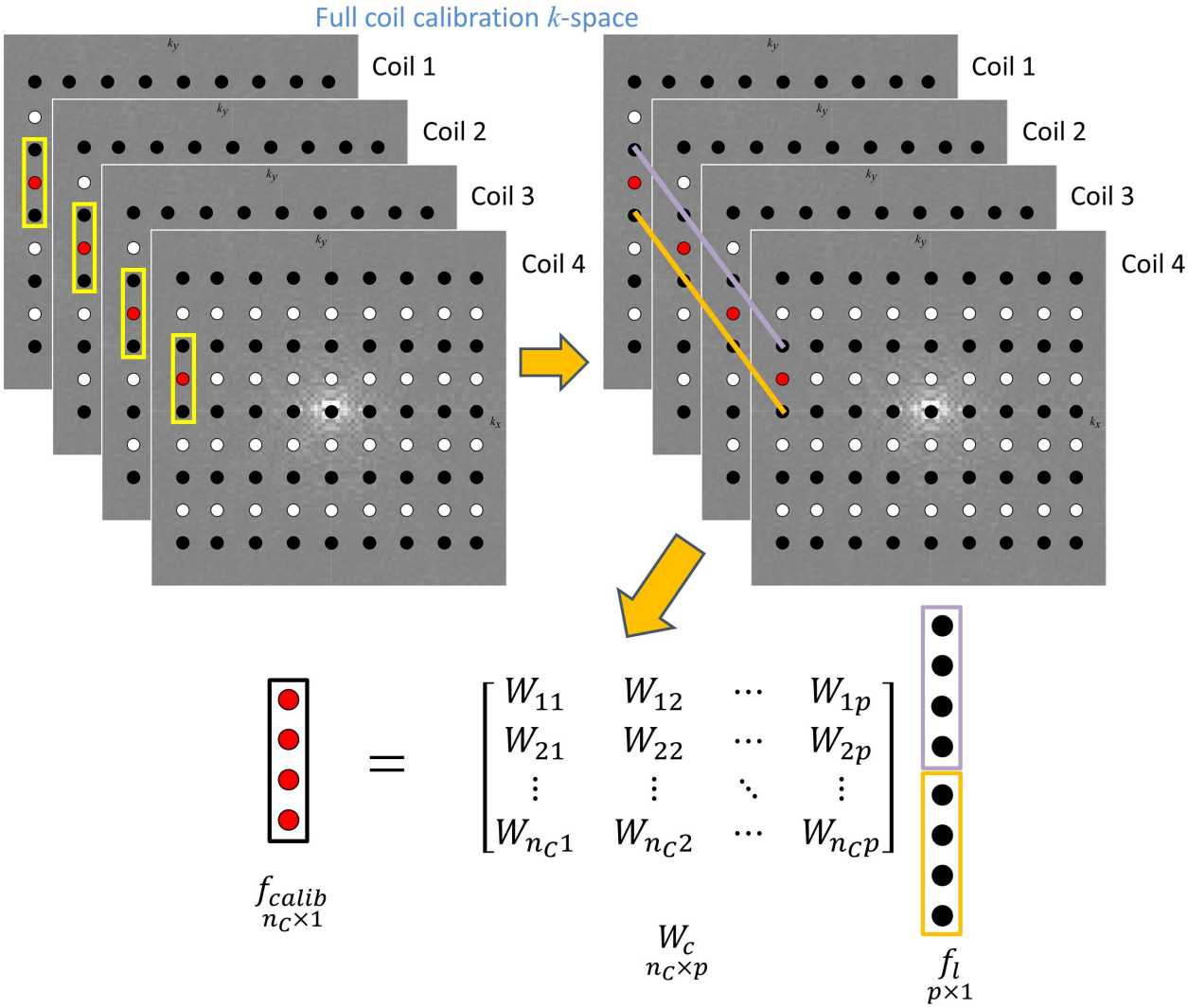

Figure 3.3: The k-space coil arrays in the top left are fully sampled where the black dots are treated as the acquired spatial frequencies and the red dots are the calibration point utilized to calculate the weights for those coil spatial frequencies. The yellow box shows a 2×1 kernel indicating which points are utilized to estimate the weights. From this, we get an acquired black dot above and below each red coil calibration point. The black points above the calibration points are then stacked by coil (1 through 4) which is then placed above the stacked black dots below the calibration points. The image in the top right demonstrates the stacking of the black dots through the purple line and the orange line with the purple vector then being placed above the orange vector in the system of linear equations (bottom). The weights, W_c, for those "unacquired spatial frequencies are then estimated using least squares. Once the weights have been estimated, the red calibration points move to the next white dots to estimate the set of weights for the next unacquired spatial frequencies.

complex-valued weights, W_c, create a system of linear equations as displayed in Figure 3.3

(bottom). From the linear equations, we can estimate the weights W_c using Eq. 3.1.

$$W_c{}^{(\omega)} = f_{calib}{}^{(\omega)} f_l{}^{(\omega)\dagger} (f_l{}^{(\omega)} f_l{}^{(\omega)\dagger})^{-1}, \quad \omega = 1, ..., L, \tag{3.1}$$

where $W_c \in \mathbb{C}^{n_C \times p}$ is the complex-valued weights, $f_{calib} \in \mathbb{C}^{n_C \times 1}$ is the complex-valued calibration spatial frequencies, $f_l \in \mathbb{C}^{p \times 1}$ is the "acquired" complex-valued spatial frequencies, $p = n_c k_{rows} k_{cols}$, $\dagger$ is the Hermitian or conjugate transpose, and L is the total number of unacquired spatial frequencies in the subsampled k-space array. The process is repeated for each spatial frequency point that would be unacquired during the actual fMRI experiment (the white dots in Figure 3.3), yielding different weights for each unacquired spatial frequency.

Once the weights for each of the unacquired coil spatial frequencies are estimated from the calibration k-space arrays, those weights are then utilized to interpolate the unacquired spatial frequencies in the actual fMRI experiment. The GRAPPA model with the estimated weights becomes

$$f_{ec}{}^{(\omega)} = W_c{}^{(\omega)} f_{kc}{}^{(\omega)} + \eta_c{}^{(\omega)}, \qquad \omega = 1, ..., L, \tag{3.2}$$

where $f_{ec} \in \mathbb{C}^{n_C \times 1}$ is the complex-valued interpolated k-space values, $f_{kc} \in \mathbb{C}^{p \times 1}$ is the complex-valued acquired k-space values, and $\eta_c \in \mathbb{C}^{n_C \times 1}$ is the additive complex-valued noise with $\eta_c \sim N(0, \tau^2(1+i))$. The interpolated coil k-space values, f_{ec}, are inserted in the respective locations of each coil yielding full coil k-space arrays, f_{full}, (top right of Figure 3.1). The full coil spatial frequency arrays f_{full} are averaged together and the IFT is applied to the single, full FOV k-space array reconstructing to a full FOV brain image.

With GRAPPA image reconstruction, however, the resulting reconstructed brain images can have diminished SNR which is a consequence of either a decreased signal intensity, increased temporal noise variance, or a combination of the two. With an increase in the deficiencies motivate our Bayesian approach, which will allow for a more automated method

for image reconstruction without having to potentially store and use large matrices. Unlike GRAPPA, our Bayesian approach will utilize all valuable available prior information from the calibration spatial frequency arrays and provide full distributions for the unacquired spatial frequencies, the weights, and the residual k-space variance.

3.2 GRAPPA Isomorphic Representation

Similar to the SENSE-ITIVE model of SENSE, we can write a as real-valued isomorphic representation model of the complex-valued GRAPPA model. The traditional GRAPPA model estimates the unacquired spatial frequencies while the data values are still in complex-valued form shown in Eq 3.3.

$$(f_{eR} + if_{eI}) = (W_R + iW_I)(f_{kR} + if_{kI}) + (\eta_R + i\eta_I). \tag{3.3}$$

This complex-valued model can be expressed by a real-valued isomorphic representation as conveyed by Eq. 3.4.

$$\left[\begin{array}{c} f_{eR} \\ \hdashline f_{eI} \end{array}\right] = \left[\begin{array}{c:c} W_R & -W_I \\ \hdashline W_I & W_R \end{array}\right] \left[\begin{array}{c} f_{kR} \\ \hdashline f_{kI} \end{array}\right] + \left[\begin{array}{c} \eta_R \\ \hdashline \eta_I \end{array}\right], \qquad (\eta_R, \eta_I)' \sim N(0, \tau^2 I_{2n_C}). \tag{3.4}$$

Eq. 3.4 characterizes the design matrix W as being skew-symmetric. The proposed BGRAPPA model will use the real-valued isomorphism (Eq. 3.4) instead of the complex-valued representation (Eq. 3.2).

3.3 BGRAPPA Technique

For our proposed Bayesian approach, we use the same linear model as GRAPPA as expressed Eq. 3.2, except the acquired spatial frequencies will be the f_{ec} variable instead of

the f_{kc} variable. This creates a model where the design matrix and the coefficients can both be treated as unknown parameters, allowing us to take a Bayesian approach to the linear regression. Then the weights, W_c, and the unacquired spatial frequencies, f_{kc}, along with the residual k-space variance, τ^2, are treated as unknowns with prior distributions placed on them. We also use an isomorphic real-valued representation of the linear GRAPPA model in Eq. 3.4 where $f_{eR} \in \mathbb{R}^{n_C \times 1}$ and $f_{eI} \in \mathbb{R}^{n_C \times 1}$ are the real and imaginary components, respectively, of f_{ec}, $W_R \in \mathbb{R}^{n_C \times p}$ and $W_I \in \mathbb{R}^{n_C \times p}$ are the real and imaginary components of W_c, $f_{kR} \in \mathbb{R}^{p \times 1}$ and $f_{kI} \in \mathbb{R}^{p \times 1}$ are the real and imaginary components of f_{kc}, and $\eta_R \in \mathbb{R}^{n_C \times 1}$ and $\eta_I \in \mathbb{R}^{n_C \times 1}$ are the real and imaginary components of η_c. This equation is a latent variable model with complex values and can be more compactly written as $f_e = W f_k + \eta$ where $f_e \in \mathbb{R}^{2n_C \times 1}$, $W \in \mathbb{R}^{2n_C \times 2p}$, $f_k \in \mathbb{R}^{2p \times 1}$, and $\eta \in \mathbb{R}^{2n_C \times 1}$ are the real-valued isomorphic representations of f_{ec}, W_c, f_{kc}, and η_c, respectively.

In this method, two different representations of the weights will be used. The first representation is the proper skew-symmetric design matrix W as shown in Eq. 3.4. The second representation is $D = [W_R, W_I]$ which is used in the prior distribution and for parameter estimation of the weights. This is to ensure W_R and W_I are uniquely estimated for W and do not need to be duplicated.

3.3.1 Data Likelihood, Prior and Posterior Distributions

Similar to GRAPPA, we assume that the residual spatial frequency error is normally distributed in the real and imaginary components, since the real and imaginary components of fMRI data are assumed to be normally distributed (Henkelman, 1985; Lindquist, 2008). The data likelihood for the acquired spatial frequencies for the n_c coils is

$$P(f_e|W, f_k, \tau^2) \propto (\tau^2)^{-\frac{2n_C}{2}} \exp\left[-\frac{1}{2\tau^2}(f_e - W f_k)'(f_e - W f_k)\right]. \tag{3.5}$$

We can quantify available prior information about the unacquired spatial frequencies f_k, the weights W, and the residual k-space variance τ^2 with assessed hyperparameters of prior distributions. The unacquired spatial frequencies f_k are specified to have a normal prior distribution, expressed in Eq. 3.6. The weights D are also specified to have a normal prior distribution (Eq. 3.7) and the k-space noise variance τ^2 is specified to have an inverse gamma prior distribution (Eq. 3.8),

$$P(f_k|n_k, f_{k0}, \tau^2) \propto (\tau^2)^{\frac{-2p}{2}} \exp\left[-\frac{n_k}{2\tau^2}(f_k - f_{k0})'(f_k - f_{k0})\right], \tag{3.6}$$

$$P(D|n_w, D_0, \sigma^2) \propto (\tau^2)^{\frac{-2n_C p}{2}} \exp\left[-\frac{n_w}{2\tau^2} tr(D - D_0)(D - D_0)'\right], \tag{3.7}$$

$$P(\tau^2|\alpha_k, \delta) \propto (\tau^2)^{-(\alpha_k+1)} \exp\left[-\frac{\delta}{\tau^2}\right], \tag{3.8}$$

where tr is the trace of the $(D-D_0)(D-D_0)'$ matrix and the hyperparameters n_k, f_{k0}, n_w, D_0, α_k, and δ are assessed from the pre-scan calibration spatial frequencies. The joint posterior distribution of the unacquired spatial frequencies f_k, the weights W, and the residual k-space variance τ^2 is

$$P(f_k, D, \tau^2|f_e) \propto P(f_e|W, f_k, \tau^2)P(f_k|n_k, f_{k0}, \tau^2)P(D|n_w, D_0, \tau^2)P(\tau^2|\alpha_k, \delta), \tag{3.9}$$

with the distributions specified from Equations 3.5, 3.6, 3.7, and 3.8.

3.3.2 Hyperparameter Determination

The hyperparameters can be appropriately assessed in an automated way using the full pre-scan coil calibration spatial frequencies. For the BGRAPPA hyperparameter assessment, the same full calibration spatial frequencies and $f_{calib} = Wf_l$ model are used like in GRAPPA reconstruction, but each spatial frequency point is treated differently than GRAPPA. As shown in Figure 3.4, the calibration spatial frequencies f_{calib} for BGRAPPA

are in the location of the data points where the acquired spatial frequencies are in the actual fMRI experiment. For GRAPPA, these data points are assigned to the f_l variable in the $f_{calib} = W_c f_l$ model shown at the bottom of Figure 3.4. Using Eq. 3.1, this will result in the prior for the weights in BGRAPPA, D_0, to be different than the estimated weights utilized in GRAPPA image reconstruction. The f_l points used for estimating the prior mean for the weights are averaged to obtain the prior mean of the unacquired spatial frequencies, f_{k0}.

The hyperparameters n_k and n_w, which are the prior scalars of the prior means, are assessed to be the number of calibration time points n_{cal}. The average residual k-space variance over the coil spatial frequency arrays is calculated to obtain a prior mean for the residual k-space variance τ_0^2. The hyperparameters α_k (shape parameter of the inverse gamma) and δ (scale parameter of the inverse gamma) are assessed to be $\alpha_k = n_{cal} - 1$ and $\delta = (n_{cal} - 1)\tau_0^2$.

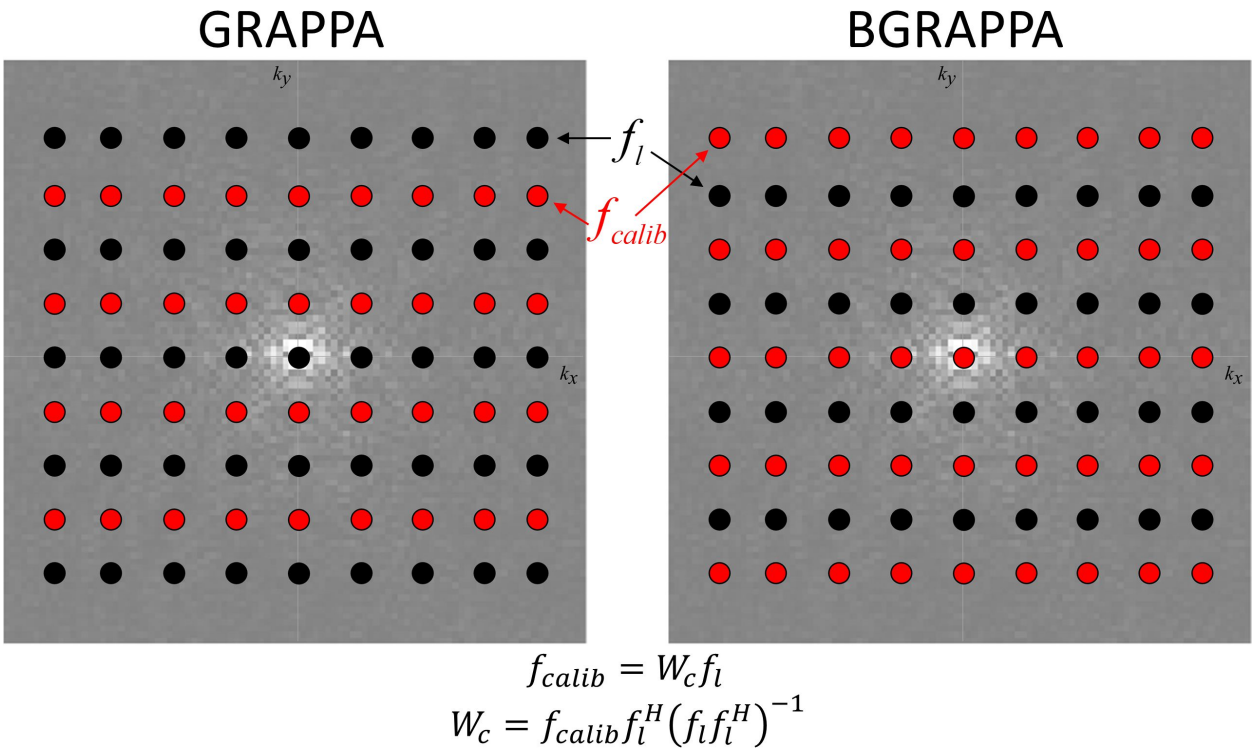

Figure 3.4: Full calibration k-space arrays that indicate which data points are used as f_{calib} points and the f_l points for GRAPPA (left) and BGRAPPA (right).

This prior information is incorporated to estimate the unacquired spatial frequencies in the subsampled k-space arrays.

3.3.3 Parameter Estimation

Using the posterior distribution in Eq. 3.9 with priors described in Eqs. 3.6, 3.7, and 3.8 along with the likelihood distribution 3.5, the MAP estimate for the unacquired spatial frequencies f_k, the weights W, and the residual k-space variance τ^2 is estimated via the Iterated Conditional Modes (ICM) optimization algorithm (Lindley and Smith, 1972; O'Hagan, 1994) and the MCMC Gibbs sampler (Geman and Geman, 1984; Gelfand and Smith, 1990) for the marginal posterior estimates. Beginning with the prior means for each parameter as initial estimates, the ICM algorithm iterates over the parameters, calculating its posterior conditional mode until convergence at the joint posterior mode. Similar to the ICM algorithm used for BSENSE, the ICM will produce the global maximum, the MAP, instead of the local maximum since each of the posterior conditionals are unimodal. The posterior conditional modes are

$$\hat{f}_k = (W'W + n_k I_{2p})^{-1}(W' f_e + n_k f_{k0}), \tag{3.10}$$

$$\hat{D} = (F_e F_k' + n_w D_0)(F_k F_k' + n_w I_{2p})^{-1}, \tag{3.11}$$

$$\hat{\tau}^2 = \frac{\Phi}{2(2n_C + 2p + 2n_C p + 1)}, \tag{3.12}$$

where $\Phi = (f_e - W f_k)'(f_e - W f_k) + n_k(f_k - f_{k0})'(f_k - f_{k0}) + \alpha_k \delta + n_w tr[(D - D_0)(D - D_0)']$, $F_e = [f_{eR},\ f_{eI}]$ and $F_k \in \mathbb{R}^{2p \times 2}$ is a skew symmetric matrix representation of the unaliased voxel values f_k as expressed by

$$F_k = \left[\begin{array}{c:c} f_{kR} & f_{kI} \\ \hdashline -f_{kI} & f_{kR} \end{array}\right]. \tag{3.13}$$

It can be shown that the full conditional distributions of each parameters f_k, D, and τ^2 are given by

$$f_k|W, \tau^2, f_e \sim N\{\hat{f}_k, \tau^2(W'W + n_k I_{2p})^{-1}\}, \tag{3.14}$$

$$D|f_k, \tau^2, f_e \sim MN\{\hat{D}, \tau^2(F_k'F_k + n_w I_{2p})^{-1}\}, \tag{3.15}$$

$$\tau^2|f_k, W, f_e \sim IG\{\alpha_{k*}, \delta_*\}, \tag{3.16}$$

where $\alpha_{k*} = n_C p + n_C + p + \alpha_k$ and $\delta_* = [(f_e - Wf_k)'(f_e - Wf_k) + n_k(f_k - f_{k0})'(f_k - f_{k0}) + n_W tr((D - D_0)(D - D_0)') + 2\delta]/2$. The Gibbs sampler uses the posterior conditionals to generate the entire distribution for each parameter at each time point yielding more information that can be used for statistical analysis. However, the computation time is longer compared to using an iterative maximum *a posteriori* (MAP) method. Since the posterior conditional distribution for both the unacquired spatial frequencies f_{k0} and the weights W are normally distributed, the mean and mode would theoretically be equal. If we use the MCMC Gibbs sampler, we would only be interested in the mean of the distributions. To save practical computational expense, for this dissertation, we only use the MAP estimate via the ICM for estimating the unacquired spatial frequencies f_{k0} and the weights W.

CHAPTER 4: Bayesian Fused GRAPPA/SENSE

In Chapter 2, we discussed SENSE image reconstruction and introduced a Bayesian approach (BSENSE) and in Chapter 3, we discussed GRAPPA image reconstruction, introducing a Bayesian approach to GRAPPA (BGRAPPA) as well. For this chapter, we look at a fused GRAPPA/SENSE reconstruction process. Since GRAPPA operates in the spatial frequency domain and SENSE operates in the image domain, we can combine these two techniques to reconstruct subsampled coil k-space arrays into a full FOV brain image. We then apply a Bayesian approach to this Fused GRAPPA/SENSE technique.

4.1 Fused GRAPPA/SENSE

4.1.1 Reconstruction Process

Multiple steps are required to properly fuse both GRAPPA and SENSE together. Figure 4.1 demonstrates the flowchart of how the subsampled spatial frequencies will be reconstructed into a single full FOV brain image using this Fused GRAPPA/SENSE technique. There are still the pre-scan calibration spatial frequency arrays in step 1 that are utilized for estimating the weight, W_c, for GRAPPA and the coil sensitivities, S, for SENSE (step 2). Step 3 of the process is then to estimate all the unacquired spatial frequencies using GRAPPA, at a single time point, yielding full coil k-space arrays. The full coil k-space arrays are then inverse Fourier transformed in full coil-weighted images (step 4). Then SENSE reconstruction is utilized to combine the full coil images into a single composite brain image (steps 5 and 6). This process is repeated at each time point in the subsampled time series of coil spatial frequency arrays.

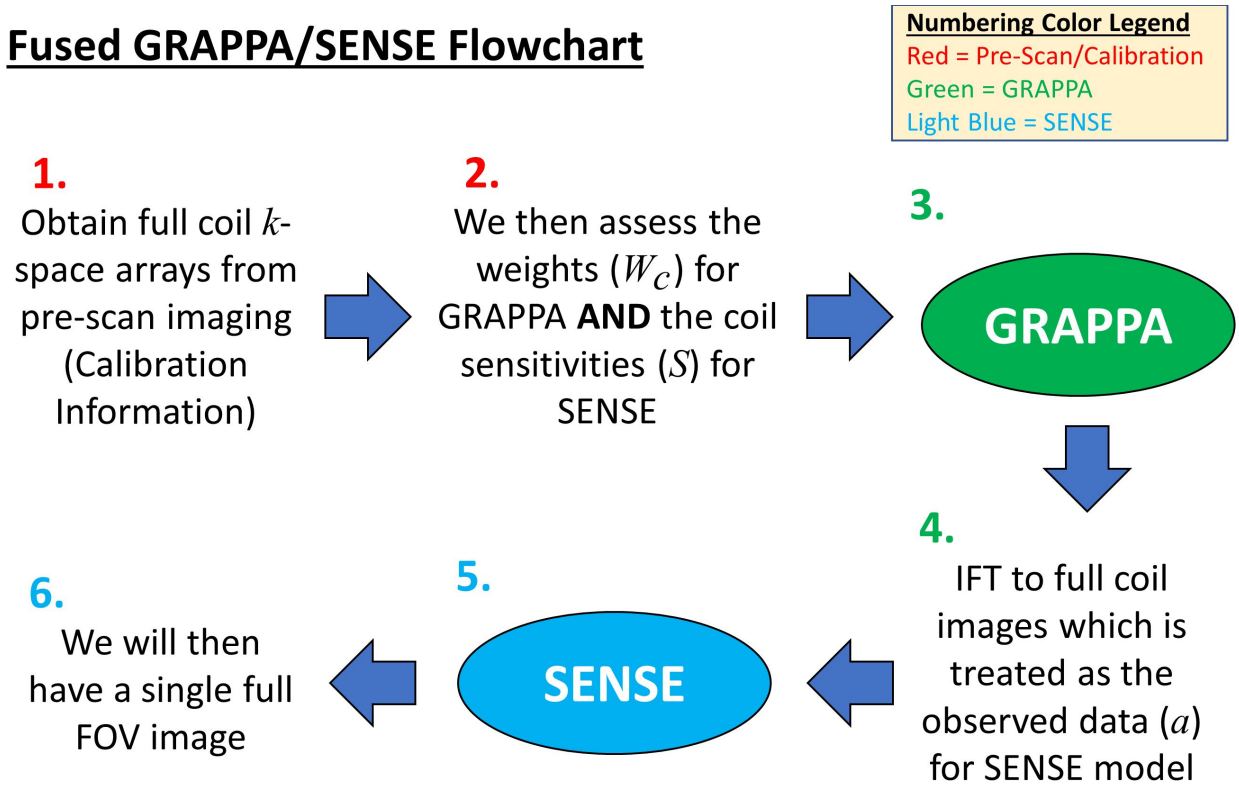

Figure 4.1: Flow chart for the BGRAPPA/BSENSE combination model for image reconstruction.

4.1.2 Model

The model for the Fused GRAPPA/SENSE technique begins with the GRAPPA model outlined in Section 3.1.2. That is ${f_{ec}}^{(\omega)} = {W_c}^{(\omega)} {f_{kc}}^{(\omega)} + {\eta_{ec}}^{(\omega)}$ where $\omega = 1, ..., K$, $f_{ec} \in \mathbb{C}^{n_C \times 1}$ is the complex-valued interpolated k-space values, $f_{kc} \in \mathbb{C}^{p \times 1}$ is the complex-valued acquired k-space values, and $\eta_c \in \mathbb{C}^{n_C \times 1}$ is the additive complex-valued noise with $\eta_c \sim N(0, \tau^2(1+i))$. The interpolated spatial frequencies, f_{ec}, are then placed in the respectively locations of the missing k-space values resulting in full coil k-space arrays, f_{full}.

The full coil k-space arrays f_{full} are then inverse Fourier transformed into full coil images. The SENSE model is then applied to the full coil image measurements with no acceleration factor, $n_A = 1$, as described in Section 2.1.2. That is ${a_c}^{(\nu)} = {S_c}^{(\nu)} {v_c}^{(\nu)} + {\varepsilon_c}^{(\nu)}$, where $\nu = 1, ..., M$, $a_c \in \mathbb{C}^{n_C \times 1}$ is the complex-valued coil measurements, $S_c \in \mathbb{C}^{n_C \times 1}$ is

the matrix of complex-valued coil sensitivities, $v_c \in \mathbb{C}$ is the complex-valued unaliased voxel value, $\varepsilon_c \in \mathbb{C}^{n_C \times 1}$ is the additive complex-valued noise where $\varepsilon_c \sim N(0, \sigma^2(1+i))$, and M is the total number of voxels in the full image.

4.2 Bayesian Fused GRAPPA/SENSE Technique

4.2.1 Data Likelihood, Prior and Posterior Distributions

For the Bayesian approach to Fused GRAPPA/SENSE, we treat the unacquired spatial frequencies f_k, the weights W, the residual k-space variance τ^2, the unaliased voxel values v, the coil sensitivities H, and the residual image variance σ^2 as unknown parameters that are dependent on the acquired spatial frequencies f_e. The priors for each of these parameters (Eqs. 2.9, 2.10, 2.11, 3.6, 3.7, and 3.8) along with the likelihood equations (Eqs. 2.8 and 3.5) are combined to produce the joint posterior distribution as expressed in Eq. 4.1.

$$P(V_k, H, \Sigma, D, F_{k*}, T|F_{e*}) \propto P(V_k, H, \Sigma|F_{full})P(F_{k*}, D, T|F_{e*}), \tag{4.1}$$

where $V_k = (v_1, ..., v_M)$ is the vector of unaliased voxel values, $H = I_M \bigotimes (H_1, ..., H_M)$ is the matrix of coil sensitivities, $\Sigma = (\sigma_1^2, ..., \sigma_M^2)$ is the vector of residual noise variances, $F_{k*} = (f_{k1}, ..., f_{kL})$ is the vector of unacquired spatial frequencies, $D = I_L \bigotimes (D_1, ..., D_L)$ is the matrix of localized weights, $T = (T_1, ..., T_L)$ is the vector of k-space noise variance, $F_{e*} = (f_{e1}, ..., f_{eJ}))$ is the vector of acquired spatial frequencies, F_{full} is a vector of the acquired spatial frequencies f_e and the f_k spatial frequencies after interpolation, M is the total number of voxels in the full image, L is the number of unacquired spatial frequencies, and J is the number of acquired spatial frequencies.

The $P(F_{k*}, D, T|F_{e*})$ is the posterior distribution of our BGRAPPA technique and the

$P(V_k, H, \Sigma|F_{full})$ is the posterior distribution of our BSENSE technique. With the BSENSE posterior portion of being dependent on full coil k-space arrays F_{full}, we must first estimate the unacquired spatial frequency values using BGRAPPA. Then the interpolated spatial frequencies are appended with the acquired spatial frequencies yielding full coil k-space arrays. After applying the IFT to the full coil k-space arrays F_{full}, our BSENSE technique is then used to complete the image reconstruction process for the Bayesian Fused GRAPPA/SENSE.

4.2.2 Hyperparameter Determination

The hyperparameter determination for our BGRAPPA technique portion of the Bayesian Fused GRAPPA/SENSE follows the assessment outlined in Section 3.3.2. For the BSENSE portion of the Bayesian Fused technique, the hyperparameter determinations follows the assessment outlined in Section 2.3.2. The information for both hyperparameter assessments comes from the same n_{cal} calibration time points. The full coil calibration k-space arrays are used for the BGRAPPA part, and the full coil calibration images, after IFT, are used for the BSENSE part.

4.2.3 Parameter Estimation

The parameter estimation for the BGRAPPA part of the Bayesian Fused technique follows the estimation outlined in Section 3.3.3. This means that the unacquired spatial frequencies f_k, the localized weights W, and the k-space noise variance τ^2 have the same posterior conditional modes and posterior conditional distributions as expressed in equations 3.10, 3.11, 3.12, 3.14, 3.15, and 3.16 respectively.

For the BSENSE part, the parameter estimation follows the estimation process outlined in Section 2.3.3. However, since the coil measurements are full images after the IFT, the

acceleration factor would be $n_A = 1$. This makes the posterior conditional modes to be

$$\hat{v} = (S'S + n_v I_2)^{-1}(S'a + n_v v_0), \tag{4.2}$$

$$\hat{H} = (V'V + n_S I_2)^{-1}(VY' + n_S H_0), \tag{4.3}$$

$$\hat{\sigma}^2 = \frac{\Theta}{2(4n_C + \alpha + 3)}, \tag{4.4}$$

where $\Theta = (a - Sv)'(a - Sv) + n_v(v - v_0)'(v - v_0) + \alpha\beta + n_S tr[(H - H_0)(H - H_0)']$, $Y = [a_R, a_I]$ and $V \in \mathbb{R}^{2\times 2}$ is a skew symmetric matrix representation of the unaliased voxel values v as expressed in Eq. 2.16.

With an acceleration factor of one, the posterior conditional distributions become

$$v|S, \sigma^2, a \sim N\{\hat{v}, \sigma^2(S'S + n_v I_2)^{-1}\}, \tag{4.5}$$

$$H|v, \sigma^2, a \sim MN\{\hat{H}, \sigma^2(V'V + n_S I_2)^{-1}\}, \tag{4.6}$$

$$\sigma^2|v, S, a \sim IG\{\alpha_*, \beta_*\}, \tag{4.7}$$

where $\alpha_* = 2n_C + \alpha + 1$ and $\beta_* = [(a - Sv)'(a - Sv) + n_v(v - v_0)'(v - v_0) + n_S tr((H - H_0)(H - H_0)') + 2\beta]/2$.

CHAPTER 5: Reconstruction Results

The software used for this research was MATLAB 2022b run on a 12th Gen Intel(R) Core(TM) i7-1255U laptop computer with 16GB RAM, operating on Windows 11.

5.1 Simulation FMRI Study

5.1.1 Non-Task Data Generation

A noiseless non-task image was used to create two series of 510 simulated full FOV coil images for one slice to mimic the experimental data shown in this Section 5.2.1. The last n_{cal} time points of the first time series of non-task images served as pre-scan calibration information that was utilized for hyperparameter assessment, and the second time series was used for a simulated non-task experiment. A complex-valued image was multiplied by a designed sensitivity map with $n_C = 8$ coils, similar to the four-channel coil shown in Figure 2.3 but with four additional coils in each corner as well. Figure 5.1 illustrates the real and imaginary parts of the full simulated brain image (first and second column) being voxel-wise multiplied by the real and imaginary components of the sensitivities for each of the $n_C = 8$ coils (third and fourth column). This results in the real and imaginary components of the complex-valued full coil weighted images (fifth and sixth column).

In real-world MRI experiments, the first few images in an fMRI time series have increased signal as the magnetization reaches a stable state. To mimic this, the first three of both non-task time series of $n_{TR} = 510$ time points of the simulated non-task time series were scaled with the signal slightly decreasing from the first to the third time point before reaching a stable signal in the fourth time point. The scaling was determined by dividing the first three images of the experimental data by the 21st image, separately. After dividing the

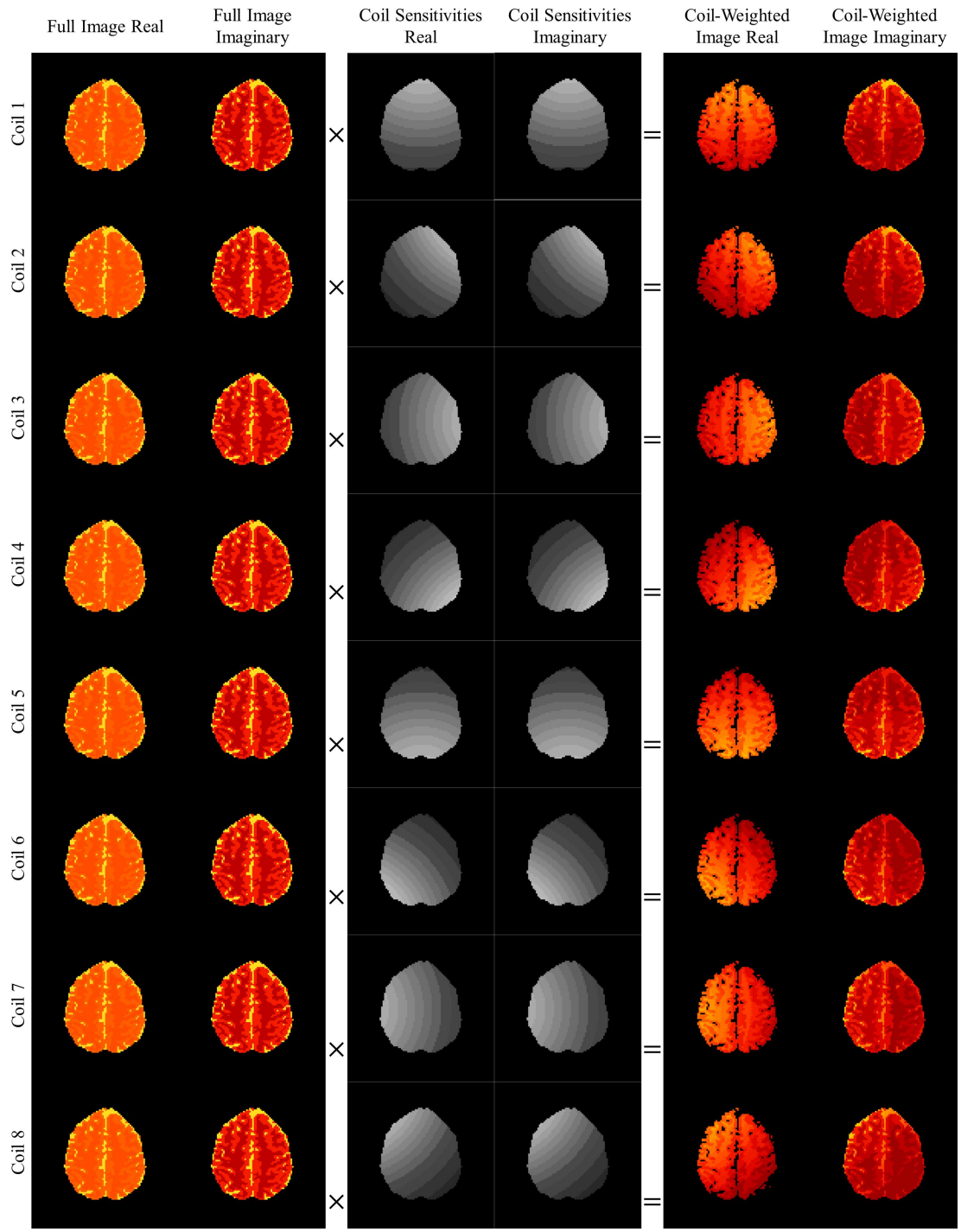

Figure 5.1: Real and imaginary components of the true complex-valued simulated image (first and second column) voxel-wise multiplied by the real and imaginary components of the complex-valued coil sensitivities for each of the $n_C = 8$ coils (third and fourth column) yielding the real and imaginary components of the complex-valued coil-weighted images (fifth and sixth column).

three images, the signal increase for each tissue type (cerebrospinal fluid (CSF), gray matter, and white matter) was averaged together for each of the three divided images, calculating the average signal increase for each matter type. For example, the average signal increase in the first image for the CSF was 75%, 55% for the gray matter and 35% for the white matter giving multiplication factors of 1.75, 1.55, and 1.35 for the matter types, respectively. This process was repeated for the second (with multiplication factors of 1.55, 1.40, and 1.20 respectively) and third (with multiplication factors of 1.40, 1.25, and 1.10 respectively) images in the series with the multiplication factors decreasing from the first to the third image.

The series of images for both the non-task calibration images and the full, simulated images were then Fourier transformed into noiseless full coil k-space arrays. The time series of the coil k-space arrays were simulated by adding separate $N(0, 0.0036 n_y n_x)$ noise, where n_y and n_x are the number of rows and columns, respectively, in the full k-space array, to the real and imaginary parts of the full coil k-space arrays, corresponding to the noise in the real-world fMRI experimental data. To mimic the fMRI experiment, the first 20 time points of the second time series were omitted leaving 490 time points of the spatial frequency arrays for the single slice. However, the first 10 time points of an fMRI experiment can be used to estimate a T_1 map which efficiently segments the different tissue types. The next 10 time points can be utilized to estimate a static magnetic field map to adjust for geometric distortions (Karaman et al., 2015). The remaining 490 time points in the time series were subsampled by censoring lines in k-space according to a determined acceleration factor. An example of the real and imaginary components of the subsampled k-space arrays for $n_C = 8$ coils and an acceleration factor of $n_A = 3$ at one time point is exhibited in Figure 5.2a. The respective aliased coils images after the IFT are displayed in Figure 5.2b. For SENSE and BSENSE, reconstruction will start from the aliased coil images as depicted in Figure 5.2b since both techniques operate in image space while the other techniques start

the reconstruction process in the k-space domain.

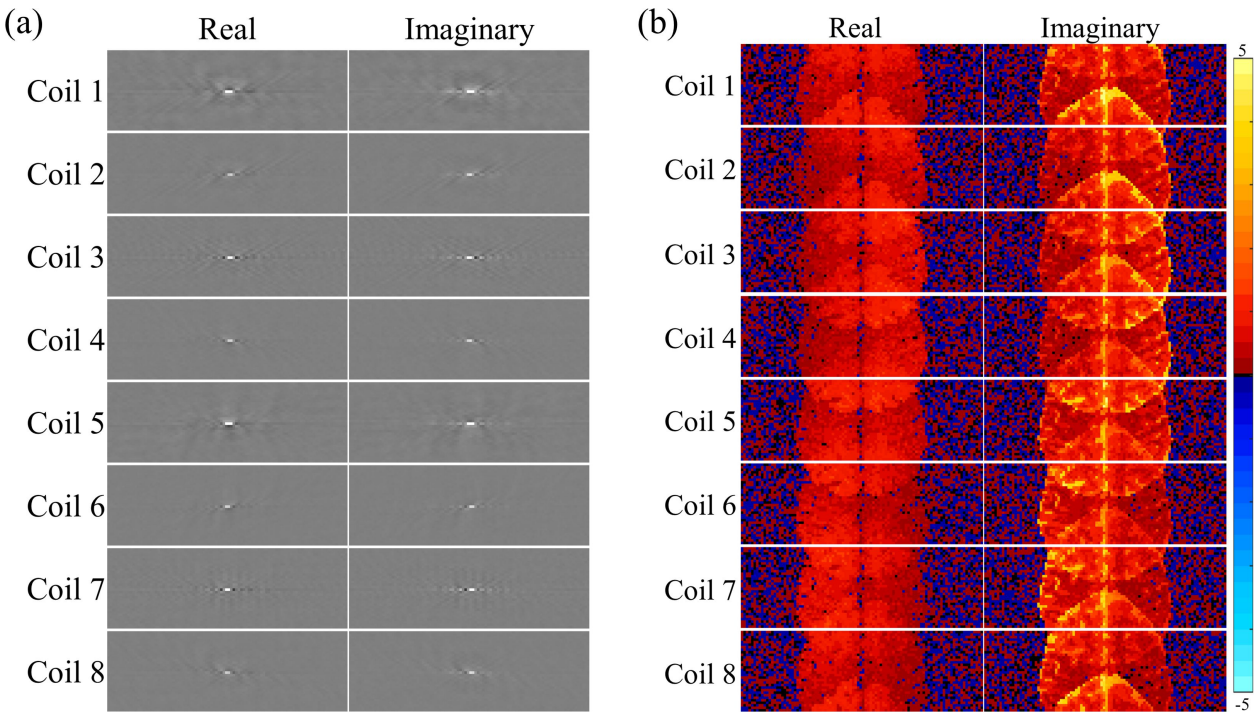

Figure 5.2: (a) The real and imaginary components of the simulated acquired noisy subsampled coil spatial frequency arrays for the first time point in the non-task time series with an acceleration factor of $n_A = 3$ and (b) the respective aliased coil measurements after applying the IFT.

5.1.2 Non-Task Reconstruction Results

To analyze the reconstruction performance of the traditional image reconstruction techniques and our proposed Bayesian approaches, we first reconstructed the subsampled coil k-space arrays at one time point, giving us a single unaliased image for each method. For this, we used the first time point of the 490 simulated non-task time series with an acceleration factor of $n_A = 3$.

The last $n_{cal} = 30$ time points, corresponding to 30 seconds, from the first 510 non-task full FOV calibration time series were utilized to assess the hyperparameters. For BGRAPPA, the prior means from the calibration information for the unacquired spatial frequency arrays f_{k0} and the localized weights D_0 were used as initial values for f_k and D. These initial values

were used to generate a τ^2 value from the posterior conditional mode (Eq. 3.12) and the posterior conditional distribution (Eq. 3.16), initializing the ICM optimization algorithm and the Gibbs sampler. For BSENSE, the prior means from the calibration images, after IFT, for the unaliased voxels v_0 and the sensitivity coils H_0 were used as initial values for v and H. These initial values were used to generate a σ^2 value from the posterior conditional mode (Eq. 2.15) and the posterior conditional distribution (Eq. 4.7), initializing the ICM algorithm and the Gibbs sampler, respectively. The hyperparameters for BGRAPPA and BSENSE were the same hyperparameters utilized for BFused, but only the MAP estimate was used for BFused.

Before analyzing the reconstruction results comparing the traditional reconstruction

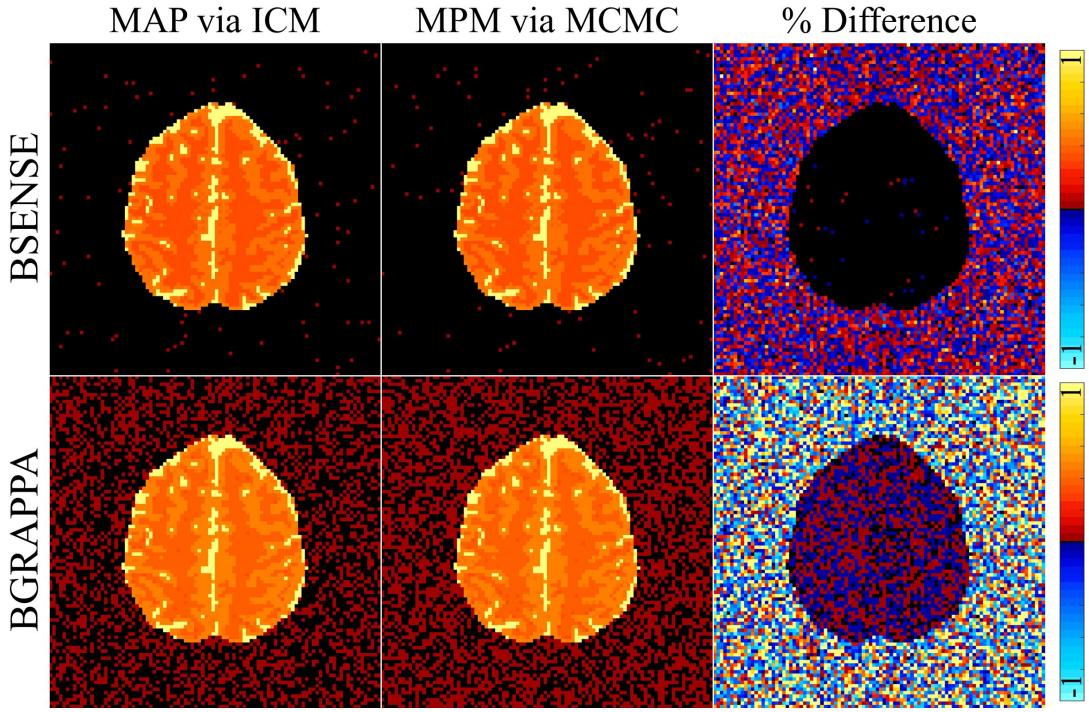

Figure 5.3: BSENSE (top row) and BGRAPPA (bottom row) reconstructed non-task magnitude images with an acceleration factor of $n_A = 3$ using the ICM to calculate the MAP estimate (first column) and the Gibbs sampler to estimate the MPM for both techniques (second column). The voxel-by-voxel percent difference between the MAP estimate and MPM estimate for both techniques is displayed in the images in the third column. Note, the minimum and maximum for the percent difference scale, shown in the color bar on the left, is -1% and 1% respectively.

techniques to our Bayesian approaches, we will first look at results comparing the MAP estimate from the ICM algorithm and the MPM from the MCMC Gibbs sampler for both BSENSE and BGRAPPA. For the ICM algorithm, only three iterations were needed for estimating the parameters and for the Gibbs sampling, 10,000 total iterations were run with a burn of 2,500 leaving 7,500 iterations for estimation. The computation time for the ICM was about 0.10 seconds for BSENSE and 0.50 seconds for BGRAPPA per time point. The computation time for the Gibbs sampler was about 90 seconds for BSENSE and 370 seconds for BGRAPPA per time point. In Figure 5.3, the magnitude of the reconstructed images for both techniques are displayed, top row for BSENSE and bottom row for BGRAPPA, with the percent difference between the images in the third column. The anatomical structure for both parameter estimation methods are similar when comparing the first column and second column for both reconstruction techniques. This is further shown by the percent difference images in the third column of Figure 5.3. With the scale for both images being -1% to 1%, we can see that the difference inside the brain is very close to 0%, meaning the MAP and MPM estimates produce very similar results. This is expected since both the unaliased voxel values v from BSENSE and the unacquired spatial frequencies f_k are normally distributed. With the normal distribution, the mean and mode are equal i.e. the MAP estimate and the MPM estimate would theoretically be the same. For the rest of this dissertation, we will only use the MAP estimate via the ICM algorithm to reconstruct the subsampled coil k-space arrays for the BSENSE, BGRAPPA, and BFused reconstruction techniques.

Figure 5.4 displays the true noiseless simulated magnitude image (first row, first column) along with the reference magnitude image (second row, first column). This reference image was determined by simply averaging the full, noisy coil k-space arrays in the time series yielding a single spatial frequency array and then applying the IFT resulting in a full complex-valued brain image. This provides us what image reconstruction would look like without

applying an acceleration factor for BGRAPPA and GRAPPA. Averaging of the full k-space arrays causes the signal across the image to decrease which explains the two different color bars in Figure 5.4. This means that the reference images and the BGRAPPA and GRAPPA reconstructed images will not accurately illustrate the true signal intensities but can still be utilized for other fMRI analysis as shown throughout this chapter.

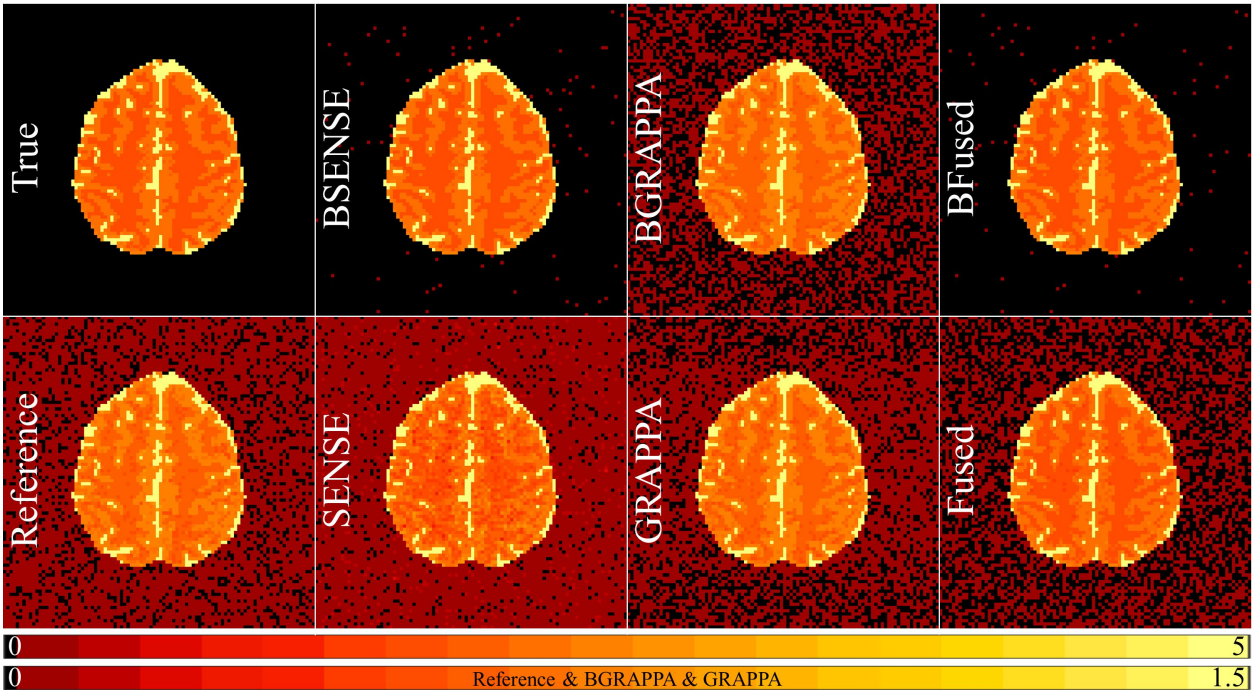

Figure 5.4: True non-task magnitude image (first row, first column), reference non-task magnitude reconstructed image (second row, first column), the Bayesian reconstructed magnitude images (first row, columns 2-4) and magnitude images from the traditional reconstruction techniques (second row, columns 2-4). The top color bar shows the scale for the true magnitude, BSENSE, BFused, SENSE, and Fused techniques while the bottom color bar shows the scale for the reference magnitude, BGRAPPA, and GRAPPA techniques.

Figure 5.4 also shows the magnitude of the reconstructed images for the traditional techniques (second row, column 2-4) and the respective Bayesian approaches (first row, columns 2-4) for the first time point in the simulated non-task series. We can see that the joint MAP estimate from BSENSE and BFused produce magnitude images that closely resemble the true non-aliased image inside the brain in Figure 5.4 (first row, first column)

with the SENSE and Fused techniques producing noisier magnitude images. Outside the brain, the noise level is noticeably higher for SENSE and Fused reconstruction compared to BSENSE and BFused magnitude reconstructed images. Visually the BGRAPPA image is slightly more accurate and less noisy than the GRAPPA image when compared to the reference image (second row, first column).

Figure 5.5 shows the true noiseless simulated phase image (first row, first column), the reference phase image (second row, first column), the phase of the reconstructed images for the traditional techniques (second row, column 2-4) and the respective Bayesian approaches (first row, columns 2-4) for the first time point in the simulated non-task series. The joint MAP estimate from BSENSE and BFused produce phase images that closely resemble the true simulated phase image inside the brain. Figure 5.5 shows that the SENSE

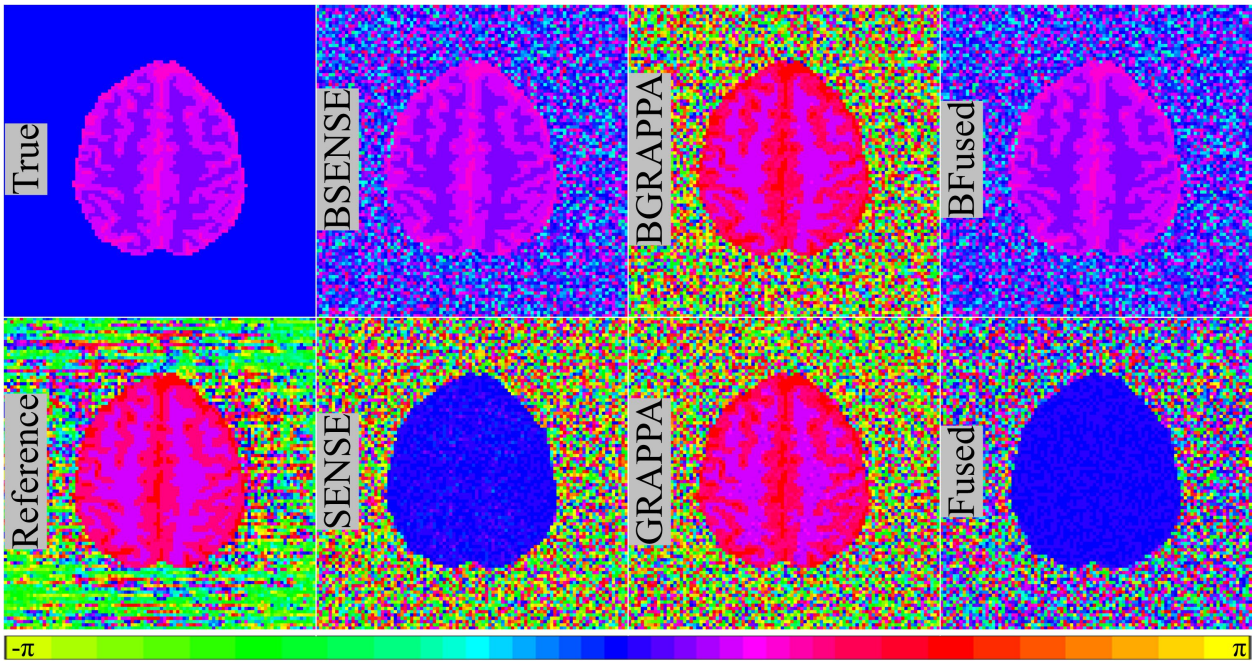

Figure 5.5: True non-task phase image (first row, first column), reference non-task phase reconstructed image (second row, first column), the Bayesian reconstructed phase images (first row, columns 2-4) and phase images from the traditional reconstruction techniques (second row, columns 2-4). Due to the circular nature of phase angles, the color bar for the phase images have wrap-around.

and Fused techniques produce phase images with no anatomical structure, showing that these techniques do not accurately maintain the complex-valued nature of MR images. The BGRAPPA and GRAPPA phase images appear to be similar to the reference phase image (second row, first column) in Figure 5.5. This reference phase image and the reconstructed phase images from BGRAPPA and GRAPPA illustrate again how averaging the full coil k-space arrays does not accurately represent the signal intensities and phase angles of the true complex-valued images.

To quantify the differences between the true or reference images and the reconstructed magnitude and phase images, we use the mean squared error, $MSE = \frac{1}{K}\sum_{j=1}^{K}(v_j - \overline{v}_j)^2$, where K is the number of voxels inside the brain in the full reconstructed image, v_j is the reconstructed magnitude or phase value of the jth voxel inside the brain, and $\overline{v}_j$ is the true magnitude or phase value of the jth voxel. This measure will indicate the accuracy of a single reconstructed image compared to the true simulated image or the reference image with lower MSE indicating a more accurate reconstructed image. The reference images were used to calculate the MSE for BGRAPPA and GRAPPA and the true simulated images were used for the other reconstruction techniques.

Figure 5.6a displays the MSE for each techniques' magnitude reconstructed image and Figure 5.6b shows the MSE for each techniques' phase reconstructed image. The BSENSE and BFused techniques had a markedly smaller magnitude MSE values than SENSE and the Fused techniques. BGRAPPA and GRAPPA had the smallest magnitude MSE values compared to the other techniques, with BGRAPPA having a slightly smaller MSE than GRAPPA, but is not the best measure for analyzing signal intensity. Evaluating the phase MSE values in Figure 5.6b, BSENSE and BFused had much smaller values compared to the other techniques. Like the magnitude MSE value comparison, the phase MSE value for BGRAPPA is slightly smaller than GRAPPA's phase MSE value.

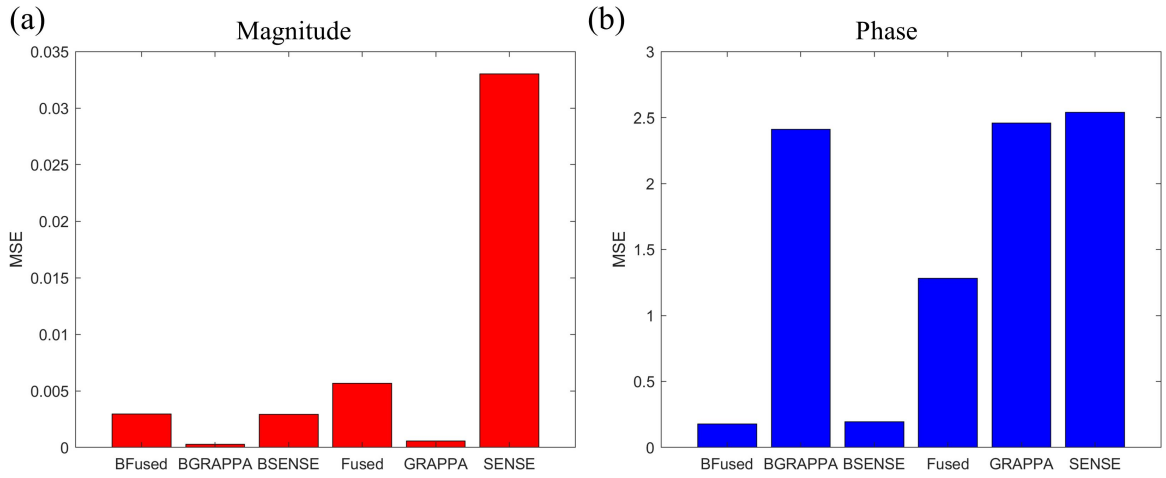

Figure 5.6: (a) MSE for inside the brain for the magnitude images of each of the reconstruction techniques and (b) the MSE for inside the brain for the phase reconstructed images. The BSENSE, BFused, SENSE, and Fused techniques were compared to the true simulated magnitude and phase images and BGRAPPA and GRAPPA were compared to the reference magnitude and phase images.

To further analyze the different reconstruction techniques, we reconstructed the entire series of $n_{IMG} = 490$ simulated non-task time series with an acceleration factor of $n_A = 3$.

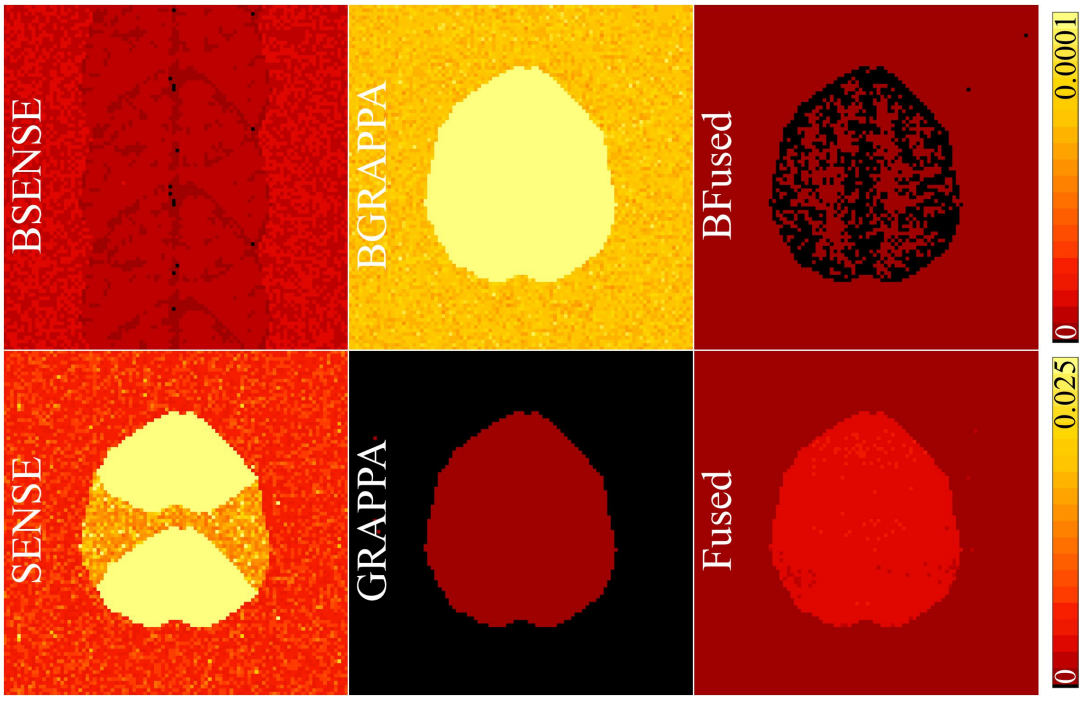

Figure 5.7: Temporal variance of the reconstructed $n_{IMG} = 490$ simulated non-task time series using the traditional techniques (bottom row) and the respective Bayesian approaches (top row).

Figure 5.7 displays the temporal variance of each reconstruction technique for non-task time series. The top row shows the Bayesian reconstruction techniques while the bottom row shows the traditional reconstruction techniques. Note how the scales for the top and bottom row are different. The top row only goes up to 0.0001 while the bottom row goes to 0.025 which is 249 times larger which shows that the Bayesian techniques have a much smaller temporal variance. This indicates a more accurate reconstruction through time. Of the three Bayesian approaches, the BFused technique had the smallest temporal variance with BGRAPPA having the largest. For the traditional techniques, SENSE had the largest temporal variance while GRAPPA had the smallest.

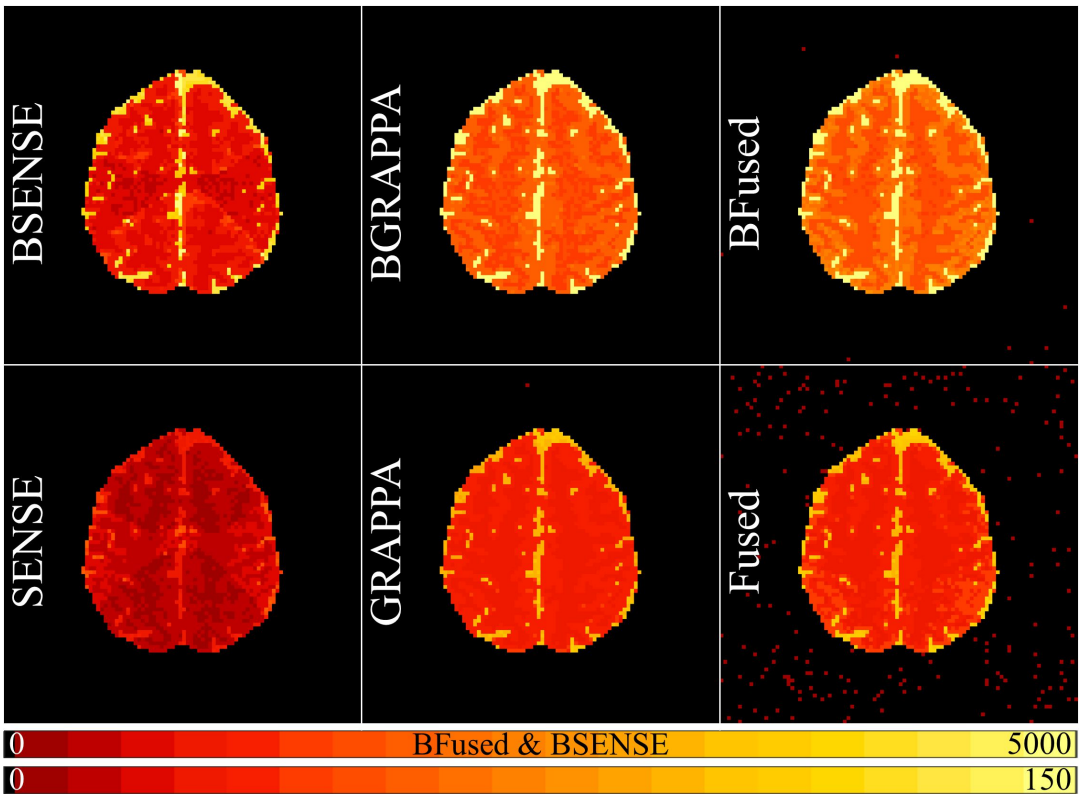

Figure 5.8: Signal-to-noise ratio of the reconstructed $n_{IMG} = 490$ simulated non-task time series using the traditional techniques (bottom row) and the respective Bayesian approaches (top row). The top color bar shows the scale for the BSENSE and BFused techniques while the bottom color bar shows the scale for the other techniques.

With the temporal variance, we can see how it directly affects the signal-to-noise ratio

(SNR) where $SNR = \beta_0/\sigma$, β_0 is the magnitude signal in each voxel, and σ is the temporal standard deviation in each voxel. The higher the SNR value, the less the noise affects the reconstruction of the subsampled coil k-space arrays. The SNR results for each reconstruction technique is displayed in Figure 5.8. The top row of the figure displays the SNR values for the Bayesian techniques, and the bottom row shows the SNR values of the traditional reconstruction techniques. In Figure 5.8, we have one scale that goes up to 5000 for the SNR values from the BSENSE and BFused techniques while the other scale goes up to 150 for the SNR values from the other techniques. This indicates that the BSENSE and BFused have considerably higher SNR values with BFused having the highest SNR values of the two. With the techniques on the 150 scale, BGRAPPA has the highest SNR values showing that the Bayesian approaches have improved SNR results over the traditional techniques.

Next, we evaluated how the number of calibration time points, n_{cal}, affected the reconstructed images. For the pre-scan calibration analysis, we fixed the acceleration factor to be $n_A = 3$ for the subsampled k-space coil arrays of the simulated non-task time series with $n_{IMG} = 490$ time points. Then we set the number of calibration time points to be $n_{cal} = 5, 10, 15, 20, 25, 30$ for separate hyperparameter assessments. After assessing the hyperparameters using each number of calibration time points, the simulated non-task time series with the subsampled coil spatial frequency arrays were reconstructed using the traditional and Bayesian reconstruction techniques.

The results for the magnitude reconstructed images using a various number of calibration time points from each technique are displayed in Figure 5.9. We can see that increasing the number of calibration time points decreases the noise level for the BSENSE and BFused techniques and slightly for the Fused technique. It appears that GRAPPA, BGRAPPA, and SENSE are unaffected by the number of calibration time points utilized for hyperparameter assessment.

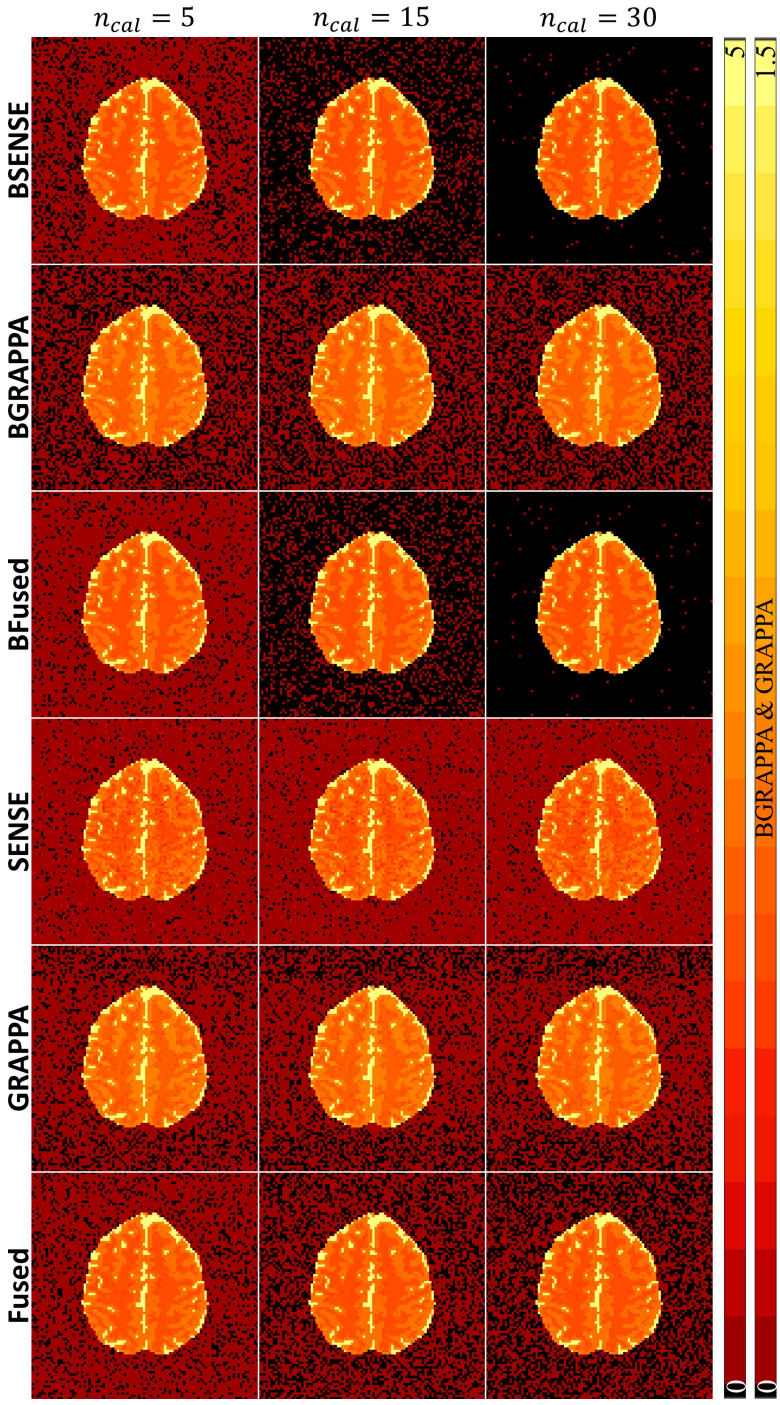

Figure 5.9: Reconstructed magnitude images for different number of calibration time points using the traditional and Bayesian image reconstruction techniques. The left color bar shows the scale for the true magnitude, BSENSE, BFused, SENSE, and Fused techniques while the right color bar shows the scale for the reference magnitude, BGRAPPA, and GRAPPA techniques.

The MSE for inside the brain along with the entropy for each of the reconstruction techniques using different number of calibration time points were calculated to quantify the results shown in Figure 5.9. Entropy analyzes uncertainty and smoothness across a single image with lower entropy meaning less uncertainty throughout the image. The equation for entropy is given by $E = -\sum_{j=1}^{N}\left[\frac{v_j}{v_{max}} ln\left(\frac{v_j}{v_{max}}\right)\right]$, where ln is the natural log, N is the number of voxels in the full reconstructed image, v_j is the reconstructed magnitude value of the jth voxel, and v_{max} is the voxel intensity if all the image intensities were in one pixel (Atkinson et al., 1997) given by $v_{max} = \sqrt{\sum_{j=1}^{N} {v_j}^2}$. Shown in Figure 5.10a, the MSE for BSENSE and BFused are very similar and much smaller than the SENSE and Fused techniques as they are compared to the true simulated magnitude image. Both BGRAPPA and GRAPPA have smaller MSE values than the rest of the reconstruction techniques, with BGRAPPA being the smallest, but are compared to the reference magnitude image. The MSE plot also shows that the MSE slightly decreases for the BSENSE, BFused, and Fused techniques while the others seem unaffected by the number of calibration images. For the

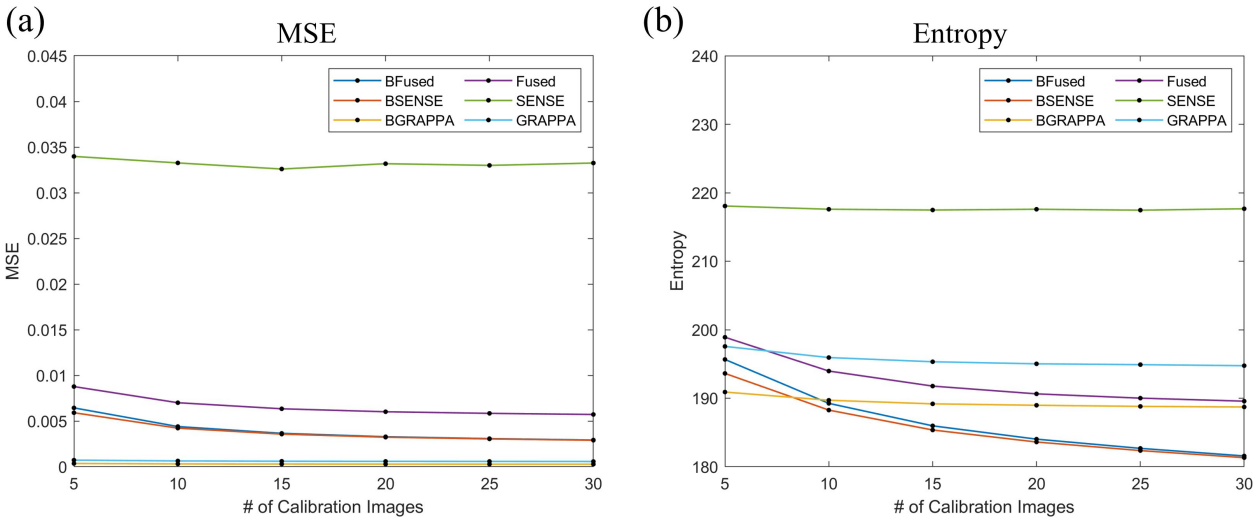

Figure 5.10: (a) MSE for inside the brain for each reconstruction technique compared to the true simulated or reference magnitude image for each number of calibration time points. (b) Entropy plot for each reconstruction technique using the various number of calibration time points. For both plots, BSENSE is the orange line, BGRAPPA is the yellow line, BFused is the blue line, SENSE is the green line, GRAPPA is the light blue line, and Fused is the purple line.

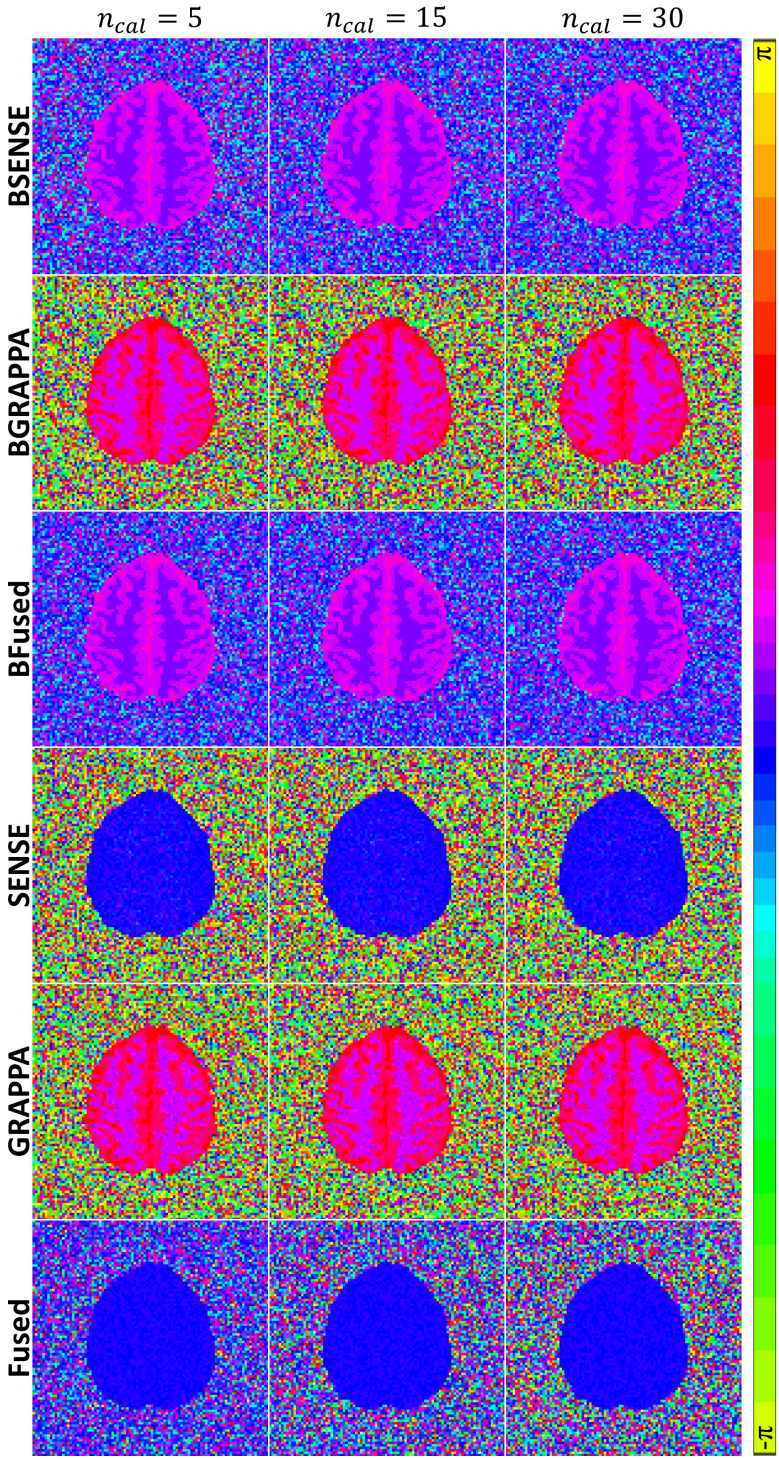

Figure 5.11: Reconstructed phase images for different number of calibration time points using the traditional and Bayesian image reconstruction techniques. Due to the circular nature of phase angles, the color bar for the phase images have wrap-around.

entropy plot in Figure 5.10b, the BSENSE and BFused have the smallest entropy values (except for $n_{cal} = 5$) with BSENSE being slightly smaller. This plot also shows that the Bayesian techniques all have smaller entropy values than the traditional techniques.

Like the magnitude images, we can also look at the phase of the reconstructed images for each reconstruction technique shown in Figure 5.11. Like Figure 5.5, BSENSE and BFused closely resemble the true simulated phase image, BGRAPPA and GRAPPA look similar to the reference phase image, and the SENSE and Fused techniques have values close to zero inside the brain for the phase. The results presented in Figure 5.11 show that increasing the number of calibration time points has a negligible effect on the phase of the reconstructed images.

Figure 5.12 displays the temporal variance for each reconstruction technique utilizing various calibration time points for hyperparameter determination. In this figure, there are two different scales for the color bars: one for the BSENSE and BFused techniques which go to 0.0001 and the other for the other techniques that go to 0.0125 which is 124 times larger. This difference in scales, like in Figure 5.7, shows that BSENSE and BFused have a markedly smaller temporal variance compared to the other reconstruction techniques with BFused having a much smaller temporal variance than BSENSE. For the other reconstruction techniques, BGRAPPA appears to have a slightly smaller temporal variance compared to GRAPPA with both being noticeably smaller than SENSE and the Fused techniques. This, again, shows that the Bayesian reconstruction techniques have a smaller temporal variance than the other techniques. From Figure 5.12, we can see that increasing the number of calibration time points decreases the temporal variance for the BSENSE and BFused while the effects appear to be imperceptible for the other reconstruction techniques.

Figure 5.13 displays the SNR images for each reconstruction technique using the different

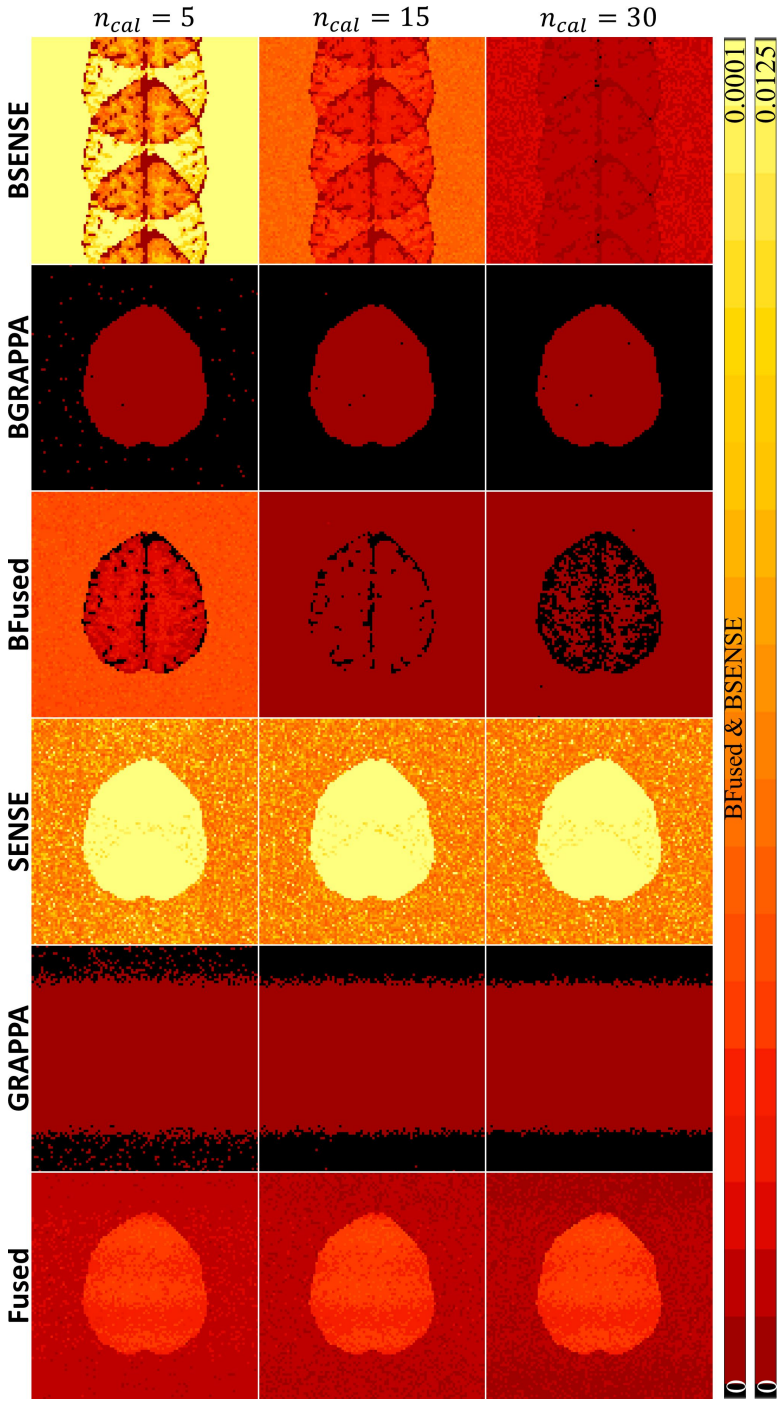

Figure 5.12: Temporal variance for different number of calibration time points using the traditional and Bayesian image reconstruction techniques. The left color bar shows the scale for the BSENSE and BFused techniques while the right color bar shows the scale for the other techniques.

number of calibration time points for the hyperparameter assessment. In Figure 5.13, there is one scale for the BSENSE and BFused techniques which go to 5000 and the other scale for the other techniques that go to 150. This scale difference shows that BSENSE and BFused have considerably higher SNR values compared to the other reconstruction techniques like in Figure 5.8. Between the two Bayesian reconstruction techniques, BFused has the higher SNR compared to BSENSE. For the other reconstruction techniques, BGRAPPA has distinctly higher SNR values compared to the traditional techniques which, again, shows that the Bayesian reconstruction techniques produce higher SNR values. From Figure 5.13, we can see that increasing the number of calibration time points increases the SNR inside the brain for the BSENSE and BFused. For the other techniques, the SNR values inside the brain appear unchanged as the calibration time points increase while decreasing SNR values outside for BGRAPPA, GRAPPA, and the Fused techniques.

For estimating priors of the Bayesian reconstruction techniques, we use up to 30 calibration image time points which are utilized to assess the hyperparameters. This means the same prior information is used at each time point when reconstructing the fMRI time series which could potentially lead to correlation with previously aliased voxels or task leakage. Task leakage is false detection of task in voxels that were previously aliased. To possibly mitigate this, we can randomly sample, without replacement, the calibration time points used at each time point in the fMRI time series. This means different hyperparameters are applied at each time point to the reconstruction of the aliased time series. We can also change the prior scalars n_v and n_S for the BSENSE and BFused techniques and the n_l and n_w scalars for the BGRAPPA and BFused techniques in the parameter estimation equations 2.13, 2.14, 2.15, 3.10, 3.11, 3.12, 4.2, 4.3, and 4.4 to be less than the number the calibration which decreases the weight of the prior information in the reconstructed images.

Figure 5.14a illustrates the average correlation between voxels and the voxels they were

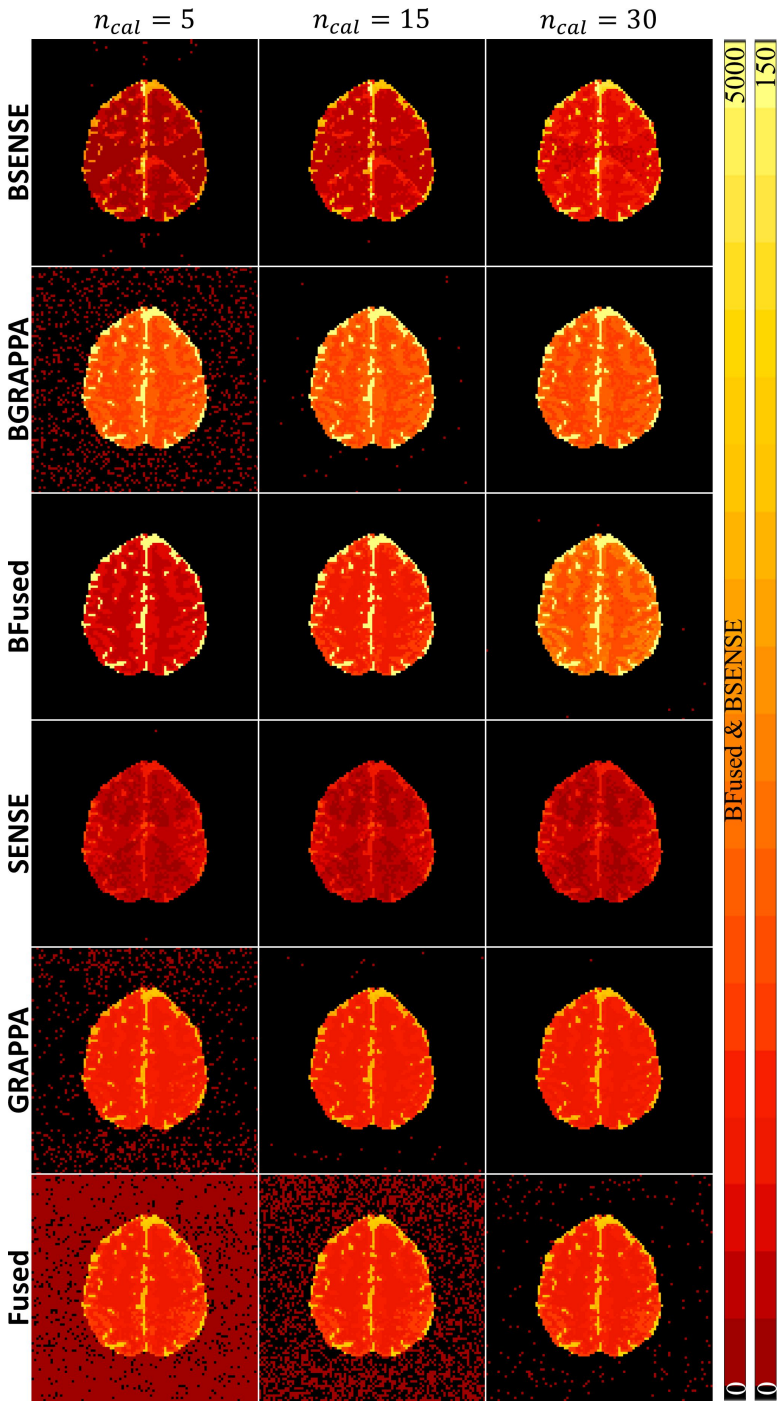

Figure 5.13: SNR for different number of calibration time points using the traditional and Bayesian image reconstruction techniques. The left color bar shows the scale for the BSENSE and BFused techniques while the right color bar shows the scale for the other techniques.

previously aliased for each reconstruction technique using different numbers of calibration time points for hyperparameter assessment. The magnitude of the reconstructed time series is used for the correlation estimation. Analyzing the plot shows that the traditional reconstruction techniques have lower correlation estimates than the Bayesian techniques. The GRAPPA and Fused techniques have the lowest correlations at or below 0.1 while the Bayesian techniques mostly range between 0.4 and 0.5. The correlation for BGRAPPA, GRAPPA, and SENSE decrease as the number of calibration time points increase. For BFused and BSENSE, the correlation slightly increases as the calibration time points increase while Fused remains relatively steady. This notably higher correlation with the Bayesian image reconstruction techniques motivates the utilization of sampling the calibration information at each time point in the series.

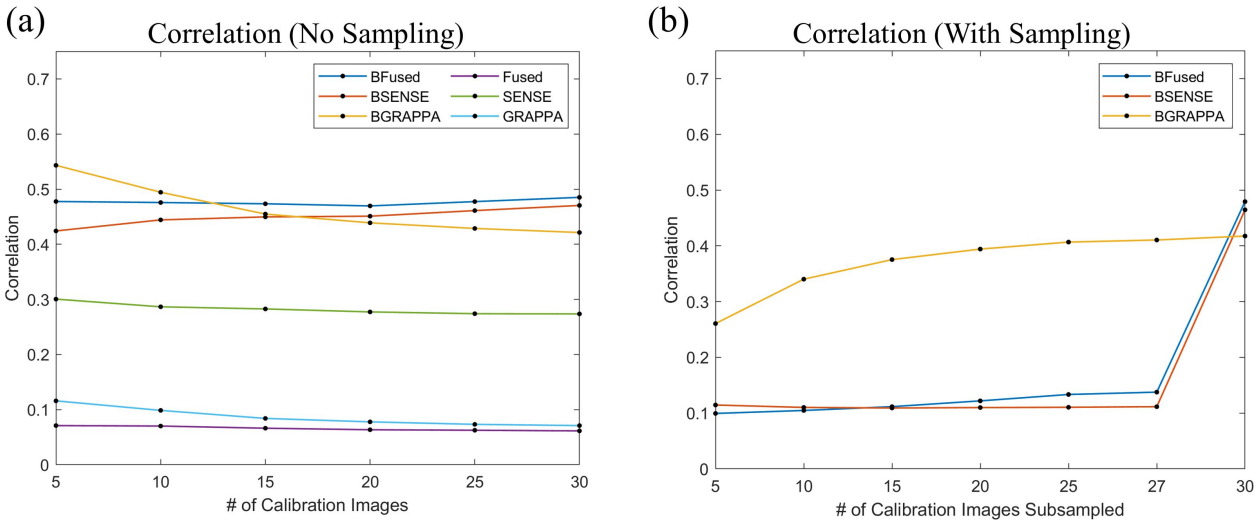

Figure 5.14: (a) Correlation between previously aliased voxels for each reconstruction technique. (b) Correlation between previously aliased voxels for each Bayesian reconstruction technique using sampling of the calibration time points without replacement. For plot a, BSENSE is the orange line (same in plot b), BGRAPPA is the yellow line (same in plot b), BFused is the blue line (same in plot b), SENSE is the green line, GRAPPA is the light blue line, and Fused is the purple line.

Figure 5.14b demonstrates the effects of sampling the calibration time points on voxel correlation while decreasing the prior scalars to $n_v = 1$, $n_S = 1$, $n_l = 1$ and $n_w = 1$. Decreasing the prior scalars to one applies equal weight between the prior information and current

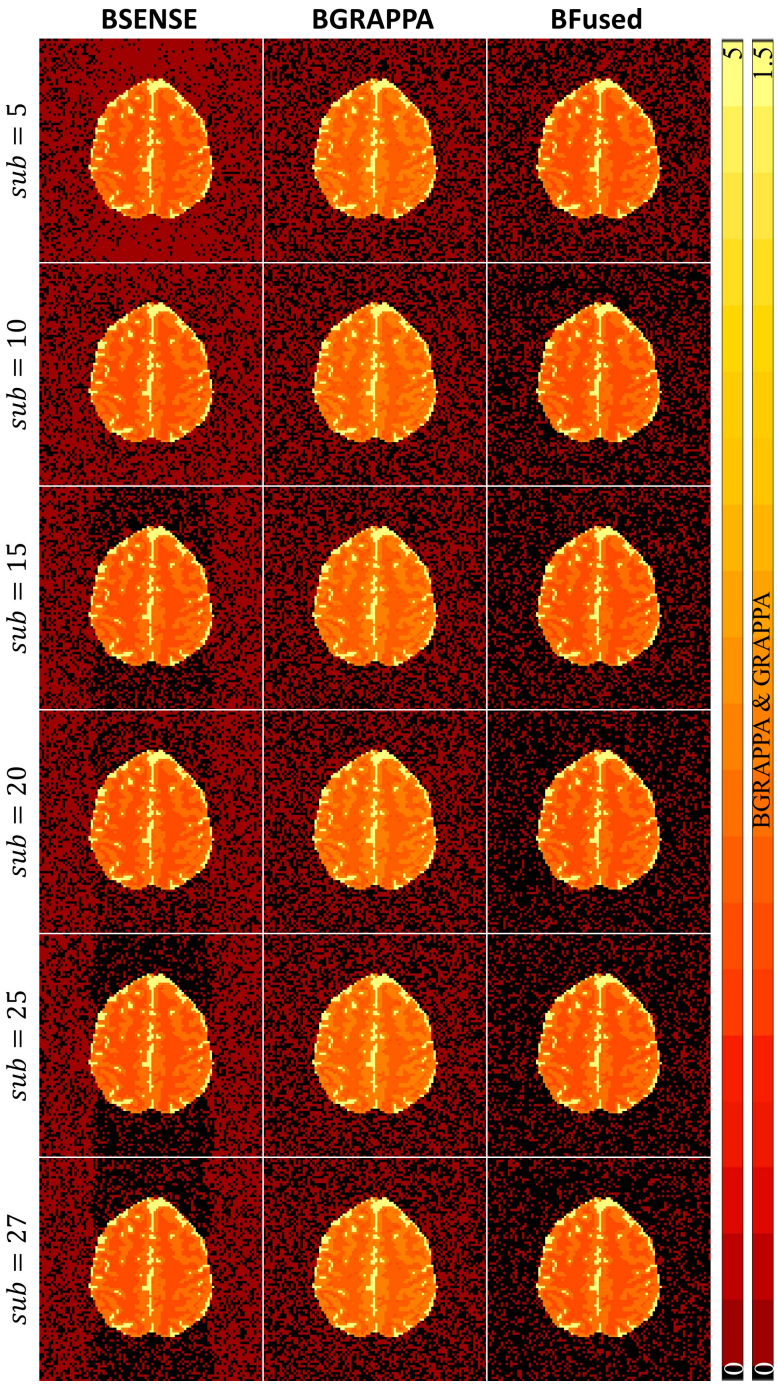

Figure 5.15: Reconstructed magnitude images for different samples of calibration time points from hyperparameter assessment for the Bayesian image reconstruction techniques. The left color bar shows the scale for the true magnitude, BSENSE and BFused techniques while the right color bar shows the scale for BGRAPPA.

information from the aliased time series in the reconstructed image. The plot in Figure 5.14b shows the average correlation between all voxels and the voxels they were previously aliased with for sampling sizes of 5, 10, 15, 20, 25, and 27, out of 30 calibration time points, comparing them to the non-sampling methods that has been demonstrated throughout the dissertation. The results indicate that sampling the calibration time points remarkably decrease the correlation for BSENSE and BFused. For BGRAPPA, the correlation does slightly decrease but increases as the sampling size increases ultimately being close to the correlation without sampling.

With the correlation analysis of sampling the calibration time points, Figure 5.15 shows the magnitude of the reconstructed images for each Bayesian reconstruction technique. The results displayed in this figure show that sampling the calibration time points has little effect on the magnitude reconstructed images inside the brain. It appears that BSENSE does have a small aliasing effect from this sampling method with BGRAPPA and BFused no experiencing this same effect. From Figure 5.15, as the sampling size increases, noise level for BSENSE and BFused slightly decrease while BGRAPPA remains unchanged.

Along with analysis of the number of calibration time points, we evaluate how applying different acceleration factors, n_A, to the subsampled coil k-space arrays affect the results for each reconstruction technique. Here, we fixed the number of calibration time points to be $n_{cal} = 30$ for hyperparameter assessment and set the acceleration factors of the non-task time series to be $n_A = 2, 3, 4, 6, 8, 12$. For SENSE, the acceleration factor cannot be larger than the number of coils in the sensitivity map as it will cause the system of linear equations to be underdetermined, which makes estimation difficult. So, in the acceleration factor analysis, the SENSE technique is not used to reconstruct using an acceleration factor of $n_A = 12$. Only the results for $n_A = 2, 3, 4$ are shown for some of the figures simply to see how increasing the acceleration factor affects the reconstruction results. These subsampled coil k-space arrays

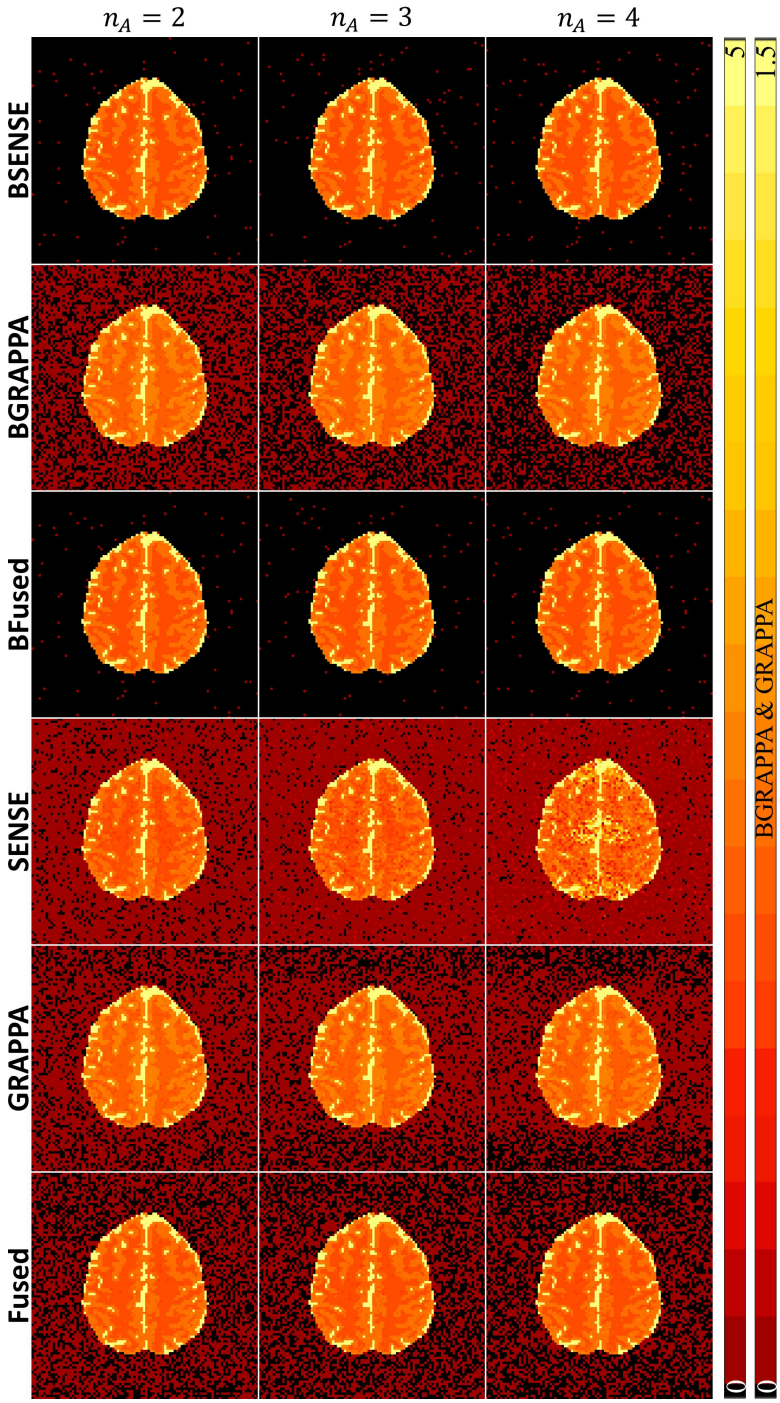

Figure 5.16: Reconstructed magnitude images for different acceleration factors using the traditional and Bayesian image reconstruction techniques. The left color bar shows the scale for the true magnitude, BSENSE, BFused, SENSE, and Fused techniques while the right color bar shows the scale for the reference magnitude, BGRAPPA, and GRAPPA techniques.

with separate acceleration factors were reconstructed into full images using the Bayesian and traditional techniques, comparing the results for all methods.

The results, exhibited in Figure 5.16, show that the magnitude images from each of the reconstruction techniques are negligibly affected by increasing the acceleration factor except for SENSE. For BGRAPPA, the noise level outside the brain does decrease as the acceleration factor increases while it only slightly decreases for GRAPPA. Again, the magnitude reconstructed images from the traditional techniques have slightly more noise than the magnitude reconstructed images from the Bayesian techniques. This is evident for examining the noise level both inside and outside the brain.

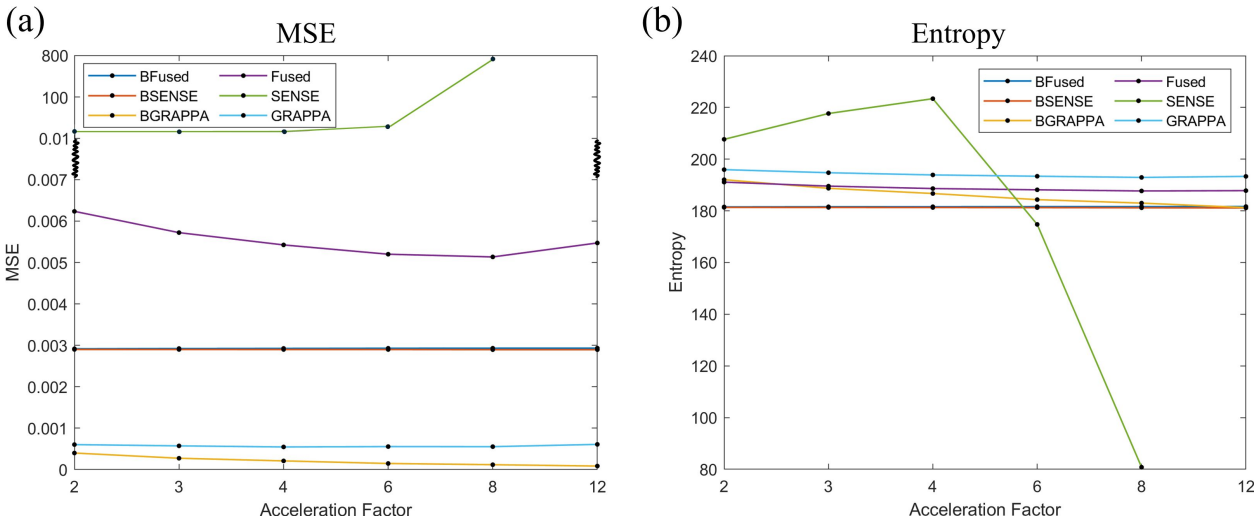

Figure 5.17: (a) MSE for inside the brain for each reconstruction technique compared to the true simulated or reference magnitude image for different acceleration factors. (b) Entropy plot for each reconstruction technique applying different acceleration factors. For both plots, BSENSE is the orange line, BGRAPPA is the yellow line, BFused is the blue line, SENSE is the green line, GRAPPA is the light blue line, and Fused is the purple line.

Figure 5.17 shows the MSE and entropy for different acceleration factors from the magnitude images for each reconstruction technique. Shown in Figure 5.17a, the MSE for BSENSE and BFused are very similar and much smaller than the SENSE and Fused techniques as they are compared to the true simulated magnitude image. The line for SENSE in the MSE

plot is above 0.01 at all acceleration factors with the MSE getting close to 800 at $n_A = 8$. Both BGRAPPA and GRAPPA have smaller MSE values than the rest of the reconstruction techniques, with BGRAPPA being the smallest, but are compared to the reference magnitude image. The MSE plot also shows that the MSE slightly decreases for the GRAPPA and Fused techniques while the Bayesian techniques seem unaffected by the acceleration factor. For the entropy plot in Figure 5.17b, SENSE appears to have inconsistencies with the entropy values due to the inaccuracy of the magnitude reconstructed images for each acceleration factor. The entropy values for the other techniques seems relatively steady (except a slight decrease with BGRAPPA) as the acceleration factor increases with the Bayesian methods having lower values. Having lower MSE and entropy values for the Bayesian reconstruction techniques show higher accuracy in reconstructing the subsampled data.

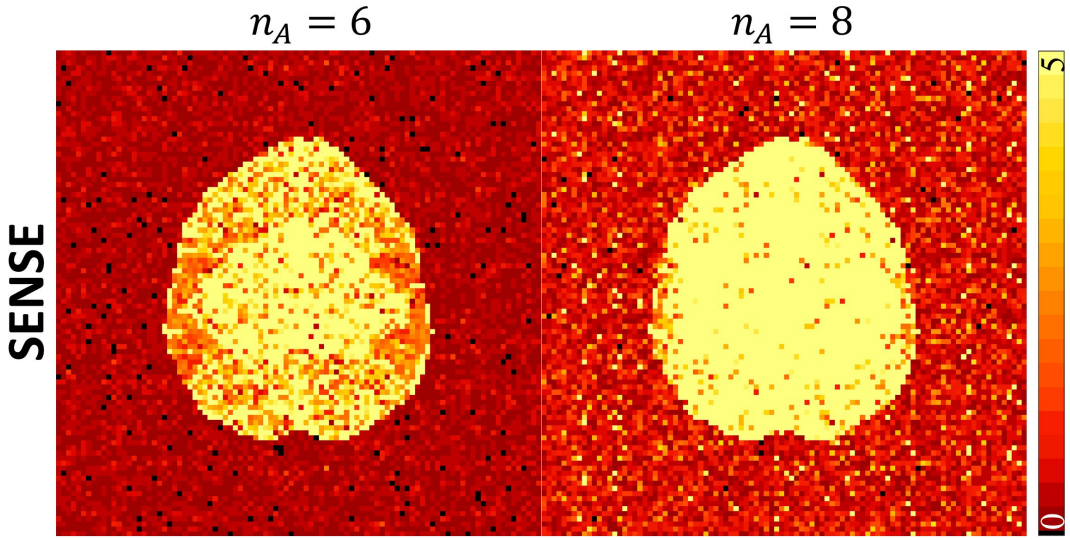

Figure 5.18: SENSE magnitude reconstructed images with $n_A = 6$ (left) and $n_A = 8$ (right).

Figure 5.18 displays the magnitude of the reconstructed images using SENSE for acceleration factors $n_A = 6$ (left) and $n_A = 8$ (right). From this figure, we can see why the MSE plot (Figure 5.17a) is substantially higher for SENSE as there any too many aliasing artifacts yielding no anatomically structure. This also explains why the SENSE line (green) in the entropy plot (Figure 5.17b) is inconsistent as the acceleration factor increases to $n_A = 6$ and

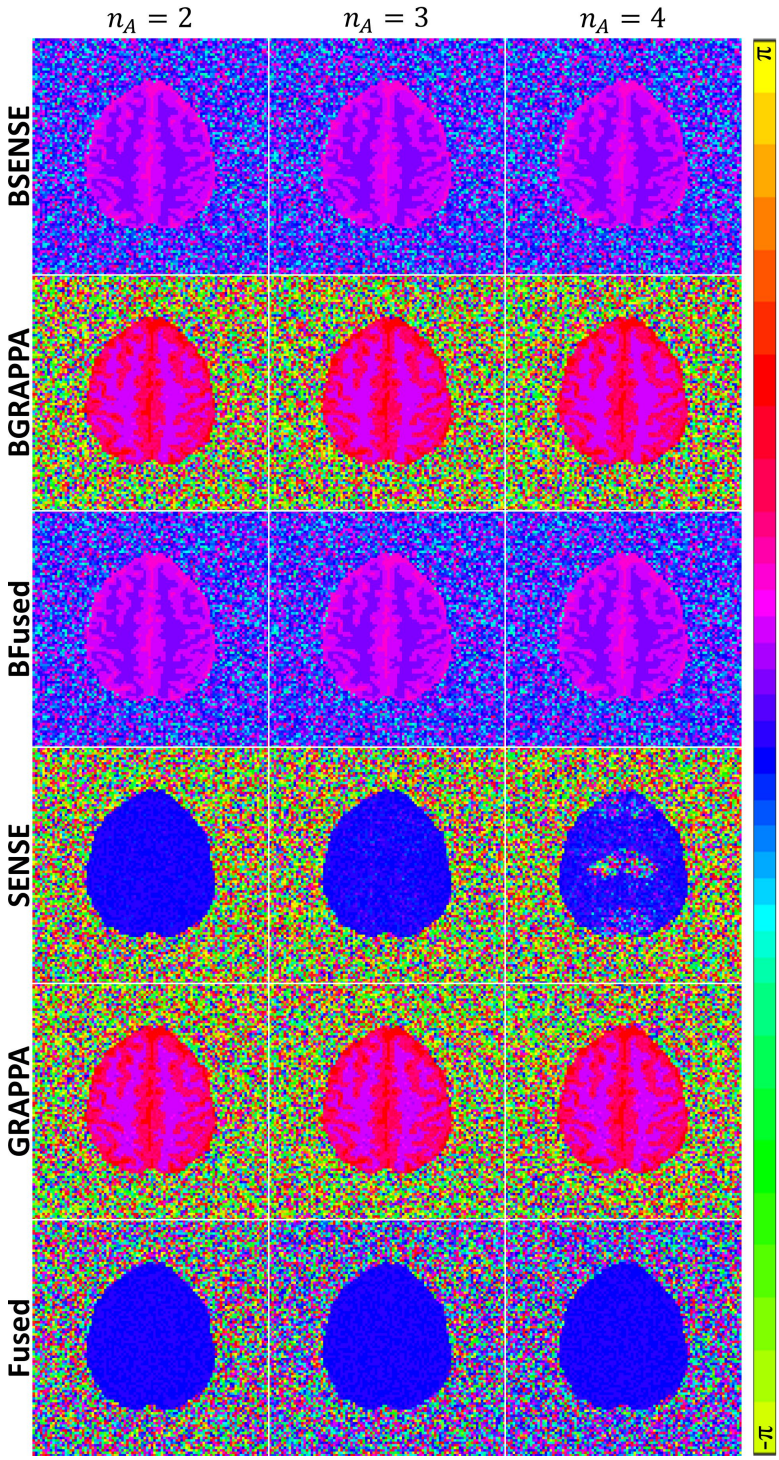

Figure 5.19: Reconstructed phase images for different acceleration factors using the traditional and Bayesian image reconstruction techniques. Due to the circular nature of phase angles, the color bar for the phase images have wrap-around.

$n_A = 8$.

The reconstructed phase images for different acceleration factors for each reconstruction techniques is shown in Figure 5.19. Like the magnitude images displayed in Figure 5.16, increasing the acceleration appears to only have an effect on the phase of the SENSE reconstructed images. Similar to the results shown in Figures 5.5 and 5.11, BSENSE and BFused phase reconstructed images closely resemble the true simulated phase image (shown in Figure 5.5) and the BGRAPPA and GRAPPA phase images appear to be similar to the reference phase image (also shown in Figure 5.5) while the SENSE and Fused techniques produce phase images with no information inside the brain.

Figure 5.20 displays the temporal variance for each reconstruction technique using different acceleration factors. In Figure 5.20, there are the same two scales for the color bars as shown in Figure 5.12 where one is for the BSENSE and BFused techniques which go to 0.0001 and the other is for the other techniques that go to 0.0125. The results illustrated in this figure show that BSENSE and BFused have notably smaller temporal variance compared to the other reconstruction techniques with BFused having the smaller temporal variance. Also, BGRAPPA appears to have a slightly smaller temporal variance compared to the traditional techniques. This further emphasizes that the Bayesian reconstruction techniques reduce the noise through time compared to the traditional techniques. From Figure 5.20, we can see that increasing the acceleration factor decreases the temporal variance for the BGRAPPA, BFused, and GRAPPA while slightly increasing for BSENSE. Figure 5.20 also shows that the Fused technique slightly increases inside the brain and slightly decreases outside. For SENSE, the temporal variance both inside and outside the brain considerably increases as the acceleration factor increases.

To further analyze the usage of different acceleration factors, Figure 5.21 displays the

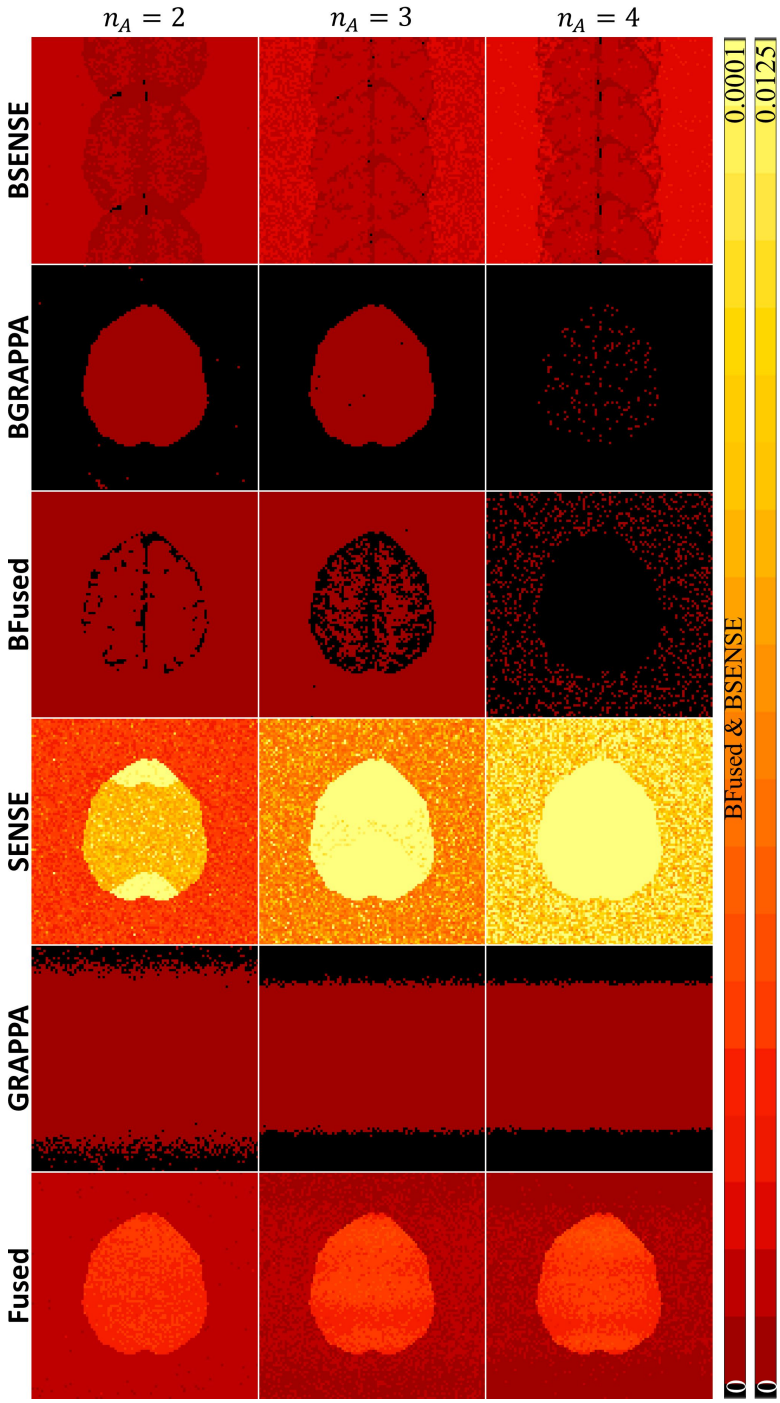

Figure 5.20: Temporal variance for different acceleration factors using the traditional and Bayesian image reconstruction techniques. The left color bar shows the scale for the BSENSE and BFused techniques while the right color bar shows the scale for the other techniques.

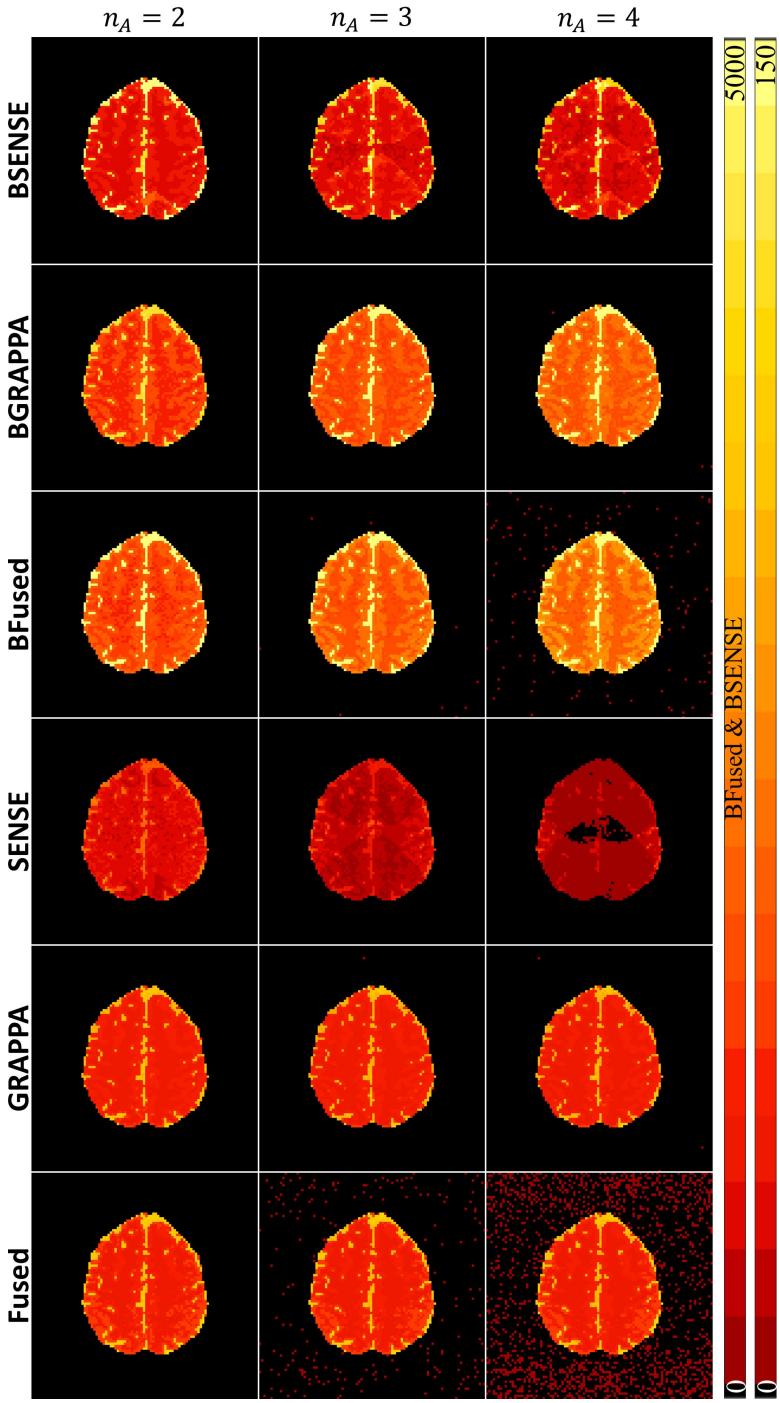

Figure 5.21: SNR for different acceleration factors using the traditional and Bayesian image reconstruction techniques. The left color bar shows the scale for the BSENSE and BFused techniques while the right color bar shows the scale for the other techniques.

SNR images for each reconstruction technique. In Figure 5.21, the one scale for the color bars is for the BSENSE and BFused techniques that go to 5000 while the other color bar goes to 150 for the other techniques. This indicates a sizable increase in SNR with these two Bayesian techniques, again, showing an inverse relationship with the temporal variance. We can see that BFused has noticeably higher SNR values compared to BSENSE. Of the reconstruction techniques on the other scale, BGRAPPA appears to have the highest SNR values. As the acceleration factor increases, the SNR values increase for the BGRAPPA and BFused techniques, decrease for BSENSE and SENSE, and are seemingly unchanged for the GRAPPA and Fused techniques. Based on these results, the techniques that involve estimating spatial frequencies either increase the SNR values or leave them unchanged, which can be an advantage for using these reconstruction techniques.

5.1.3 Task Activation

In task-based fMRI, the non-task reconstructed images create a baseline value for each voxel. This yield an intercept-only simple linear regression model $y = \beta_0 + \xi$ where y is the magnitude of the reconstructed voxel value. By adding in task activation to select images in the series of images, we have a simple linear regression model $y = \beta_0 + \beta_1 x + \xi$ for the unaliased voxel values. In this regression, β_0 is the baseline voxel value for the non-task reconstructed images determining the SNR, as demonstrated in the previous subsection. The β_1 value is the estimated task related signal increase from β_0 determining the contrast-to-noise ratio $CNR = \beta_1/\sigma$. The vector $x \in \{0,\ 1\}^{n_{IMG}}$, where n_{IMG} is the number of reconstructed images in the series, is a vector such that the zeros correspond to the images in the series without task activation and the ones correspond to the images with task activation. We can write this regression as $y = XB + \epsilon$, where $X = [1,\ x] \in \mathbb{R}^{n_{IMG} \times 2}$ and $B = [\beta_0,\ \beta_1]'$.

The task is not usually visible on the reconstructed images since the CNR is typically

much lower than the SNR. Instead, a right-tailed t-test is carried out with $\beta_1 \leq 0$ as the null hypothesis and $\beta_1 > 0$ as the alternative. The reason for the one-sided hypothesis test is because we only anticipate an increased signal from the task activation. To simulate added task, a $\beta_1 = 0.045$ magnitude-only signal increase is added to select voxels of the true noiseless non-task image. This added task activation is located in the left motor cortex to resemble the region of interest (ROI) of brain activity from the fMRI unilateral right-hand finger tapping experiment used in Section 5.2 (Karaman et al., 2014).

Similar to magnitude-only task activation, we can also use phase images for task detection. A simulated phase task of $\pi/120$ was also added to the true simulated task image. A simple linear regression model, $\phi = \theta_0 + \theta_1 x + \epsilon$, can be used for the phase activation as well. In this regression, ϕ is the phase of the reconstructed voxel, θ_0 is the baseline phase voxel value from the non-task reconstructed images, and θ_1 is the estimated increase from θ_0. We then use a one-tailed t-test, $t = \hat{\theta}_1 / SE(\hat{\theta}_1)$t, to determine which voxels contain statistically significant θ_1 values indicating which voxels experience phase task activation (Rowe et al., 2007).

5.1.4 FMRI Time Series Data Generation

A noiseless task image was used along with the noiseless non-task image to create a series of $n_{TR} = 510$ simulated full coil images for one slice mimicking real-world fMRI data. The simulated task activation was designed to mimic tapping of the subject's right fingers leading to activity in the left motor cortex which becomes our ROI for analyzing task detection in this experiment, as mentioned above. Knowing this, artificial signal increase was added to the voxels in the ROI (as mentioned in Section 5.1.3) for task images.

The true images were multiplied by the same $n_C = 8$ coil sensitivity maps for the non-task simulated time series (as illustrated in Figure 5.1), and then the series of images

were Fourier transformed in full coil k-space arrays. This series was also generated by adding separate $N(0, 0.0036 n_y n_x)$ noise to the real and imaginary parts of the full coil k-space arrays and were then inverse Fourier transformed back into cull coil images, yielding a CNR of 0.75. To simulate our real-world fMRI experimental process, the first 20 time points in the series were non-task. The scaling for the first few images in the fMRI simulated data is similar to that outlined in Section 5.1.1 for each of the tissue types. The initial 20 non-task time points are followed by 16 epochs alternating between 15 non-task and 15 task time points. An epoch is a stimulation period with time points of the subject at rest (non-task) and the subject performing an action or task. The series culminated with 10 non-task time points producing the simulated fMRI series $n_{TR} = 510$ images. To mimic the fMRI experiment in Section 5.2, the first 20 time points were omitted leaving 490 time points in the series. This series is transformed into the spatial frequency domain and then subsampled according to the acceleration factor to simulate subsampling of a real fMRI experiment. For the BSENSE and SENSE techniques, these subsampled coil k-space arrays were inverse Fourier transformed into alias coil images for reconstruction. The last n_{cal} full coil FOV time points in the second non-task time series from Subsection 5.1.1 were utilized as full FOV coil calibration k-space arrays and full FOV calibration images to assess the hyperparameters for all techniques.

5.1.5 FMRI Time Series Reconstruction Results

The hypothesis test described in Section 5.1.3 was utilized to determine voxels with a statistically significant signal increase. The statistically significant magnitude voxels for the simulated fMRI series of 490 time points, outlined in Section 5.1.4, for each reconstruction technique is displayed in Figure 5.22. For this magnitude-only task analysis, an acceleration factor of $n_A = 3$ was applied for subsampling the k-space arrays with $n_{cal} = 30$ calibration time points were utilized for hyperparameter determination. A 5% false discovery rate (FDR) threshold procedure (Benjamini and Hochberg, 1995; Genovese et al., 2002;

Logan and Rowe, 2004) was used for multiplicity correction. The ROI here consists of 28 voxels located in the left motor cortex and is outlined in green for each image in Figure 5.22. The results in Figure 5.22 show that, visually, the Bayesian reconstruction techniques capture the expected task activation in the ROI. SENSE also detects task activation, but GRAPPA and the Fused technique does not capture the task active voxels.

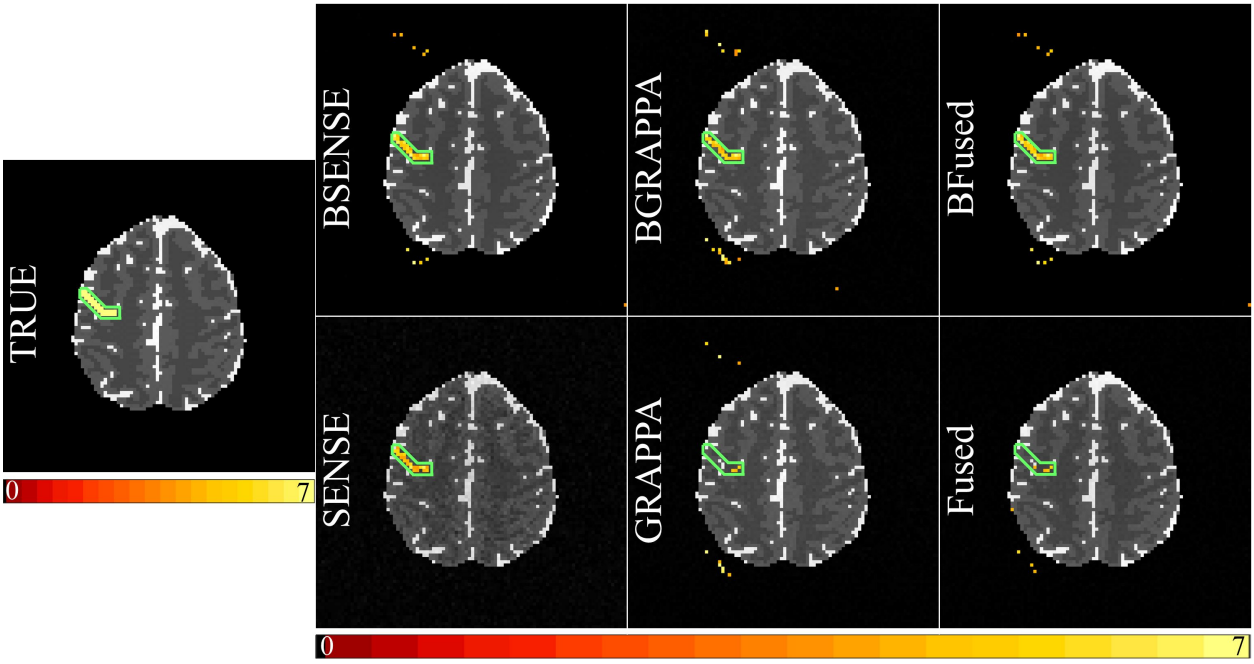

Figure 5.22: Magnitude image with active task voxels in the ROI (first column), statistically significant voxels in the ROI using FDR for the Bayesian reconstructed magnitude images (first row, columns 2-4), and significant voxels in the ROI using FDR for the reconstructed magnitude images using traditional techniques (second row, columns 2-4).

Since a one-tailed t-test is used for hypothesis testing, we can inspect the t-statistics closer. Figure 5.23a displays a bar graph of the number of correctly identified task voxels, out of 28, for each reconstruction technique from the magnitude-only task detection in Figure 5.22. This graph shows that the Bayesian techniques all identified more task voxels in the ROI compared to the traditional techniques with BSENSE and BFused capturing two more than BGRAPPA. Figure 5.23b shows a bar graph of the mean t-statistic values in the ROI (whether or not the voxels are considered active) for each reconstruction technique. The

result shows that the Bayesian techniques have high mean t-statistic values compared to the traditional techniques. BSENSE and BFused have virtually the same mean t-statistic value while BGRAPPA is slightly smaller. The GRAPPA and Fused techniques appear to have the worst results with capturing task activation as SENSE proves to be the best of the three for task detection despite having the worst non-task reconstruction results, expressed in Section 5.1.2.

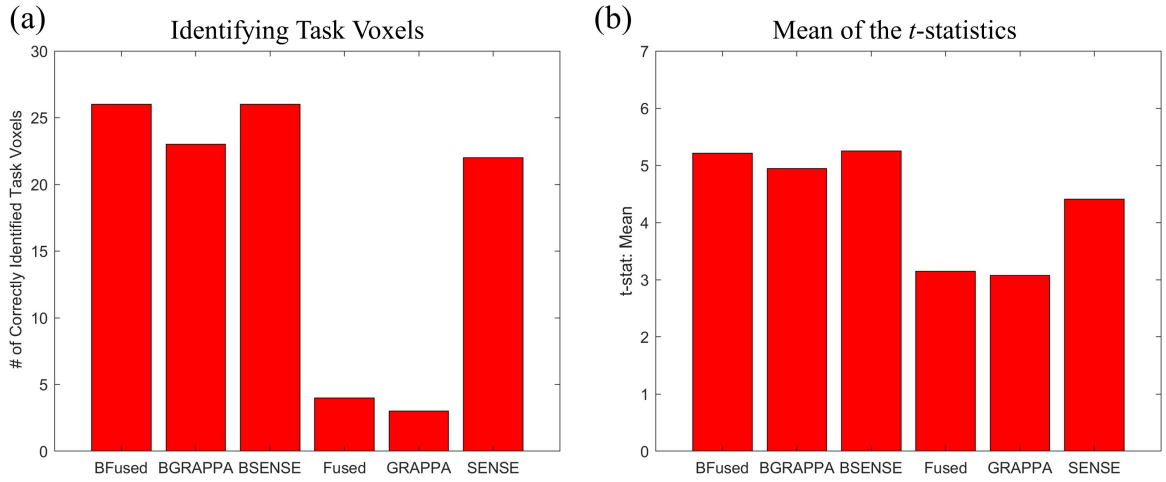

Figure 5.23: (a) Bar graph for number of correctly identified magnitude-only task voxels and (b) a bar graph of mean values for the t-statistics for each reconstruction technique.

Similar to the magnitude-only task analysis, a phase-only task analysis can be performed on the reconstructed images. The hypothesis test for phase-only activation is described in Section 5.1.3, determining voxels with a statistically significant signal increase. Using a 5% false discovery rate (FDR) threshold procedure (Benjamini and Hochberg, 1995; Genovese et al., 2002; Logan and Rowe, 2004), the image results for the phase-only task activation analysis in Figure 5.24 with the ROI outlined in green. The results in Figure 5.24 appear similar to that of the magnitude-only task results shown in Figure 5.22. That is, the Bayesian reconstruction techniques and SENSE all capture the task activation in the ROI. For GRAPPA and Fused techniques, there are some statistically significant voxels in the ROI, but not enough that would allow us to consider activation in that region.

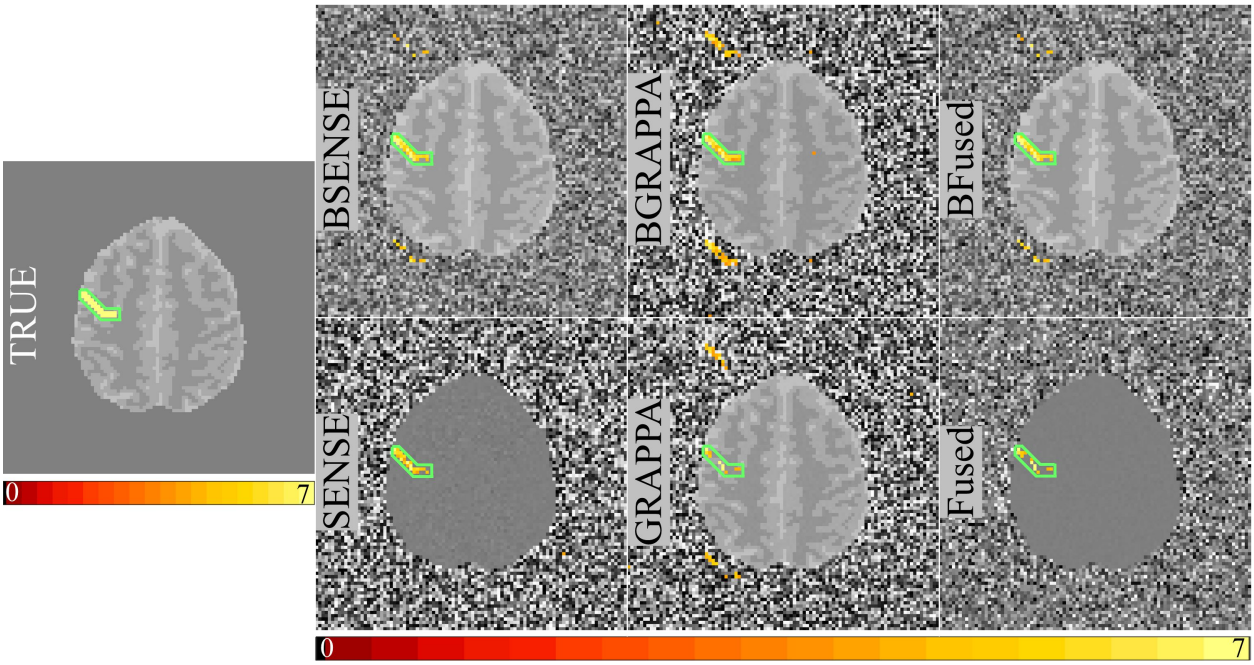

Figure 5.24: Phase image with active task voxels in the ROI (first column), statistically significant voxels in the ROI using FDR for the Bayesian reconstructed phase images (first row, columns 2-4), and significant voxels in the ROI using FDR for the reconstructed phase images using traditional techniques (second row, columns 2-4).

Similar to the magnitude-only task analysis, we can inspect the t-statistics closer. Figure 5.25a displays a bar graph of the number of correctly identified task voxels, out of 28,

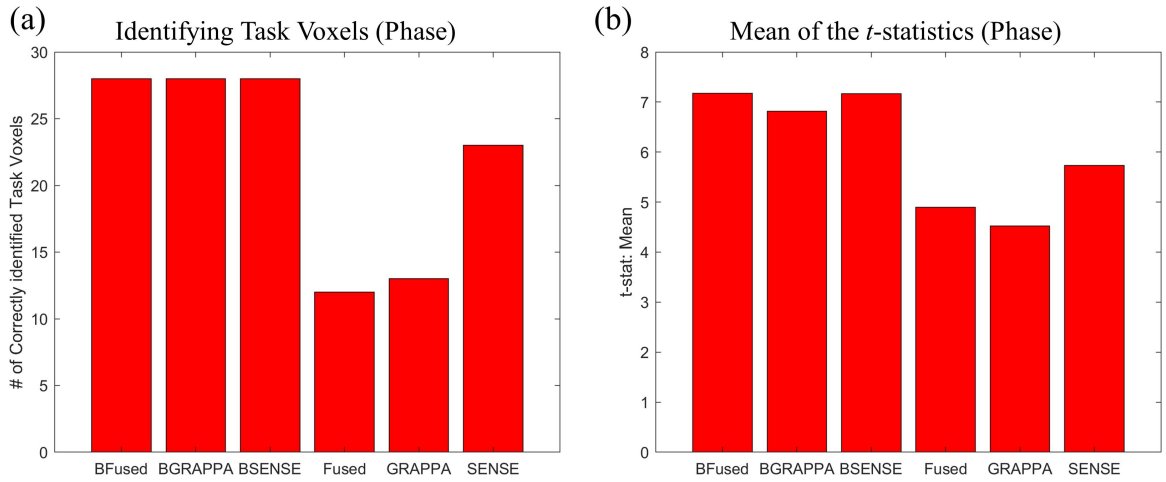

Figure 5.25: (a) Bar graph for number of correctly identified phase-only task voxels and (b) a bar graph of mean values for the t-statistics for each reconstruction technique.

and Figure 5.25b displays a bar graph of the mean t-statistic values in the ROI for each reconstruction technique from the phase-only task detection. Like the magnitude-only results in Figure 5.23, the Bayesian reconstruction techniques provide better task detection performance for the phase-only task analysis. In Figure 5.25a, the bar graph shows that BSENSE, BGRAPPA, and BFused detect all 28 task voxels in the ROI as active. SENSE also detects activity for the phase-only task detection, but GRAPPA and Fused do not even capture half of the task voxels in the ROI. Figure 5.25b shows that the Bayesian techniques have high mean t-statistic values compared to the traditional techniques with BGRAPPA being slightly smaller than BSENSE and BFused. Of the three traditional techniques, SENSE has the highest mean t-statistic value, but is still prominently smaller than the three Bayesian methods.

Similar to in the simulated non-task analysis, we evaluated how utilizing different number of calibration time points affects the task detection results. For this analysis, the acceleration factor was fixed at $n_A = 3$ with the number of calibration time points set to $n_{cal} = 5, 10, 15, 20, 25, 30$. Figure 5.26 displays the magnitude-only task detection results for different numbers of calibration time points using each reconstruction method. Similar to Figure 5.22, BSENSE, BGRAPPA, BFused, and SENSE capture the activation in the ROI outlined in green with the Bayesian techniques having stronger power in detecting the task. Visually, it appears that increasing the number of calibration time points have no effect on task detection. These results are further analyzed in Figure 5.27.

In Figure 5.27a shows a plot of the number of correctly identified task voxels in the ROI using different numbers of calibration images for each reconstruction technique. In this plot, the BFused blue line follows the BSENSE orange line. From this, we can see that BSENSE, BGRAPPA, and BFused all capture more task voxels than the traditional techniques with SENSE being the only one of the three capturing more than five voxels in the ROI. Figure

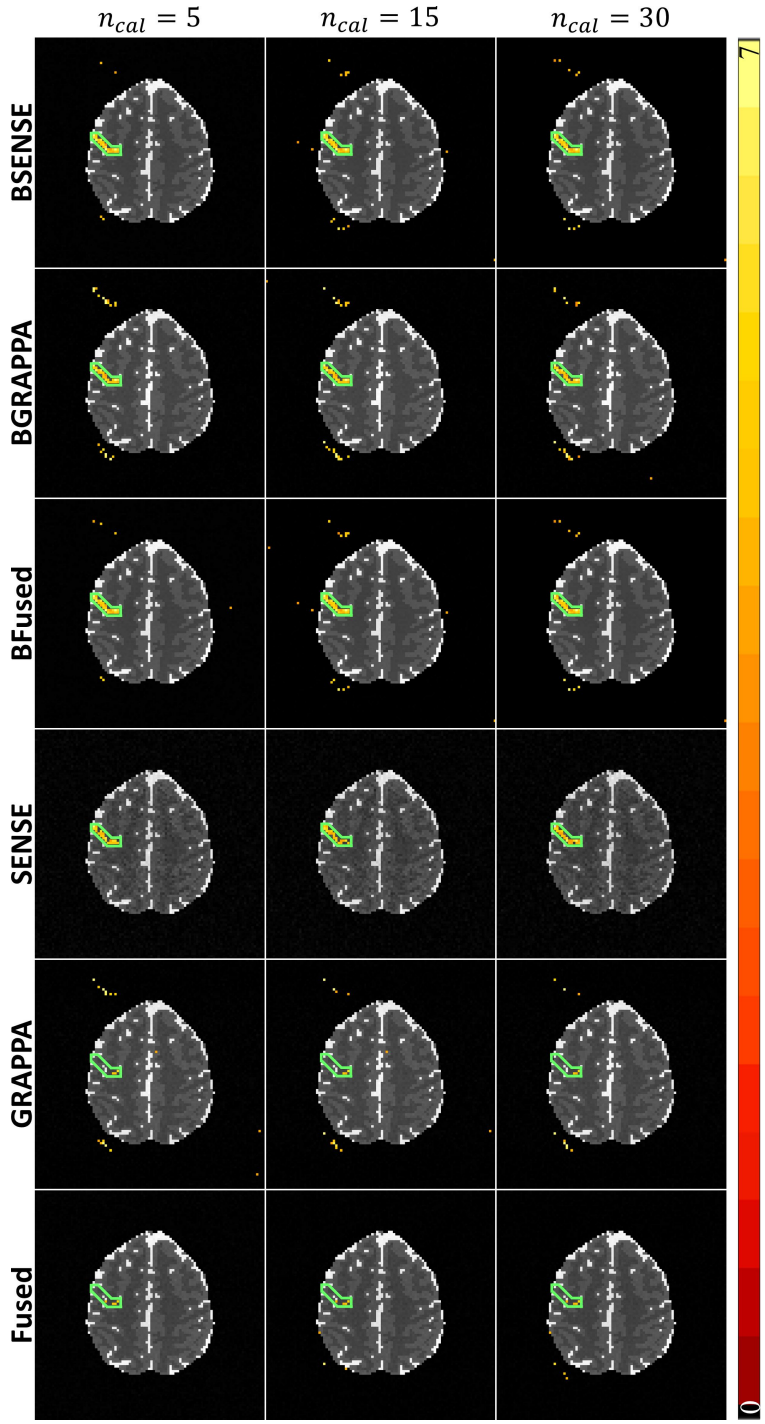

Figure 5.26: Statistically significant voxels in the ROI using FDR for the Bayesian reconstructed magnitude images (rows 1-3), and significant voxels in the ROI using FDR for the reconstructed magnitude images using traditional techniques (rows 4-6) for different numbers of calibration time points.

5.27b displays a plot of the mean t-statistic values for each number of calibration time points for all reconstruction techniques. This plot shows that the Bayesian techniques have higher mean t-values with BSENSE being slightly higher than BFused and BGRAPPA having the lowest of the three. Increasing the number of calibration time points used for hyperparameter assessment has little to no effect for each of the reconstruction techniques (except SENSE) as exhibited in both plots.

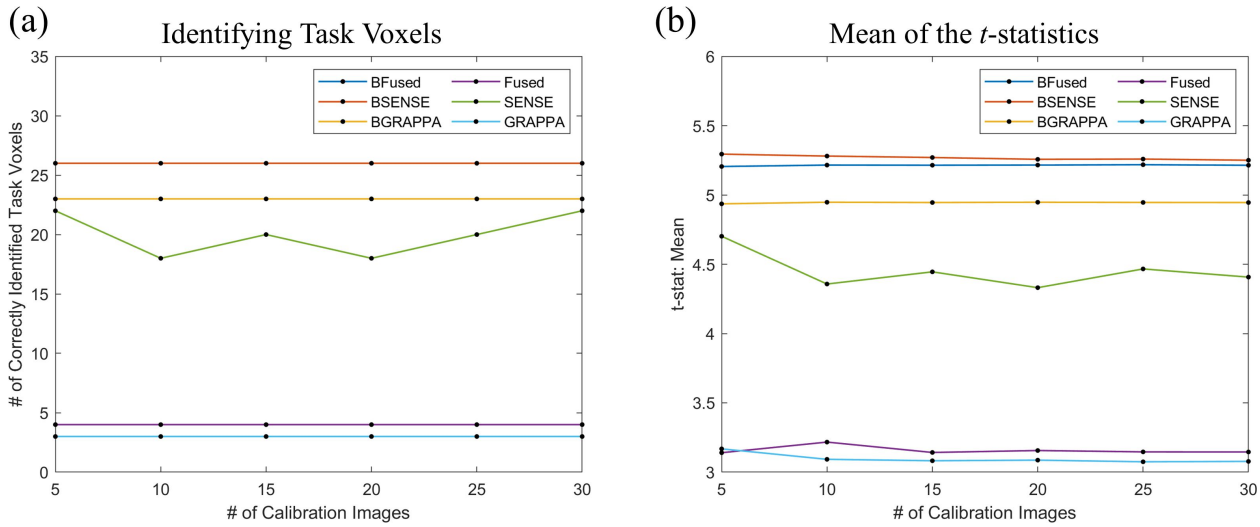

Figure 5.27: (a) Plot of correctly identified magnitude-only task voxels and (b) a plot of the mean values for the t-statistics for each reconstruction technique using a different number of calibration time points for hyperparmeter assessment.

Figure 5.28 shows the results for phase-only task activation for different numbers of calibration time points. Similar to the results shown in Figure 5.24, BSENSE, BGRAPPA, BFused, and SENSE all capture the activation in the ROI for each number of calibration time points. GRAPPA and Fused both detect voxels in the ROI but not a convincing amount to consider activation. Increasing the number of calibration time points for hyperparameter assessment also appears to have a visually insignificant effect on the power of task detection for all reconstruction techniques.

Additional phase-only task detection results are analyzed in Figure 5.29. Figure 5.29a

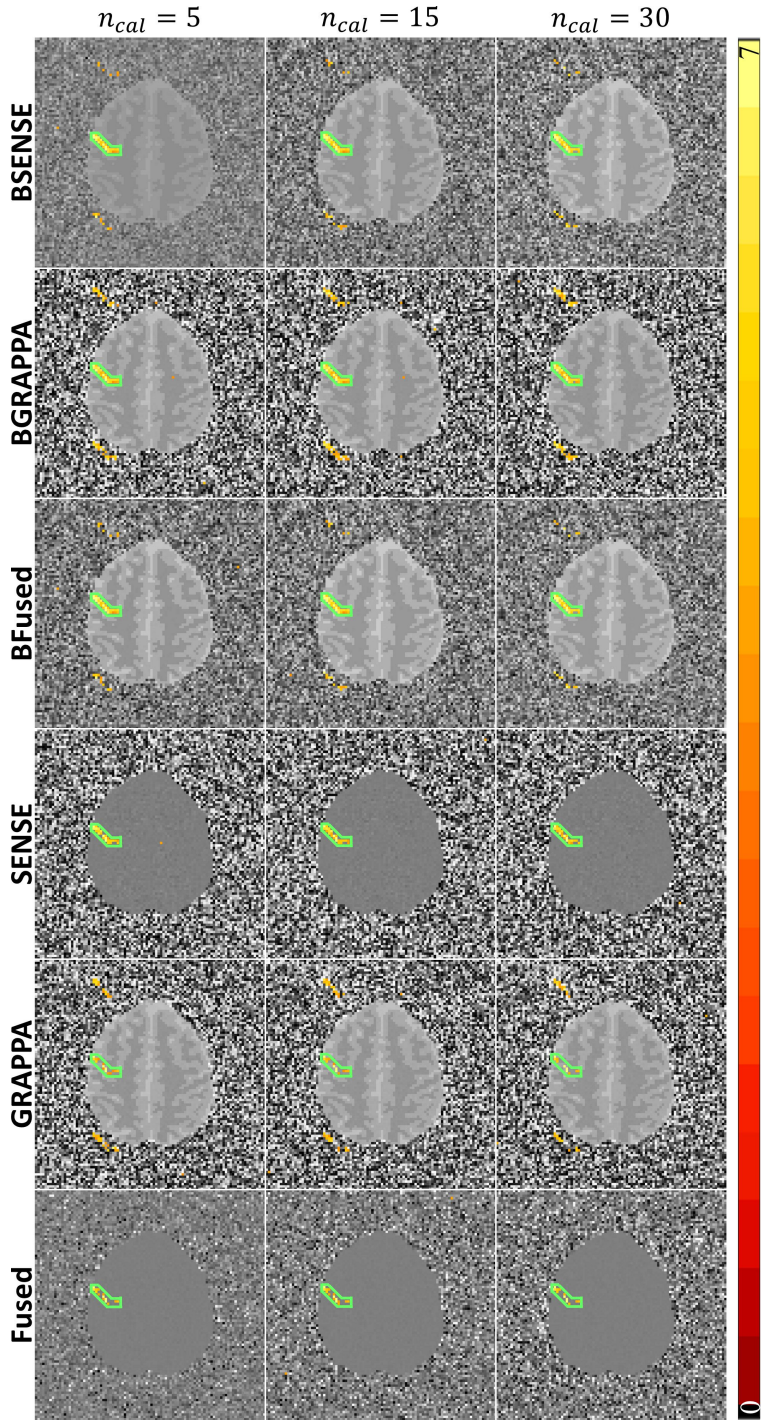

Figure 5.28: Statistically significant voxels in the ROI using FDR for the Bayesian reconstructed phase images (rows 1-3), and significant voxels in the ROI using FDR for the reconstructed phase images using traditional techniques (rows 4-6) for different numbers of calibration time points.

shows a plot of the number of correctly identified phase-only task voxels in the ROI using different numbers of calibration images for each reconstruction technique. In this plot, the BFused blue line and the BSENSE orange line follow the BGRAPPA yellow line where each of these captures all the task voxels in the ROI. Of the three traditional techniques, SENSE captured more active voxels in the ROI. Figure 5.29b displays a plot of the mean t-values for all reconstruction techniques using different numbers of calibration time points. This plot shows that the Bayesian techniques have higher mean t-statistic values with BFused and BSENSE being slightly higher than BGRAPPA. These plots show that increasing the number of calibration time points has no effect for the Bayesian techniques and very small effect on the reconstruction traditional techniques.

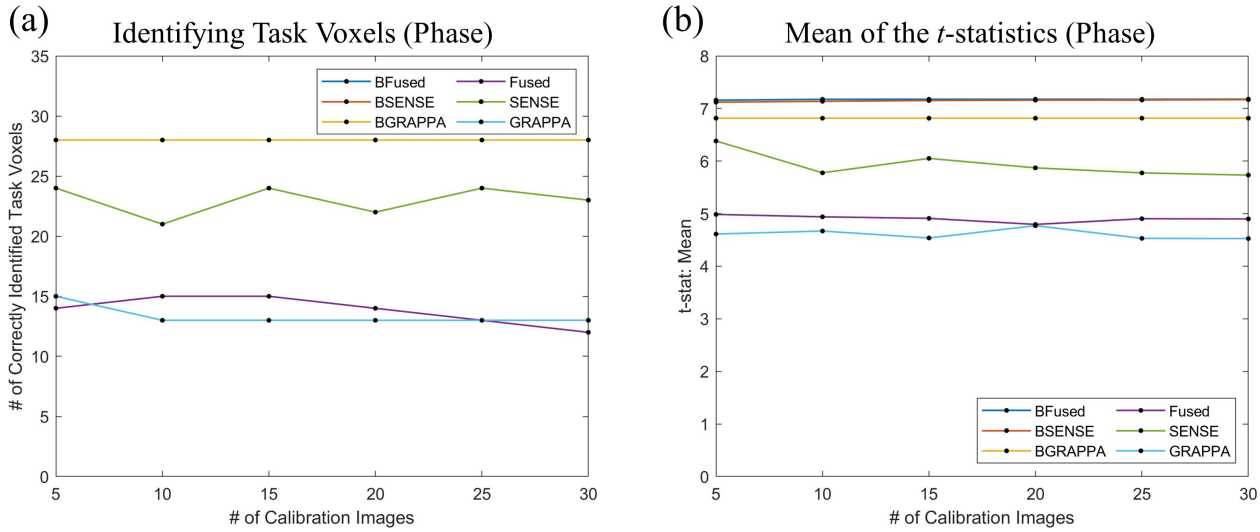

Figure 5.29: (a) Plot of correctly identified phase-only task voxels and (b) a plot of the mean values for the t-statistics for each reconstruction technique using a different number of calibration time points for hyperparameter assessment.

As mentioned in Section 5.1.2, using the same prior information at each time point in the series of subsampled fMRI data could potentially lead to task leakage. This can be seen in Figures 5.22, 5.26, 5.24, and 5.28 for each Bayesian technique having some task leakage above and below the brain in the task activation images. Since we know where leakage would be based on the acceleration factor, one could mask it out or flag it as suspicious. Here, the

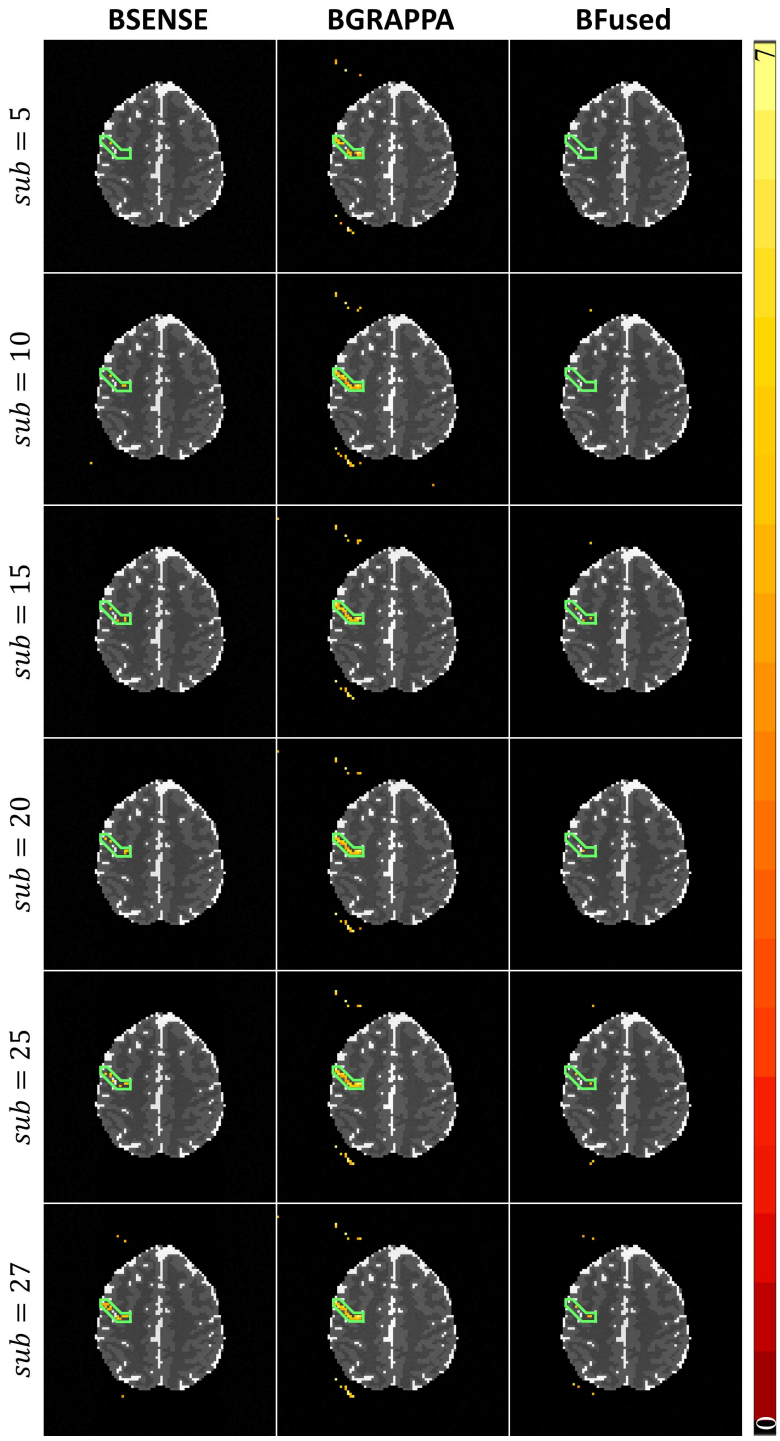

Figure 5.30: Statistically significant voxels in the ROI using FDR for the Bayesian reconstructed magnitude images utilizing different samples of calibration time points for hyperparameter assessment.

same sampling of the calibration time points process outlined in Section 5.1.2 was followed for task activation results. Figure 5.30 shows the magnitude-only task detection results for BSENSE (first column), BGRAPPA (second column), and BFused (third column). For BSENSE and BFused, sampling the calibration time points reduces the task leakage but also loses the task detection power while having minimal effect on BGRAPPA.

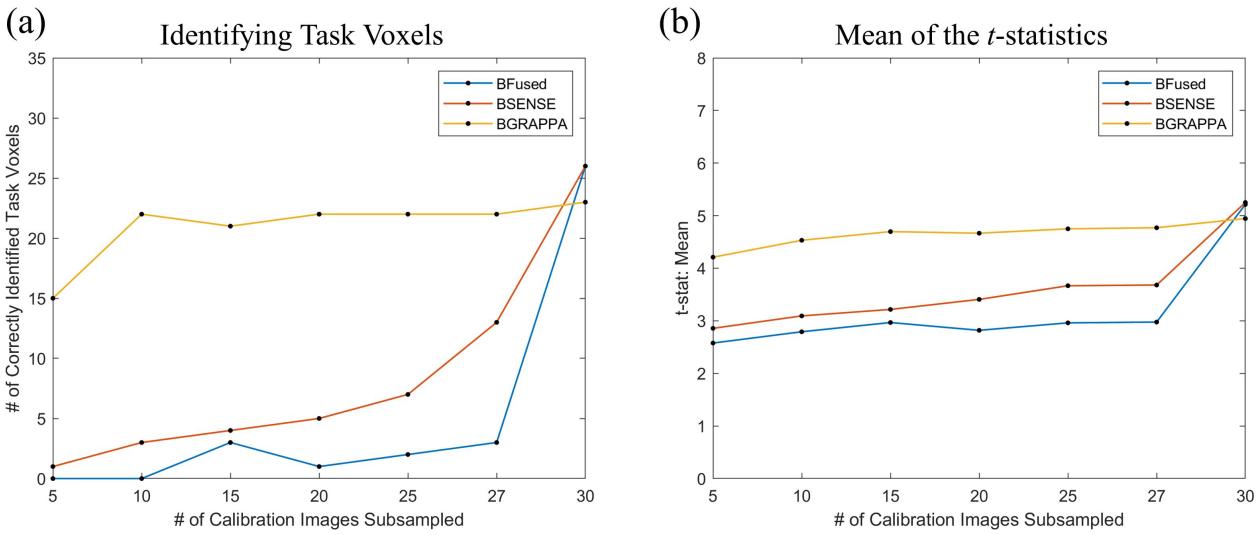

Figure 5.31: (a) Plot of correctly identified magnitude-only task voxels and (b) a plot of the mean values for the t-statistics for each Bayesian reconstruction technique using different samples of calibration time points for hyperparameter assessment.

Further analysis of magnitude-only task detection from calibration time point sampling is demonstrated in Figure 5.31. Figure 5.31a displays a plot of the number of voxels detected as task in the ROI of each sampling size for BSENSE, BGRAPPA, and BFused. Like the correlation analysis in Figure 5.14, BGRAPPA appears unaffected by sampling the calibration time points while the power of task detection for BSENSE and BFused is weakened. The plot in Figure 5.31b shows that the mean of the t-values for each sampling size noticeably decreases for BSENSE and BFused compared to the non-sampling process but is relatively unchanged for BGRAPPA. Both plots indicate a slight increase in task detection power as the sampling size increases.

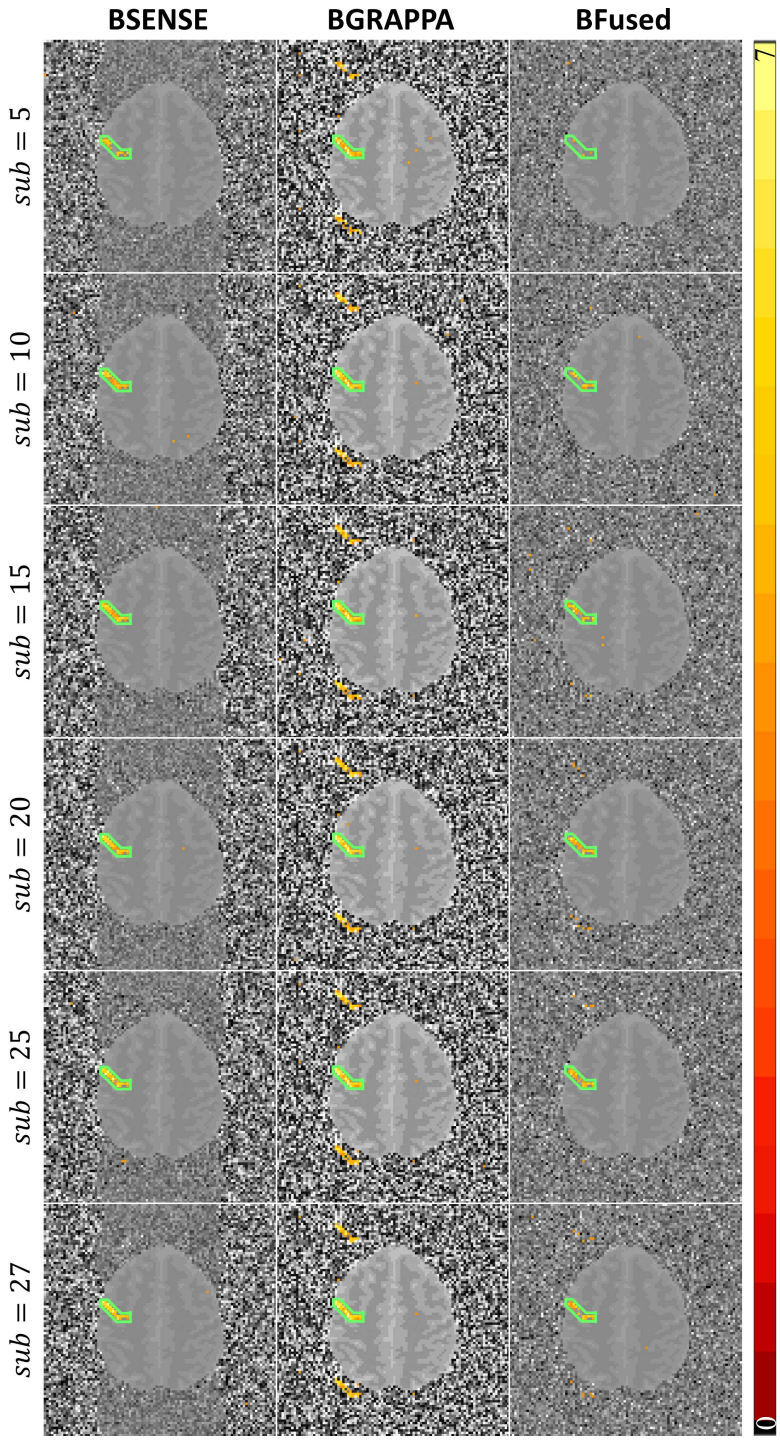

Figure 5.32: Statistically significant voxels in the ROI using FDR for the Bayesian reconstructed phase images utilizing different samples of calibration time points for hyperparameter assessment.

Along with the magnitude-only task analysis of this sampling process, Figure 5.32 shows the results for the phase-only task detection from sampling the calibration time points. Like the magnitude-only results, BGRAPPA appears minimally affected by the sampling of the calibration time points. For BFused, the task leakage and task-detection is slightly reduced, but still captures activation in the ROI for larger sampling sizes. However, BSENSE appears to remove the task leakage while still capturing task activation in the ROI.

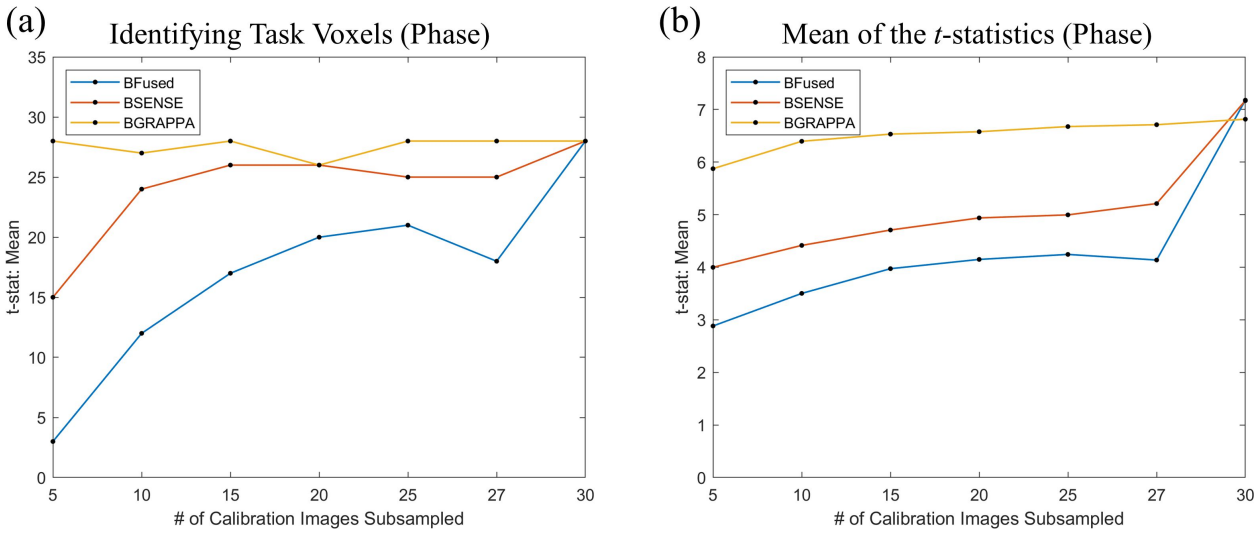

Figure 5.33: (a) Plot of correctly identified phase-only task voxels and (b) a plot of the mean values for the t-statistics for each Bayesian reconstruction technique using different samples of calibration time points for hyperparameter assessment.

Figure 5.33a displays a plot of the number of voxels detected as phase-only task in the ROI and Figure 5.33b shows a plot of the mean of the t-values for each sampling size for BSENSE, BGRAPPA, and BFused. BGRAPPA and BSENSE both capture phase-only task activation in the ROI, as shown in Figure 5.31b, but BGRAPPA did experience the task leakage. At higher sample sizes (greater than or equal to 15), BFused captures more than half of the active voxels in the ROI. In Figure 5.31b, BGRAPPA has the highest mean t-values for sampling the calibration time points with BFused having the lowest t-values. The number of voxels identified as task and the mean t-statistic values increase as the sampling size increase for all three Bayesian techniques.

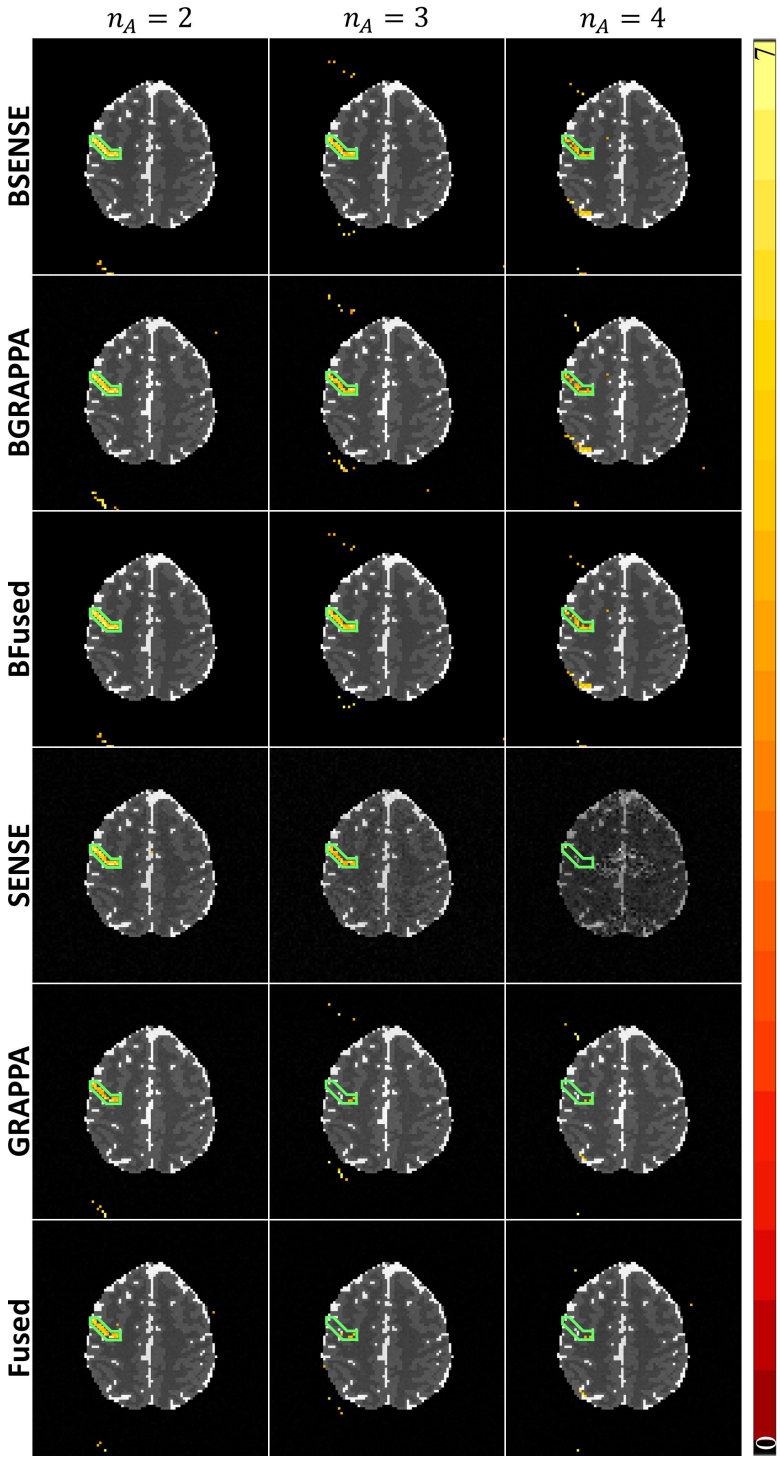

Figure 5.34: Statistically significant voxels in the ROI using FDR for the Bayesian reconstructed magnitude images (rows 1-3), and significant voxels in the ROI using FDR for the reconstructed magnitude images using traditional techniques (rows 4-6) for different acceleration factors.

Along with the various number of calibration time points, we evaluated how different acceleration factors affect task detection for each of the reconstruction techniques. For this, the number of calibration time points for hyperparameter assessment was fixed at $n_{cal} = 30$ and the different acceleration factors were set to be $n_A = 2, 3, 4, 6, 8, 12$. Again, since the acceleration factor for SENSE cannot be greater than the number of coils, SENSE was not used to reconstruct the subsampled data at $n_A = 12$. The results for the magnitude-only task activation is displayed in Figure 5.34. These results show that the Bayesian reconstruction methods capture the active voxels in the ROI up to $n_A = 4$. For SENSE, the magnitude-only task detection is effective up to $n_A = 3$, still less than the Bayesian techniques, but does not detect activation at $n_A = 4$. The GRAPPA and Fused techniques only detect task activation at an acceleration factor of $n_A = 2$.

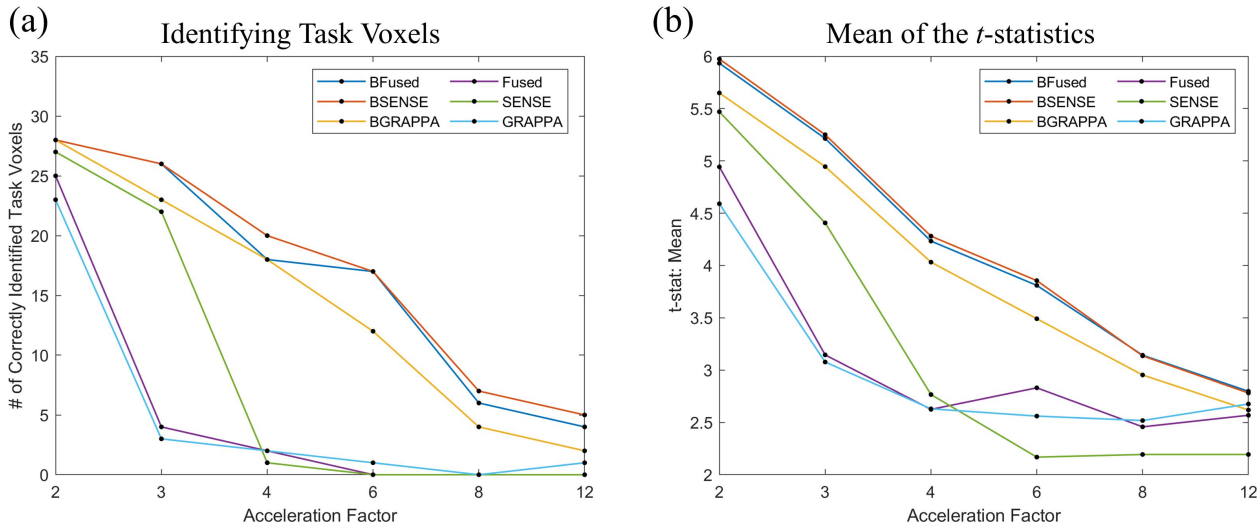

Figure 5.35: (a) Plot of correctly identified magnitude-only task voxels and (b) a plot of the mean values for the t-statistics for each reconstruction technique using different acceleration factors.

Figure 5.35 displays additional magnitude-only task analysis for different acceleration factors. In Figure 5.35a, we can see that for all reconstruction techniques, the number of correctly identified task voxels decrease as the acceleration factor increases. For all acceleration factors, the Bayesian techniques' correctly identified task voxels are notably higher

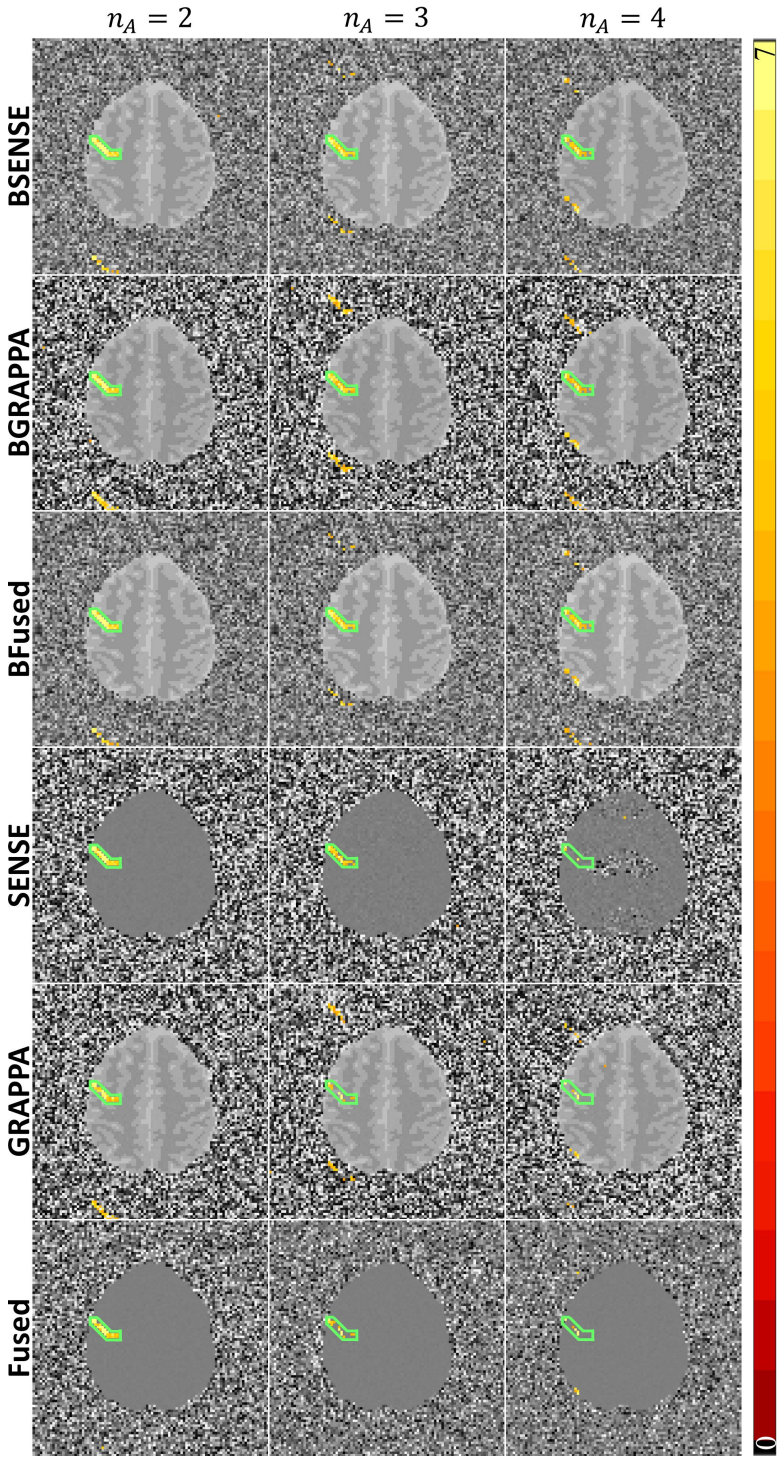

Figure 5.36: Statistically significant voxels in the ROI using FDR for the Bayesian reconstructed phase images (rows 1-3), and significant voxels in the ROI using FDR for the reconstructed phase images using traditional techniques (rows 4-6) for different acceleration factors.

than the traditional techniques. As the acceleration factor gets to $n_A = 6$, BSENSE and BFused still capture 18 of the 28 voxels in the ROI, but experiences noticeable task leakage. In Figure 5.35b, the Bayesian techniques have higher t-values than the traditional for each acceleration factor. Like Figure 5.35a, as the acceleration factor increases, the mean t-statistic values decrease for each technique. Evaluating both plots, BFused and BSENSE perform the best of all the techniques with both of them producing very similar results.

Task analysis of different acceleration factors is continued with investigating phase-only activation for each reconstruction method. Figure 5.36 displays the phase-only task detection images for acceleration factors up to $n_A = 4$ for each reconstruction technique. The results appear similar to that of the magnitude-only activation. The Bayesian techniques capture activation in the ROI for all three acceleration factors displayed, SENSE losing task detection power at $n_A = 4$, and GRAPPA and Fused have little task detection power after $n_A = 2$.

The task analysis for the phase-only task detection for different acceleration factors is shown in Figure 5.37. In Figure 5.35a, like the magnitude-only task detection, the number of correctly identified task voxels decrease as the acceleration factor increases for all reconstruction techniques. For all acceleration factors, the Bayesian techniques' identified task voxels are notably higher than the traditional techniques with BFused and BSENSE identifying the same number of task voxels as each other. As the acceleration factor gets to $n_A = 6$, BSENSE and BFused, again, still capture 18 of the 28 voxels in the ROI, but experiences notable task leakage. In Figure 5.37b, Like Figure 5.35b, as the acceleration factor increases, the mean t-statistic values decrease for each technique. The Bayesian techniques have higher t-values for the phase-only task dectection compared to traditional for each acceleration factor. BFused and BSENSE perform the best of all the techniques with both of them producing very similar results, as exhibited in both plots.

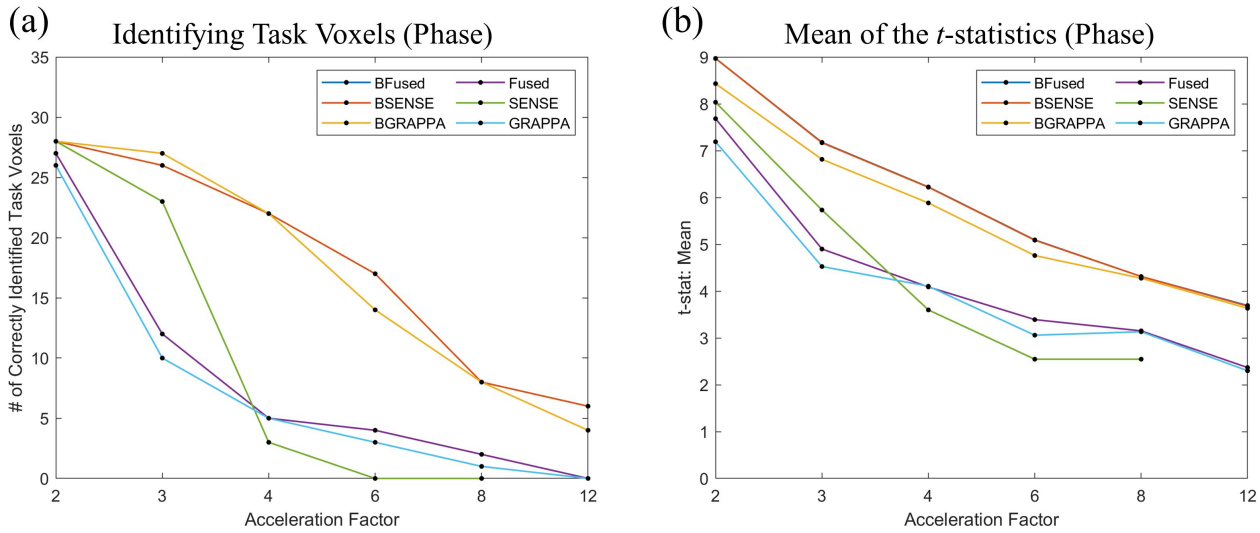

Figure 5.37: (a) Plot of correctly identified phase-only task voxels and (b) a plot of the mean values for the t-statistics for each reconstruction technique using different acceleration factors.

5.2 Experimental FMRI Study

5.2.1 Data Description

A 3.0 T General Electric Signa LX magnetic resonance imager was used to conduct an fMRI experiment on a single subject. A right-handed finger-tapping task was performed in a block design with an initial 20 s rest followed by 16 epochs with 15 s off (rest state) and 15 s on (task performed). The experiment was concluded with 10 s of rest giving us a series of $n_{TR} = 510$ repetitions with each repetition being 1 s, a flip angle of 90° and an acquisition bandwidth of 125 kHz. The data set consists of nine 2.5 mm thick axial slices with $n_C = 8$ receiver coils that have a 96×96 dimension for a 24 cm full FOV, with a posterior to anterior phase encoding direction. This procedure was repeated with the subject completely at resting state as well. This provides a non-task series of $n_{TR} = 510$ repetitions that can be utilized as pre-scan calibration information to assess the prior means and the hyperparameters.

For each volume image in the experimental series, a time dependent echo time, TE_t, consisted of three parts. The first part was fixed to have a value of $TE = 42.7$ ms at the first 10 time points. In the second part, the next five TE values were an equally spaced interval of values 42.7 ms, 45.5 ms, 47.7 ms, 50.2 ms, 52.7 ms and was repeated for another 5 time points. For the final part, the last 490 time points were fixed at 42.7 ms. To account for T_1 effects and varying echo times, the center row of k-space for each TR in each receiver coil was acquired with three navigator echoes which is used to correct any potential Nyquist "ghosting." The additional rows of k-space were incorporated to estimate and adjust the error in the center frequency and group delay offsets between the odd and even lines of k-space (Nencka et al., 2008).

Typically, the magnetic fields in an fMRI experiment will induce a drift in the phase over time which we correct before reconstruction to give us a stable phase through time. This phase correction was performed on both pre-scan non-task time series and the fMRI experiment time series. Once the phase was corrected, the last $n_{cal} = 30$ full k-space arrays and images (after IFT) of the non-task series of $n_{TR} = 510$ time points performed on the subject were used for hyperparameter assessment. The fMRI experimental series described above was used for fMRI analysis. The first 20 time points were discarded leaving 490 time points for the fMRI experiment due to the varying echo times and magnetization stability. The first 10 images not used for fMRI activation can be used to estimate a T_1 map (Karaman et al., 2014) while the second 10 images could be used for static magnetic field mapping (Hahn et al., 2012). Similar to the simulation study, the subsampled coil k-space arrays came from artificially skipping lines in the full coil k-space arrays of the fMRI experimental time series, mimicking the effect of actually subsampling the coil k-space arrays.

5.2.2 Experimental Reconstruction Results

Similar to the process for the simulated data described in Section 5.1, each image in the entire time series of aliased coil measurements were simultaneously unaliased and combined using the traditional and Bayesian reconstruction techniques. Before artificially aliasing the time series, a reference magnitude image (first row, first column in Figure 5.38) was produced by taking the square norm between the $n_C = 8$ full FOV coil images at the first time point. This provides a magnitude image with which to compare to BSENSE, BFused, SENSE, and Fused to. Another reference magnitude image (second row, first column in Figure 5.38) was produced by first Fourier transforming the $n_C = 8$ full coil images in full k-space arrays.

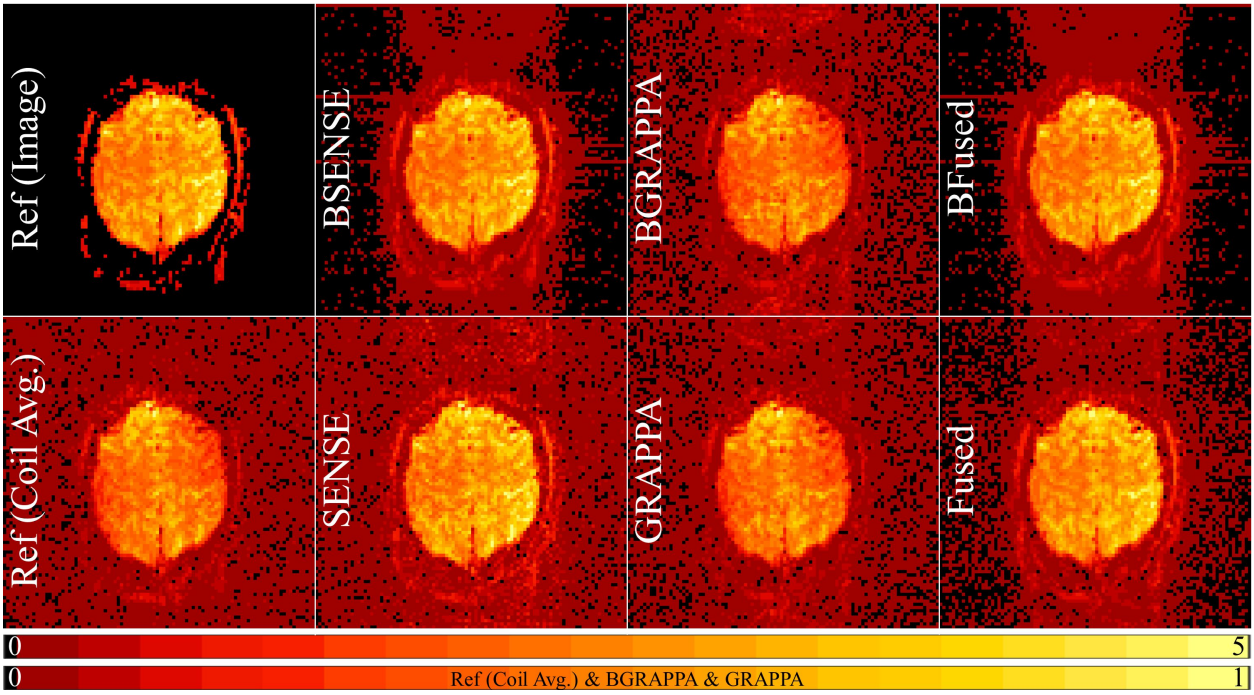

Figure 5.38: Reference non-task experimental magnitude image using the square norm of the coil images (first row, first column), reference non-task experimental magnitude reconstructed image from averaging the full coil k-space arrays (second row, first column), the Bayesian reconstructed experimental magnitude images (first row, columns 2-4) and experimental magnitude images from the traditional reconstruction techniques (second row, columns 2-4). The top color bar shows the scale for the square norm reference magnitude image, BSENSE, BFused, SENSE, and Fused techniques while the bottom color bar shows the scale for the averaged k-space arrays reference magnitude, BGRAPPA, and GRAPPA techniques.

Then the full coil k-space arrays were averaged together into a single, composite full k-space array and inverse Fourier transformed back into image space yielding the magnitude image in the second row, first column of Figure 5.38.

Figure 5.38 also displays the Bayesian reconstructed magnitude images (top row, columns 2-4) and the reconstructed magnitude images of the traditional reconstruction techniques (bottom row, columns 2-4) of the first time point from the 490 images using an acceleration factor of $n_A = 3$. Just as the simulated results in Figure 5.4 demonstrated, we can see that the joint MAP estimate from BSENSE and BFused produce magnitude images that closely resemble the square norm reference image in Figure 5.38 (first row, first column) inside the brain with the SENSE and Fused techniques reconstructing noisier magnitude images. The noise level outside the brain is also noticeably higher for the SENSE and Fused techniques compared to BSENSE and BFused. Visually the BGRAPPA magnitude image is slightly less noisy than the GRAPPA magnitude image when compared to the averaged k-space reference image (second row, first column).

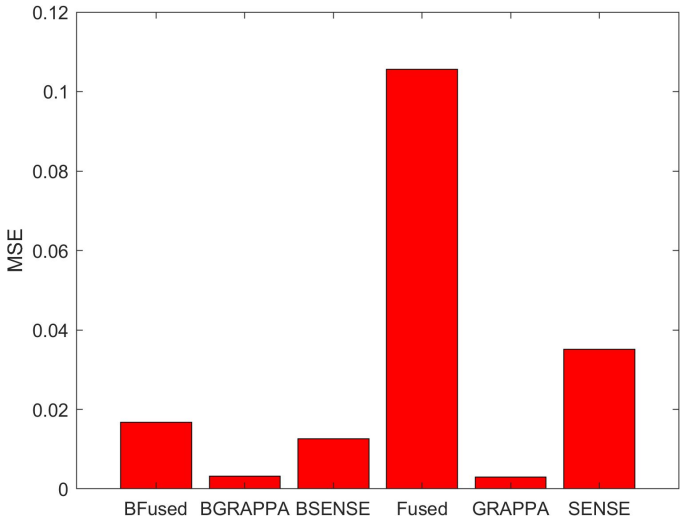

Figure 5.39: Bar graph of MSE estimates for inside the brain for the magnitude images of each of the reconstruction techniques for the experimental data.

To calculate the MSE estimates for the magnitude images, the BSENSE, BFused, SENSE, and Fused techniques were compared to the square norm reference image (first row, first column of Figure 5.38) and the BGRAPPA and GRAPPA techniques were compared to the averaged k-space reference image (second row, first column of Figure 5.38). Figure 5.39 displays a bar graph of the MSE for each techniques' magnitude reconstructed image. For the graph, the BSENSE and BFused techniques have markedly smaller MSE values than SENSE and the Fused techniques while BGRAPPA and GRAPPA had the smallest MSE values. BGRAPPA has a slightly smaller MSE compared to GRAPPA, but, again, is not the best measure for analyzing signal intensity.

The phase of the reconstructed images for the traditional techniques (second row) and

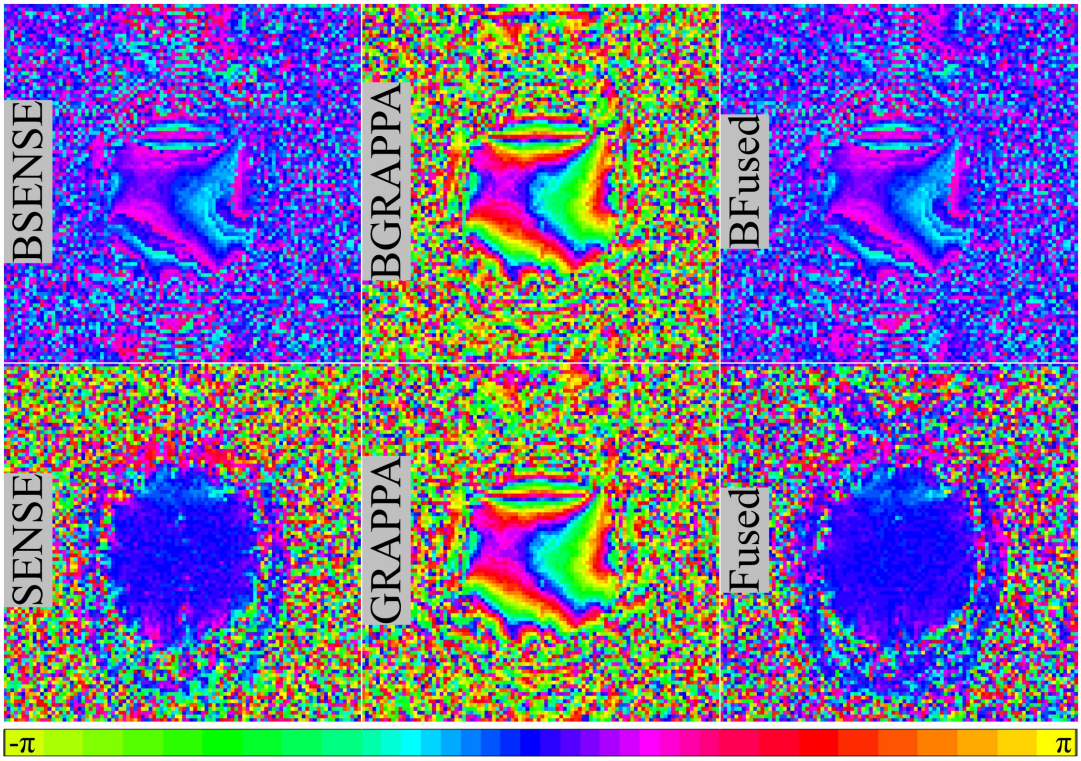

Figure 5.40: The Bayesian reconstructed experimental phase images (first row) and experimental phase images from the traditional reconstruction techniques (second row). Due to the circular nature of phase angles, the color bar for the phase images have wrap-around.

the respective Bayesian approaches (first row) for the first time point in the experimental series is shown in Figure 5.40. The appearance of the BSENSE, BGRAPPA, BFused, and GRAPPA phase reconstructed images are due to the imperfect shims of the magnetic field gradients. An example of this can be seen in the experimental data of the Bruce et al. 2011 paper. In the simulated data used for this dissertation, perfect homogeneity throughout the magnetic gradient field is assumed resulting in clear anatomical structure for the BSENSE, BFused, BGRAPPA, and GRAPPA phase reconstructed images. The BSENSE and BFused reconstructed phase images in Figure 5.40 more accurately represent the phase images and can also be utilized estimate the change in the B-field inhomogeneity, ΔB. The phase from the BGRAPPA and GRAPPA reconstructed images also estimates the imperfections of the shims but do not accurately represent the signal intensities and phase angles of the true

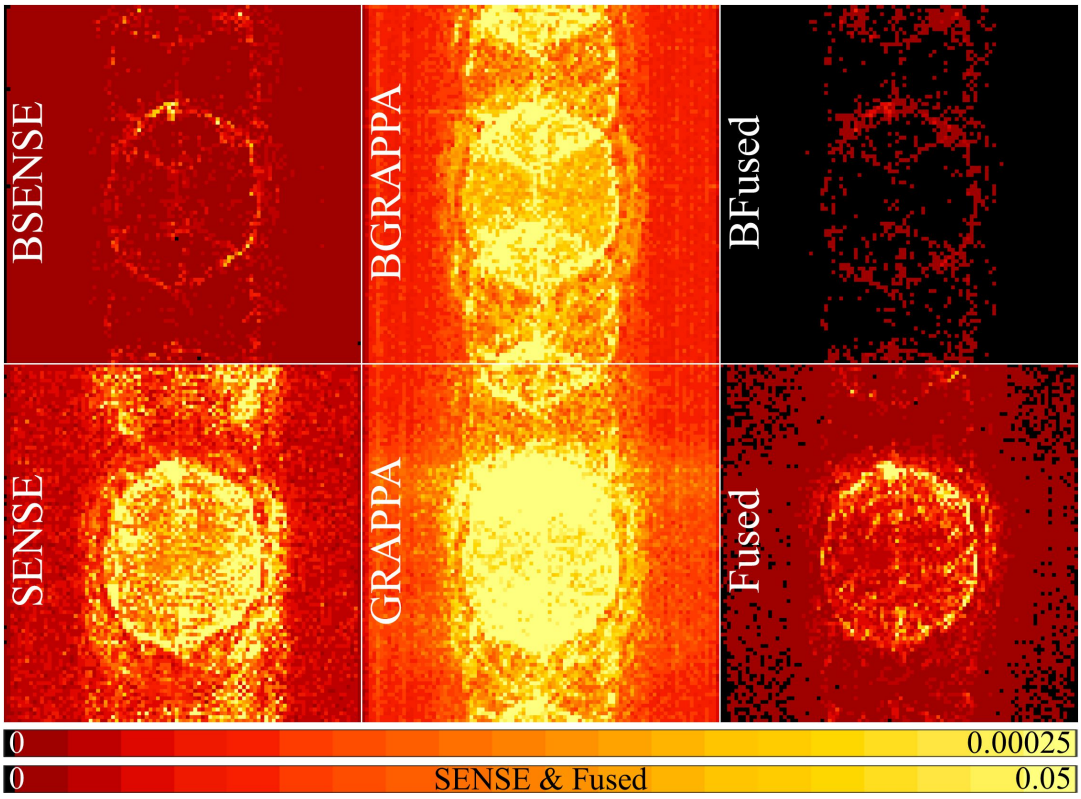

Figure 5.41: Temporal variance of the reconstructed $n_{IMG} = 490$ experimental time series using the traditional techniques (bottom row) and the respective Bayesian approaches (top row).

complex-valued images. The phase of the SENSE and Fused reconstructed images are zero inside the brain, meaning these phase images are of no value.

From the reconstruction of the entire $n_{IMG} = 490$ time series, Figure 5.41 displays the temporal variance of each reconstruction technique. The top row of Figure 5.41 shows the Bayesian reconstruction techniques, and the bottom row shows the traditional reconstruction techniques. Note that the scale for the top color bar only goes up to 0.00025 while the bottom row goes to 0.05 which is 199 times larger. Comparing BGRAPPA and GRAPPA, BGRAPPA has a smaller temporal variance. This shows that the Bayesian techniques have smaller temporal variances compared to the traditional techniques which indicates more ac-

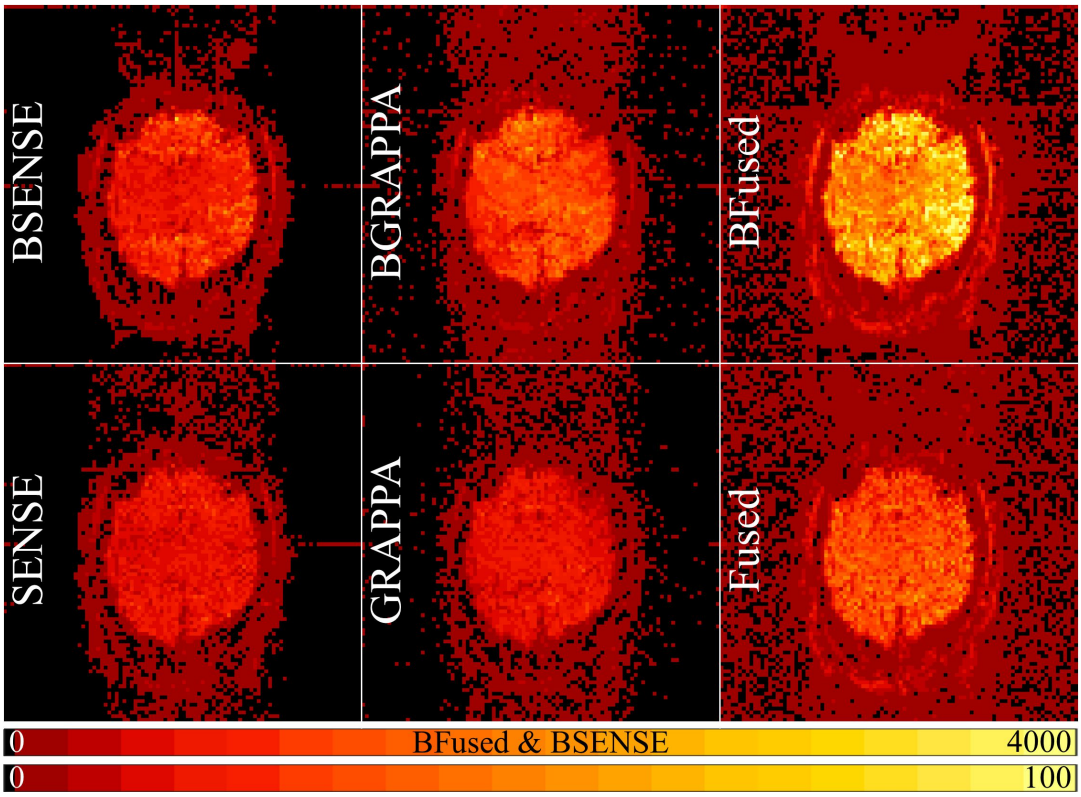

Figure 5.42: Signal-to-noise ratio of the reconstructed $n_{IMG} = 490$ experimental time series using the traditional techniques (bottom row) and the respective Bayesian approaches (top row). The top color bar shows the scale for the BSENSE and BFused techniques while the bottom color bar shows the scale for the other techniques.

curate reconstruction through time. Of the three Bayesian approaches, the BFused technique had the smallest temporal variance with BGRAPPA having the second smallest. For the traditional techniques, SENSE had the largest temporal variance while GRAPPA had the smallest.

Figure 5.42 displays the SNR images using the experimental data for each reconstruction technique utilizing the different number of calibration time points. In Figure 5.42, there is one scale for the BSENSE and BFused techniques which goes to 4000 while the other scale goes to 100 for the other techniques. This scale difference shows that BSENSE and BFused have considerably higher SNR values compared to the other reconstruction techniques like in Figure 5.42. Between BFused and BSENSE, BFused produced the higher SNR values. For the other reconstruction techniques, BGRAPPA had similar SNR values to the Fused

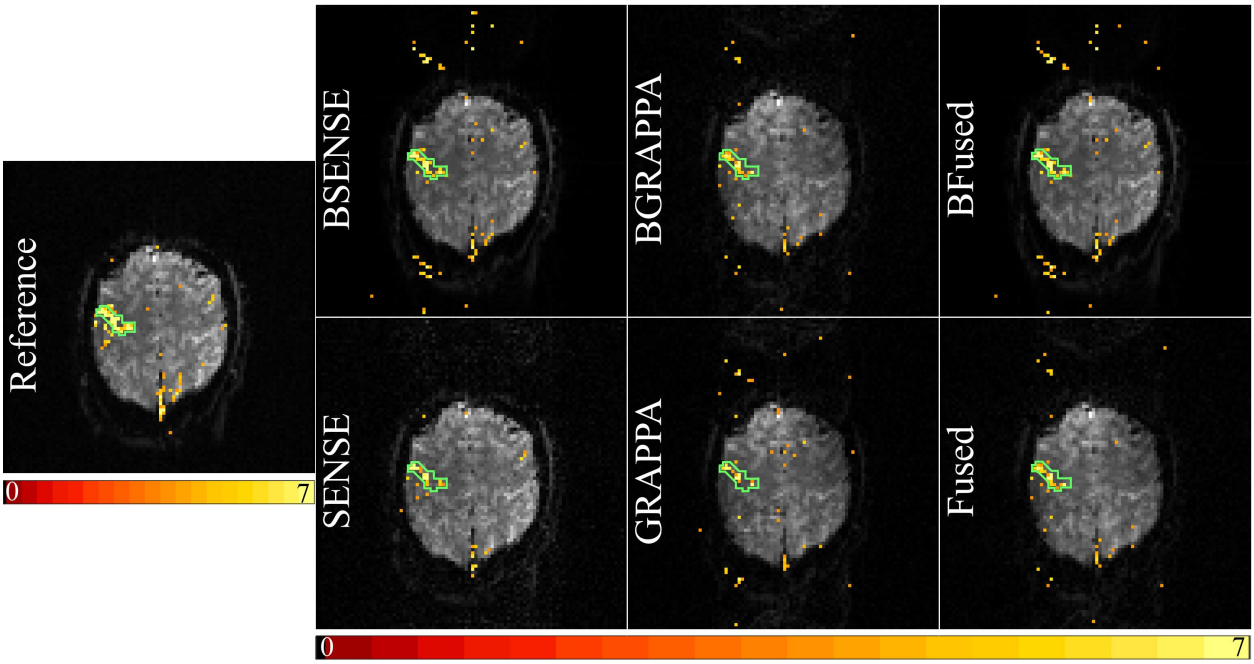

Figure 5.43: Magnitude experimental image with active task voxels in the ROI (first column), statistically significant voxels in the ROI using FDR for the Bayesian reconstructed magnitude experimental images (first row, columns 2-4), and significant voxels in the ROI using FDR for the reconstructed experimental magnitude images using traditional techniques (second row, columns 2-4).

technique with both being greater than SENSE and GRAPPA.

The hypothesis test described in Section 5.1.3 was, again, utilized to determine voxels with a statistically significant signal increase for magnitude-only activation. The statistically significant voxels for the experimental fMRI series for each reconstruction technique is displayed in Figure 5.43, using $n_A = 3$. A 5% false discovery rate (FDR) threshold procedure (Benjamini and Hochberg, 1995; Genovese et al., 2002; Logan and Rowe, 2004) was used for multiplicity correction. The ROI here consists of 28 voxels located in the left motor cortex and is outlined in green for each image in Figure 5.43. The results in Figure 5.43 show that, visually, each reconstruction technique captures the expected task activation in the ROI. However, the Bayesian techniques produced higher task detection, capturing more task active voxels and having higher mean t-values, as shown in Figure 5.44.

Figure 5.44a displays a bar graph of the number of correctly identified task voxels for each reconstruction technique from the magnitude-only task detection in Figure 5.43. This graph shows that BSENSE and BFused identified more task voxels in the ROI compared

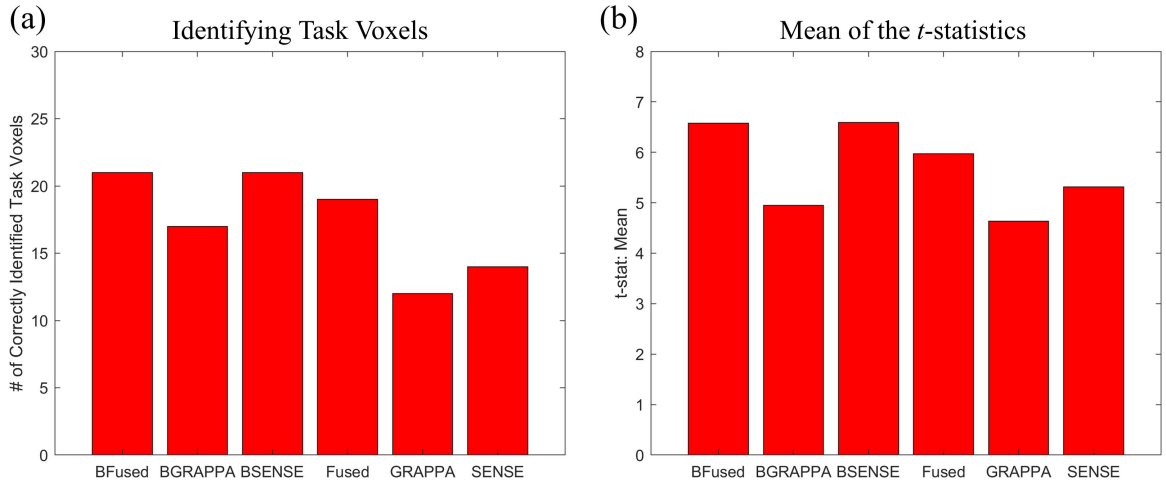

Figure 5.44: (a) Bar graph for number of correctly identified magnitude-only task voxels and (b) a bar graph of mean values for the t-statistics for each reconstruction technique for the experimental data.

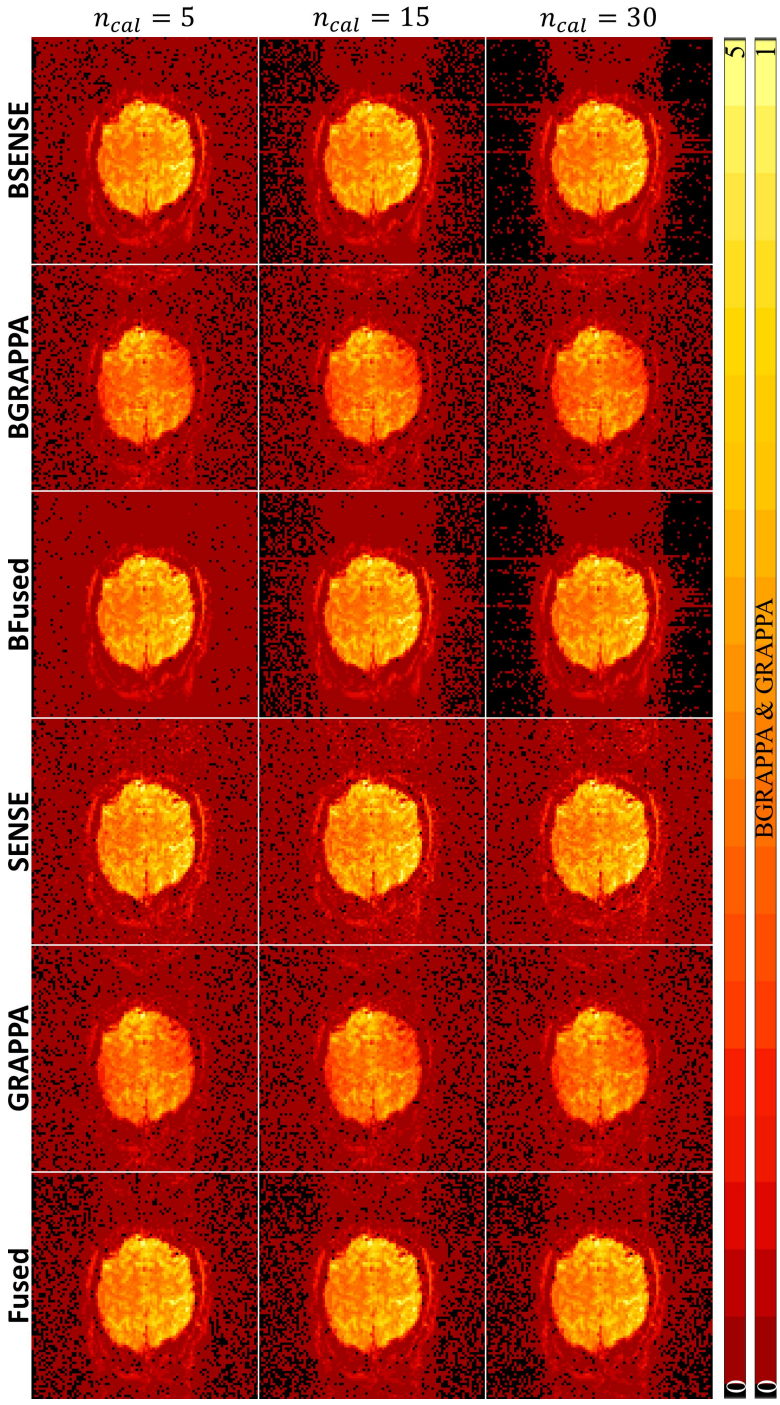

Figure 5.45: Reconstructed magnitude images for different numbers of calibration time points using the traditional and Bayesian image reconstruction techniques for the experimental data. The left color bar shows the scale for the BSENSE, BFused, SENSE, and Fused techniques while the right color bar shows the scale for the BGRAPPA and GRAPPA techniques.

to the other techniques with the Fused technique capturing the third most task voxels. In this bar graph, we can see that BGRAPPA does correctly identify more task voxels than GRAPPA and SENSE. Figure 5.44b displays a bar graph of the mean t-statistic values in the ROI for each reconstruction technique. The results show that BSENSE and BFused have highest mean t-statistic values with both of these techniques having virtually the same mean t-statistic value. The Fused reconstruction does have a higher mean t-value than the other techniques with BGRAPPA having a slightly lower mean t-statistic value than SENSE despite identifying more task voxels in the ROI.

Similar to the simulation study, we evaluated how the number of calibration time points, n_{cal}, affected the reconstructed images. For the pre-scan calibration analysis, we fixed the acceleration factor to be $n_A = 3$ for the subsampled k-space coil arrays of the experimental time series. Then we set the number of calibration time points to be $n_{cal} = 5, 10, 15, 20, 25, 30$ for separate hyperparameter assessments. After assessing the hyperparameters using each number of calibration time points, the experimental time series with the subsampled coil spatial frequency arrays were reconstructed using the traditional and Bayesian reconstruction techniques.

Figure 5.45 displays the results for the magnitude reconstructed images using the different numbers of calibration time points from each technique. From Figure 5.45, we can see that increasing the number of calibration time points decreases the noise level for the BSENSE and BFused techniques while the other techniques remain seemingly unaffected. The Bayesian reconstruction techniques seem to produce slightly less noise images inside the brain (and mostly outside the brain) compared to the traditional techniques. The MSE for inside the brain along with the entropy for each of the reconstruction techniques using various numbers of calibration time points were calculated to quantify the results shown in Figure 5.45. Shown in Figure 5.46a, the MSE for BSENSE and BFused are smaller than the

SENSE and Fused techniques as they are compared to the square norm reference magnitude image. Both BGRAPPA and GRAPPA have smaller MSE values than the rest of the reconstruction techniques, with BGRAPPA being slightly smaller, but, again, are compared to the averaged $k-$-space reference magnitude image. For the entropy plot in Figure 5.46b, the BSENSE and BFused have the smallest entropy values (except for $n_{cal} = 5$) with BSENSE being slightly smaller. This plot also shows that the Fused technique has smaller entropy values compared to BGRAPPA, which has smaller entropy values compared to SENSE and GRAPPA. The entropy values for the Bayesian reconstruction techniques appear to decrease as the number of calibration time points increases.

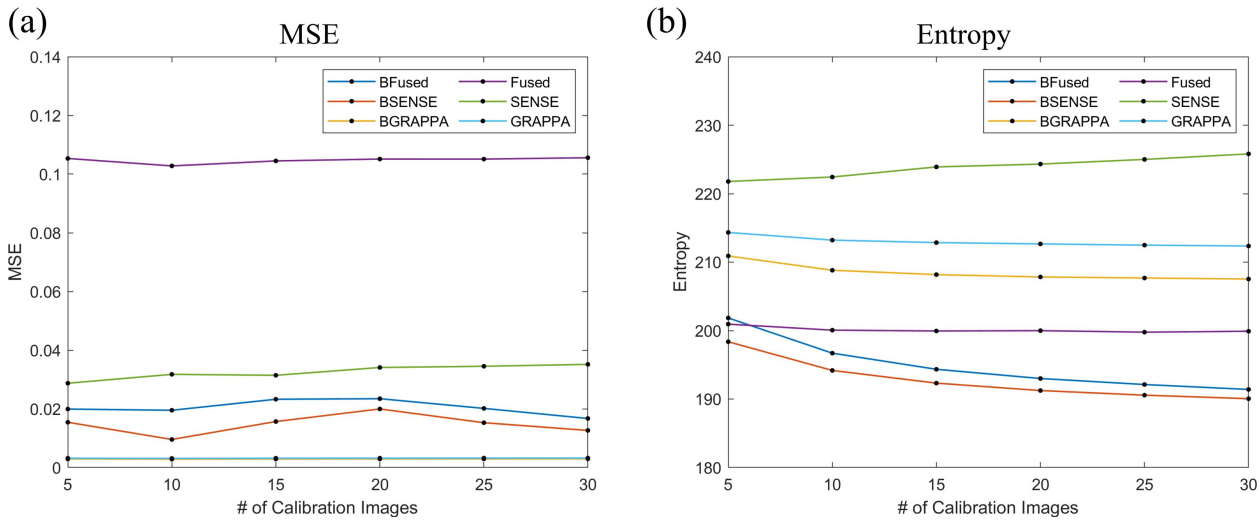

Figure 5.46: (a) MSE for inside the brain for each reconstruction technique compared to the square norm reference magnitude image or the averaged coil k-space arrays reference magnitude image for each number of calibration time points. (b) Entropy plot for each reconstruction technique using the various number of calibration time points. For both plots, BSENSE is the orange line, BGRAPPA is the yellow line, BFused is the blue line, SENSE is the green line, GRAPPA is the light blue line, and Fused is the purple line.

The appearance of the phase reconstructed images for different numbers of calibration time points is similar to the those shown in Figure 5.40. That is, the BSENSE, BGRAPPA, BFused, and GRAPPA reconstructed phase images show the imperfections of the shims and the SENSE and Fused are close to zero inside the brain providing no information. These

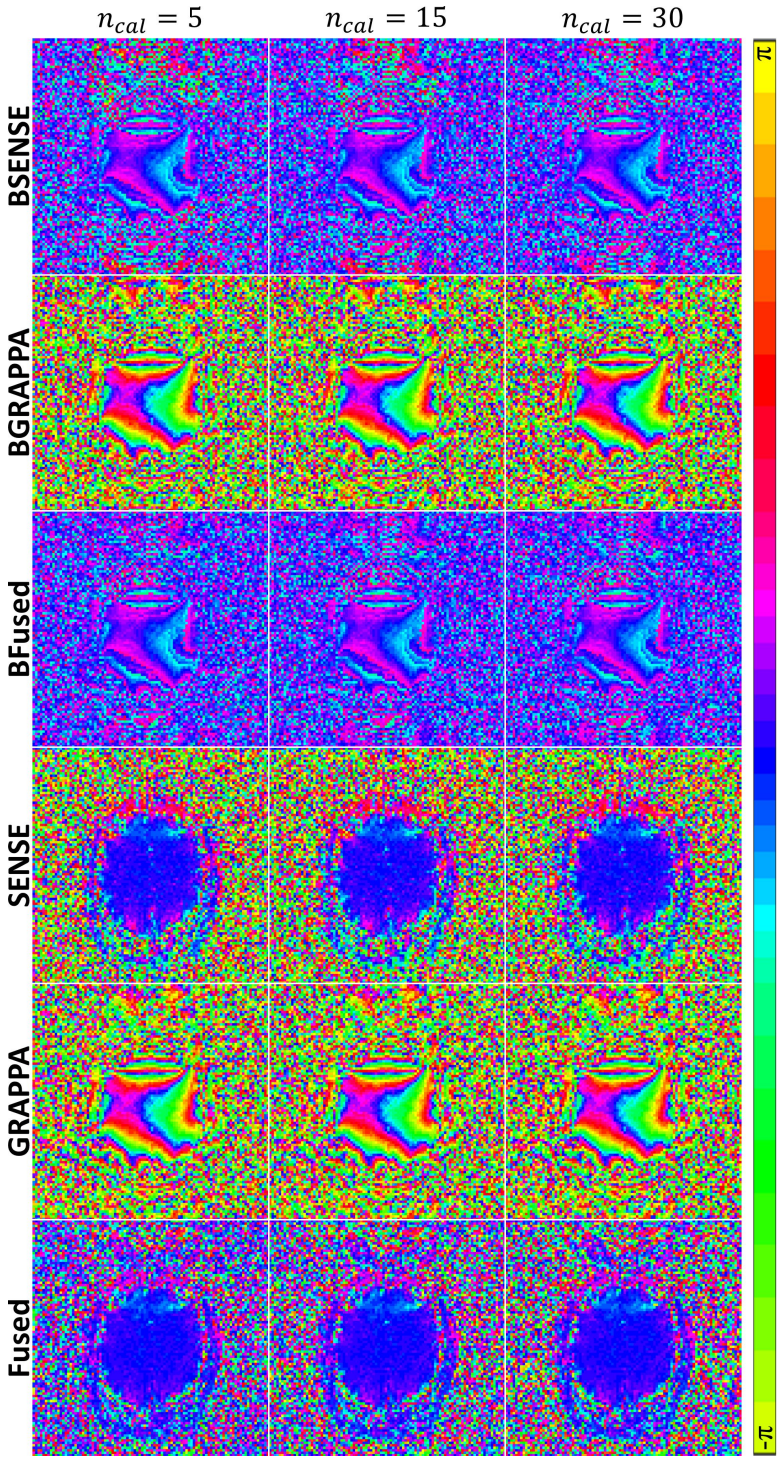

Figure 5.47: Reconstructed experimental phase images for different numbers of calibration time points using the traditional and Bayesian image reconstruction techniques. Due to the circular nature of phase angles, the color bar for the phase images have wrap-around.

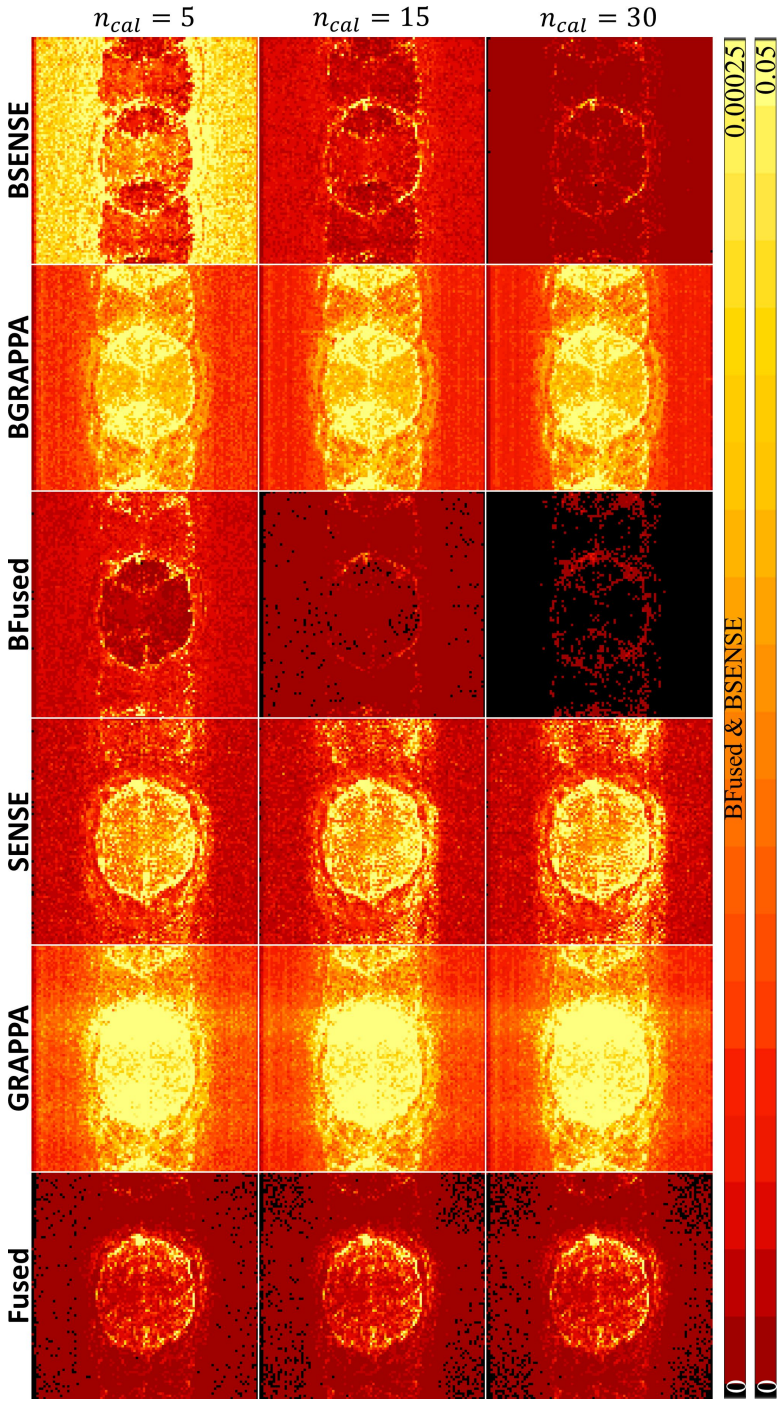

Figure 5.48: Temporal variance for different numbers of calibration time points using the traditional and Bayesian image reconstruction techniques for the experimental data. The left color bar shows the scale for the BSENSE and BFused techniques while the right color bar shows the scale for the other techniques.

results are shown in Figure 5.47. From these results, we can see that increasing the number of calibration time points used for hyperparameter assessment has little to no effect on the reconstructed phase images.

Figure 5.48 displays the temporal variance for each reconstruction technique utilizing various calibration time points for the experimental data. In this figure, there are two different scales for the color bars: one for the BSENSE, BGRAPPA, BFused, and GRAPPA techniques which go to 0.00025 and the other for the SENSE and Fused techniques that go to 0.05, similar to that shown in Figure 5.41. With BGRAPPA having smaller temporal variance for the experimental data compared to GRAPPA, the Bayesian reconstruction techniques produce more accurate reconstructed images through time compared to the traditional techniques. Between BSENSE and BFused, BFused has a much smaller temporal variance than BSENSE. Also, increasing the calibration time points decreases the temporal variance for both BSENSE and BFused reconstruction techniques. For the traditional reconstruction techniques, SENSE appears to have a highest temporal variance continuing to show that the SENSE technique under performs with the non-task analysis of these image reconstruction techniques.

In Figure 5.49, we have have two scales for the color bars where BSENSE and BFused follow the color bar that goes up to 4000 while the others follow the color bar that go up to 100. This indicates that BSENSE and BFused produce substantially larger SNR values compared to the other reconstruction techniques. In Figure 5.49, it appears that the BGRAPPA and Fused techniques produce similar SNR values with SENSE having the smallest SNR values. From Figure 5.49, we can see that increasing the number of calibration time points increases the SNR inside the brain for the BSENSE and BFused. For the other techniques, the SNR values inside the brain appear unchanged as the calibration time points increase while decreasing SNR values outside the brain for BGRAPPA, GRAPPA, and the

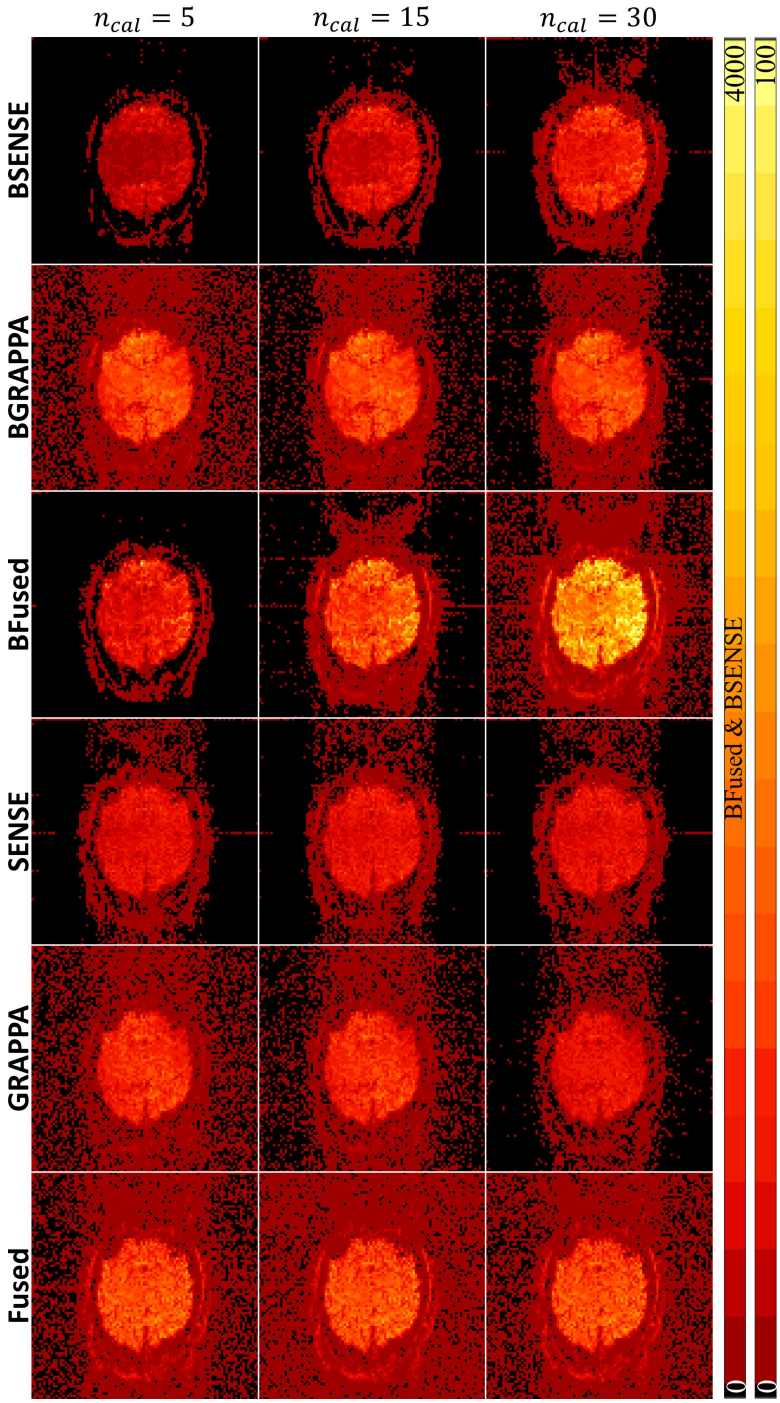

Figure 5.49: SNR for different number of calibration time points using the traditional and Bayesian image reconstruction techniques for the experimental data. The left color bar shows the scale for the BSENSE and BFused techniques while the right color bar shows the scale for the other techniques.

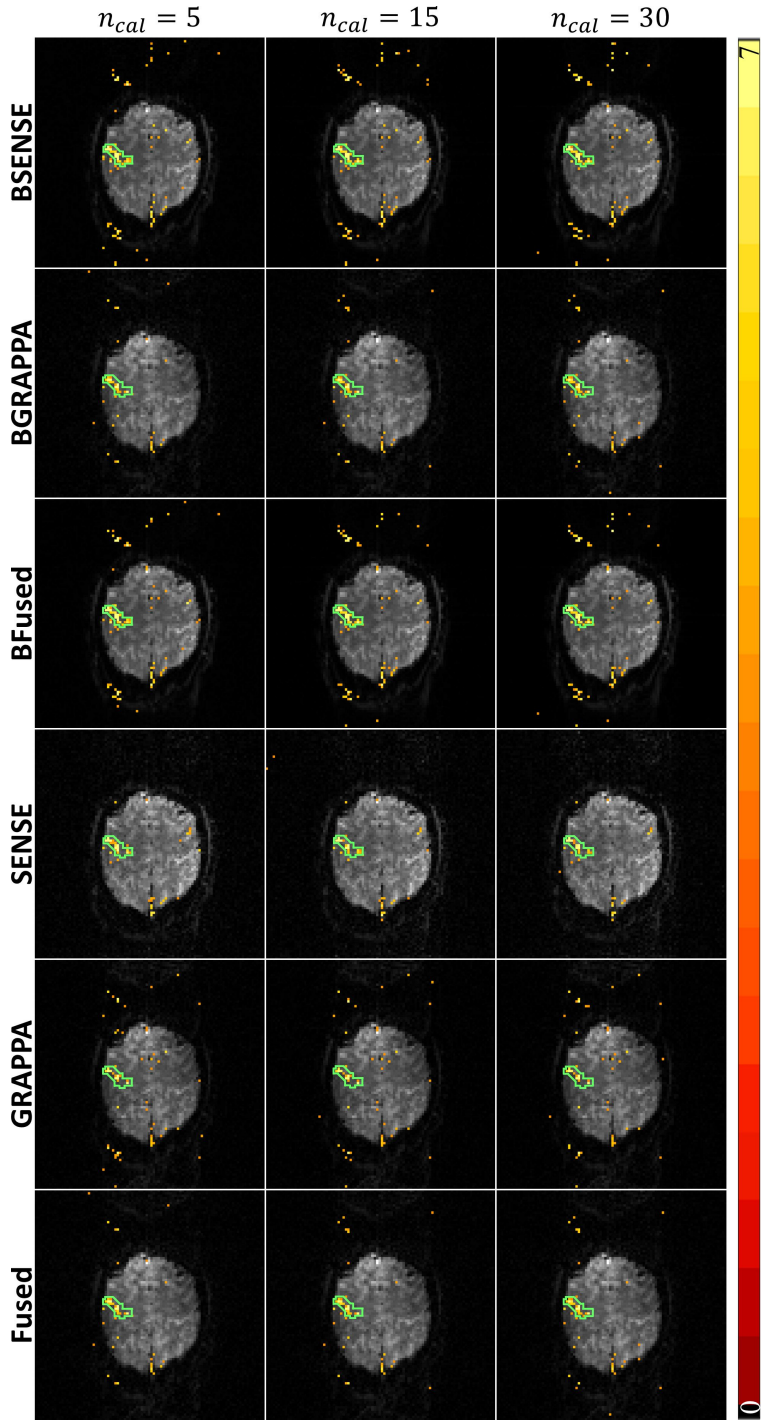

Figure 5.50: Statistically significant voxels in the ROI using FDR for the Bayesian reconstructed experimental magnitude images (rows 1-3), and significant voxels in the ROI using FDR for the reconstructed experimental magnitude images using traditional techniques (rows 4-6) for different numbers of calibration time points.

Fused techniques.

We also evaluated how utilizing different number of calibration time points affects the magnitude-only task detection results. Figure 5.50 displays the magnitude-only task detection results for different numbers of calibration time points using each reconstruction method. Similar to Figure 5.43, each reconstruction technique captures activation in the ROI outlined in green, but the BSENSE and BFused techniques appear to have the strongest power in detecting the task. Visually, it appears that increasing the number of calibration time points have no effect on task detection.

These results are further analyzed in Figure 5.51. In Figure 5.51a shows a plot of the number of correctly identified task voxels in the ROI using different numbers of calibration images for each reconstruction technique. From this, we can see that BSENSE and BFused capture more task voxels than the other techniques. The plot also shows that the Fused technique captures more task voxels than BGRAPPA. BGRAPPA still correctly identifies more task voxels than SENSE and GRAPPA, but still performs slightly worse than the

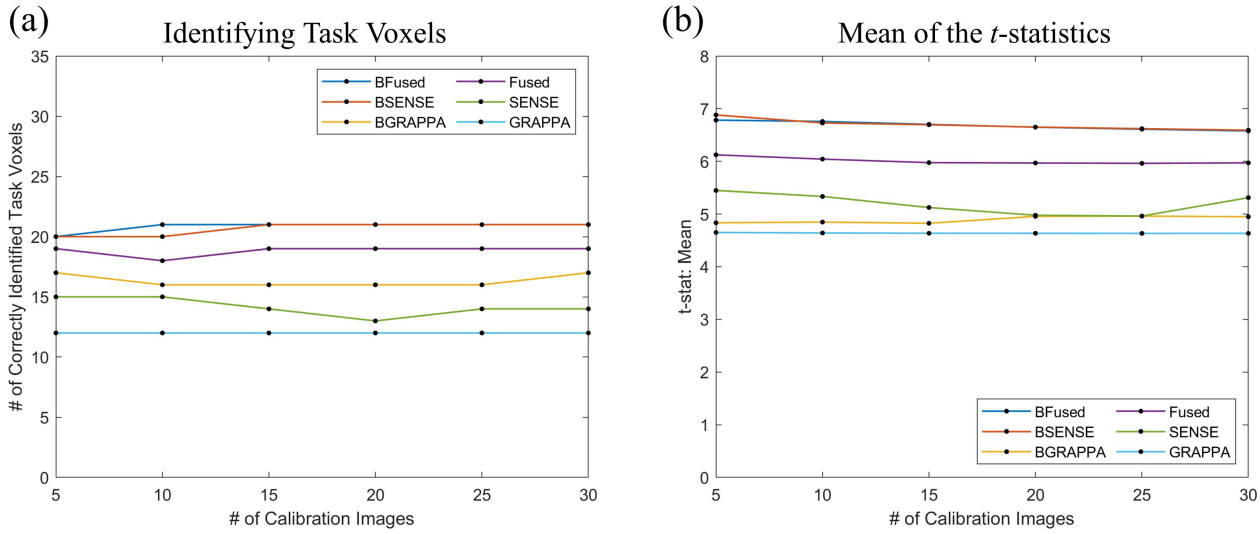

Figure 5.51: (a) Plot of correctly identified magnitude-only task voxels and (b) a plot of the mean values for the t-statistics for each reconstruction technique using different numbers of calibration time points for hyperparameter assessment for the experimental data.

Fused technique with the experimental task analysis. Of all the reconstruction techniques, GRAPPA appears to detect the least amount of task voxels and have the lowest mean t-statistic values as shown in 5.51b. In this plot, BSENSE and BFused have the highest mean t-values with BSENSE being slightly higher at each point (except at $n_{cal} = 30$). Despite having more voxels identified as task, BGRAPPA has slightly smaller mean t-values than SENSE. This could mean that there is less variation between the t-statistic values in the ROI for BGRAPPA. Overall, increasing the number of calibration time points used for hyperparameter assessment has minimal effect for each of the reconstruction techniques (except SENSE) as exhibited in both plots.

Using the same prior information at each time point in the series of subsampled fMRI data could potentially lead to correlation, as mentioned in Section 5.1.2. The same sampling of the calibration time points process outlined in Section 5.1.2 was also followed for correlation analysis using the experimental data. Figure 5.52a illustrates the average correlation

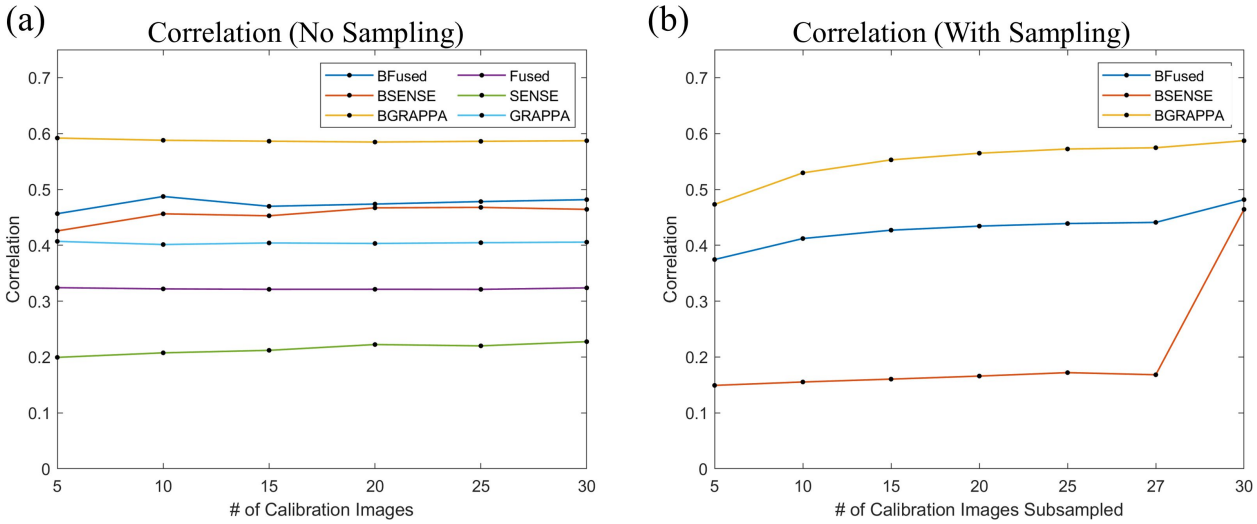

Figure 5.52: (a) Correlation between previously aliased voxels for each reconstruction technique for the experimental data. (b) Correlation between previously aliased voxels for each Bayesian reconstruction technique using sampling of the calibration time points without replacement for the experimental data. For plot a, BSENSE is the orange line (same in plot b), BGRAPPA is the yellow line (same in plot b), BFused is the blue line (same in plot b), SENSE is the green line, GRAPPA is the light blue line, and Fused is the purple line.

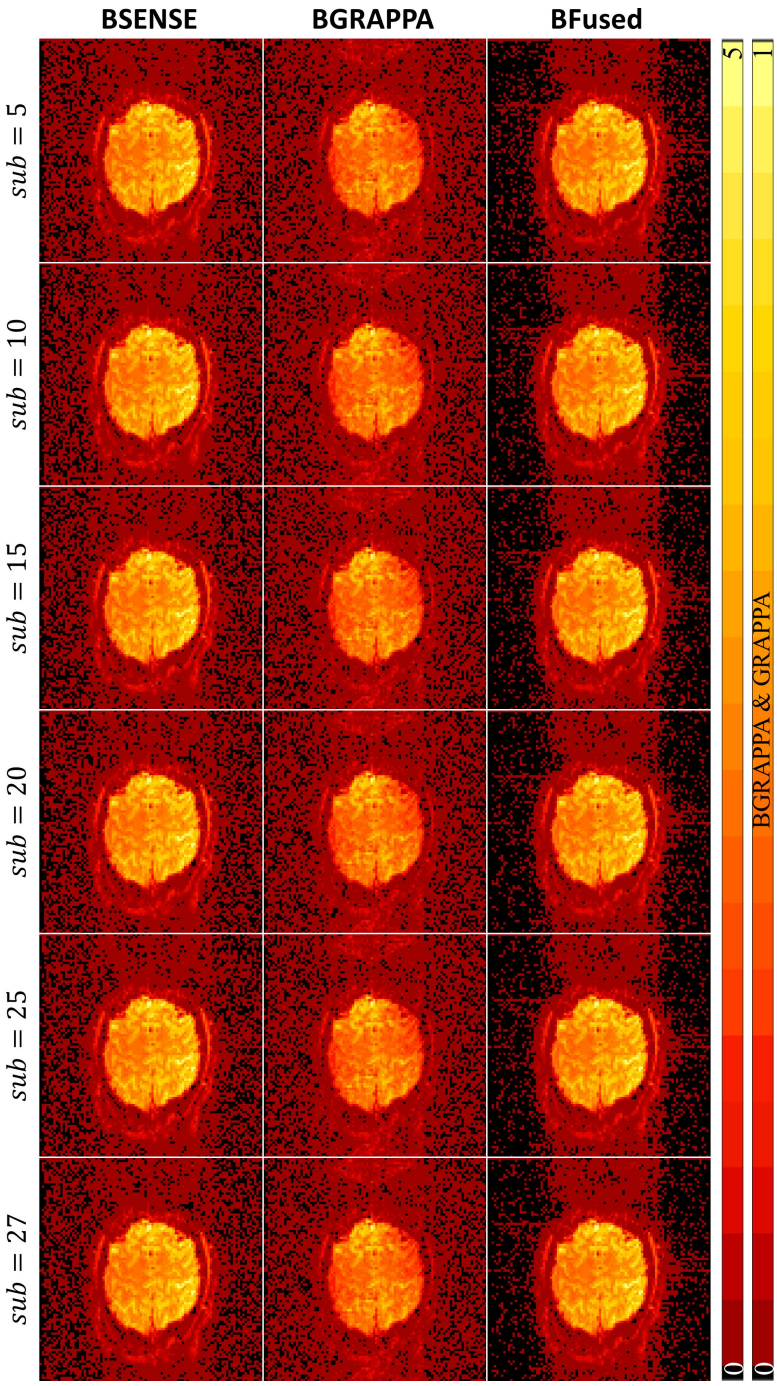

Figure 5.53: Reconstructed experimental magnitude images for different samples of calibration time points from hyperparameter assessment for the Bayesian image reconstruction techniques. The left color bar shows the scale for the true magnitude, BSENSE and BFused techniques while the right color bar shows the scale for BGRAPPA.

between voxels and the voxels they were previously aliased for each reconstruction technique using different numbers of calibration time points. The magnitude of the reconstructed experimental time series is used for the correlation estimation. Analyzing the plot shows that the traditional reconstruction techniques have lower correlation estimates than the Bayesian techniques. The correlation estimates for GRAPPA are close to the correlation estimates for the Bayesian techniques but are still less than each of them. The correlation appears relatively steady for each reconstruction technique as the number of calibration time points increase.

Figure 5.52b demonstrates the effects of sampling the calibration time points on voxel correlation while, again, decreasing the prior scalars to $n_v = 1$, $n_S = 1$, $n_l = 1$ and $n_w = 1$. The plot in Figure 5.52b shows the average correlation between all voxels and the voxels they were previously aliased with for sampling sizes of 5, 10, 15, 20, 25, and 27, out of 30 calibration time points, comparing them to the non-sampling methods. The results indicate that sampling the calibration time points remarkably decreases the correlation for BSENSE only. For BGRAPPA and BFused, the correlation does slightly decrease but increases as the sampling size increases ultimately being close to the correlation without sampling.

Figure 5.53 shows the magnitude of the reconstructed images for each Bayesian reconstruction technique using different sample sizes of the calibration time points. The results displayed in this figure show that sampling the calibration time points has little effect on the magnitude reconstructed images inside the brain. Figure 5.15 also shows that as the sampling size increases, the noise level for BSENSE, BGRAPPA, and BFused remains unchanged.

Figure 5.54 shows the magnitude-only task detection results for BSENSE (first column), BGRAPPA (second column), and BFused (third column). For BSENSE, sampling the calibration time points reduces the task leakage while minimally losing task detection power.

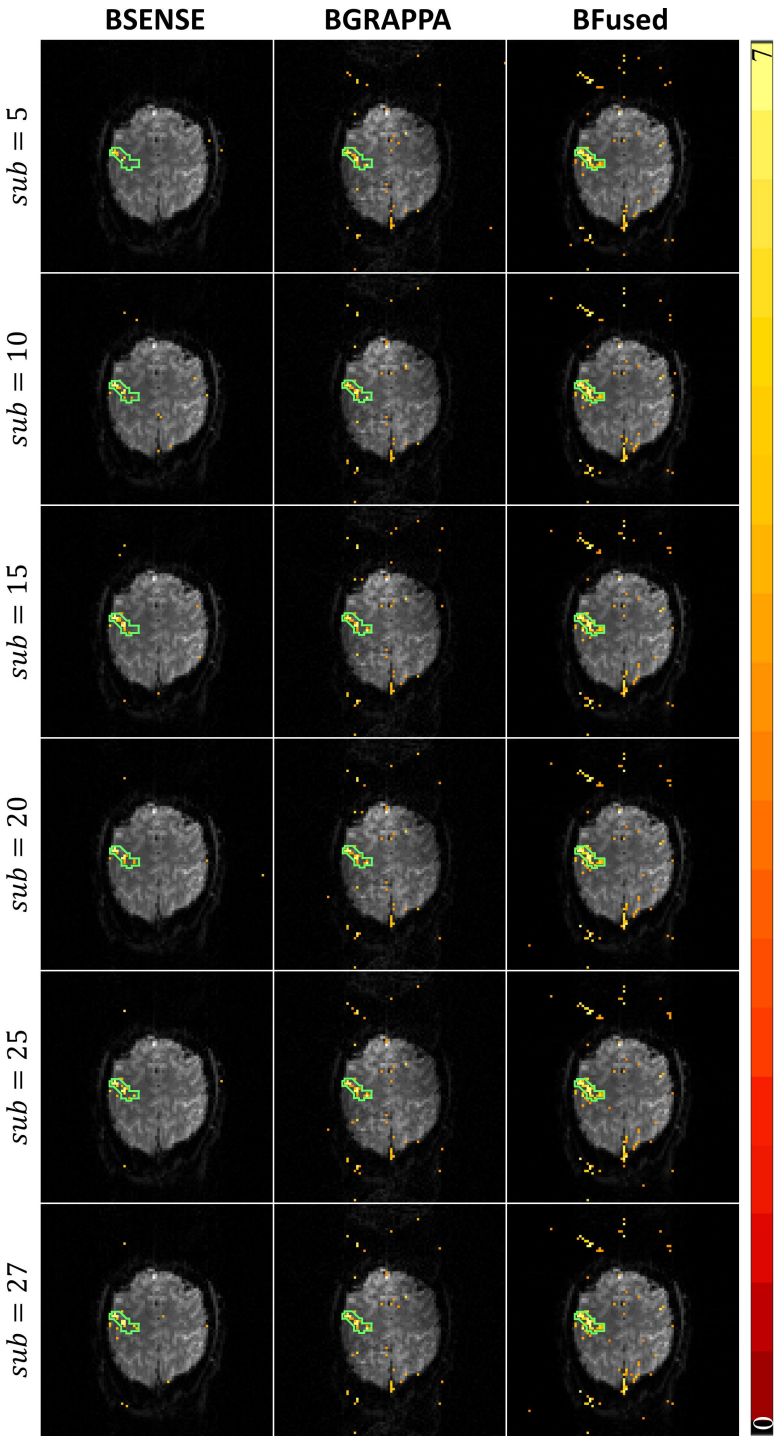

Figure 5.54: Statistically significant voxels in the ROI using FDR for the Bayesian reconstructed magnitude images utilizing different samples of calibration time points for hyperparameter assessment for the experimental data.

For BGRAPPA and BFused, task leakage is hardly mitigated by sampling the calibration time points.

This is more evident in Figure 5.55 which shows the identified task voxels in plot (a) and the mean t-values in plot (b). In Figure 5.55a, we can see that sampling the calibration time points minimally affects the number of identified task voxels. However, it does slightly increase the mean of the t-values in Figure 5.55b, which would need a little more investigating. For BSENSE, the number of correctly identified voxels is slightly less than BGRAPPA, but the mean of the t-statistic values is similar to BGRAPPA.

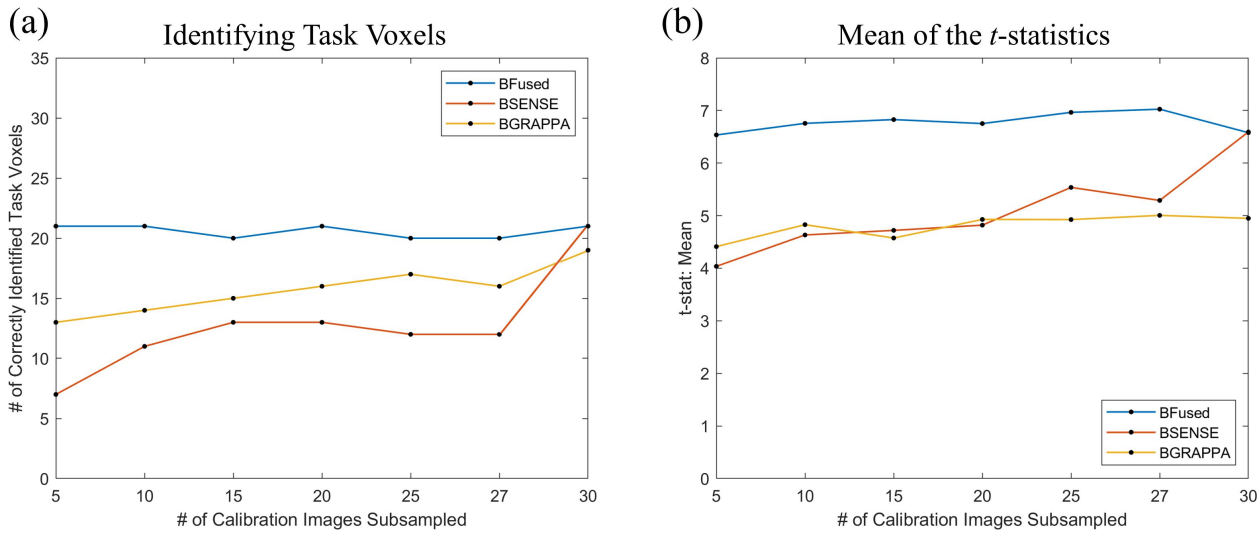

Figure 5.55: (a) Plot of correctly identified magnitude-only task voxels and (b) a plot of the mean values for the t-statistics for each Bayesian reconstruction technique using a different number of calibration time points for hyperparameter assessment for the experimental data.

Along with analysis of the number of calibration time points, we evaluate how different acceleration factors affect the results for each reconstruction technique for the experimental data. Here, we fixed the number of calibration time points to be $n_{cal} = 30$ for hyperparameter assessment and set the acceleration factors of the experimental time series to be $n_A = 2, 3, 4, 6, 8, 12$. In the acceleration factor analysis, the SENSE technique is not used to reconstruct using and acceleration factor of $n_A = 12$ due to the underdetermined system.

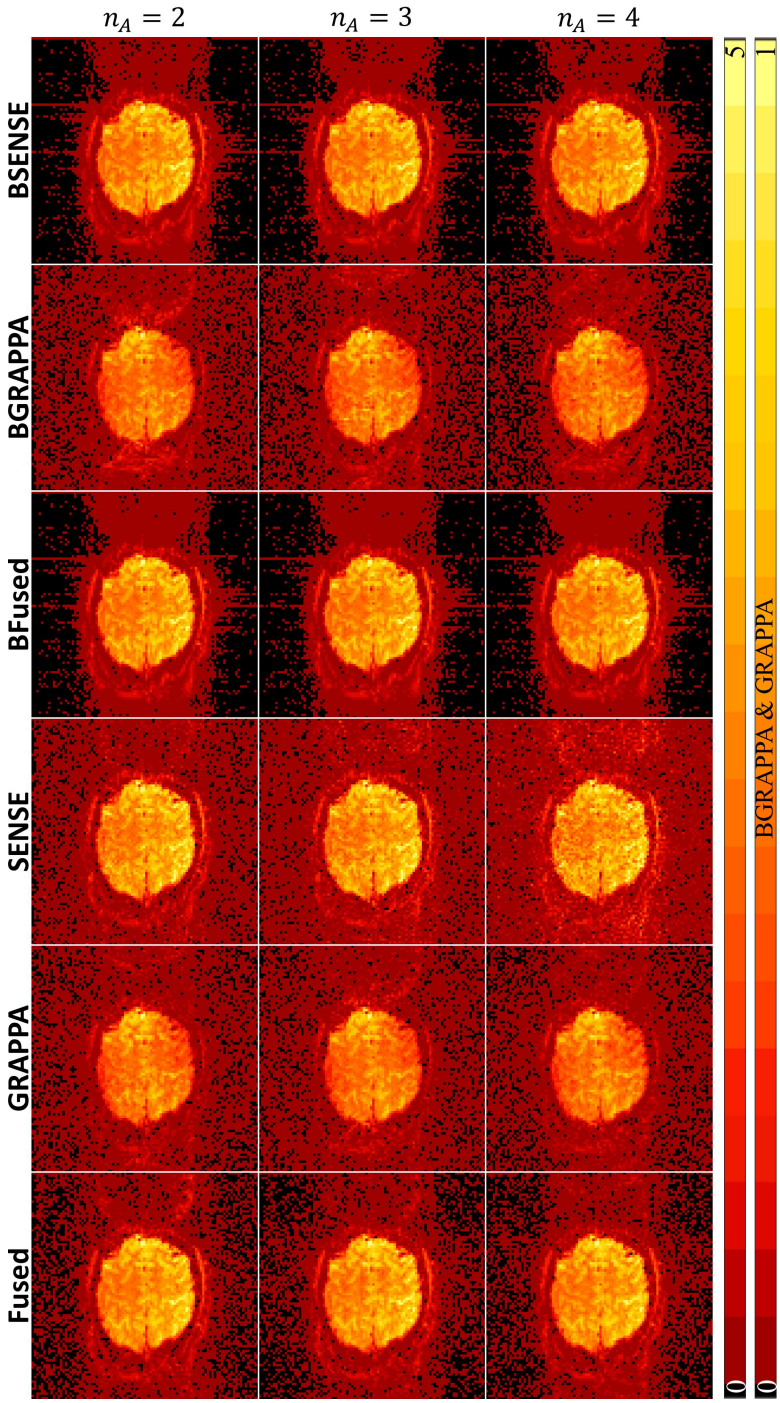

Figure 5.56: Reconstructed magnitude images for different acceleration factors using the traditional and Bayesian image reconstruction techniques for the experimental data. The left color bar shows the scale for the true magnitude, BSENSE, BFused, SENSE, and Fused techniques while the right color bar shows the scale for the reference magnitude, BGRAPPA, and GRAPPA techniques.

Only the results for $n_A = 2, 3, 4$ are shown for some of the figures simply to see how increasing the acceleration factor effects the reconstruction results. These subsampled experimental coil k-space arrays with separate acceleration factors were reconstructed into full images using each of the reconstruction techniques, comparing the results for all methods.

The results displayed in Figure 5.56 show that the magnitude images from each of the reconstruction techniques, except for SENSE, are negligibly affected by increasing the acceleration factor. The noise level for inside and outside the brain for SENSE appears to increase as the acceleration factor increases. Similar to the simulated results, the magnitude reconstructed images from the traditional techniques have slightly more noise than the Bayesian magnitude reconstructed images for inside the brain. For BGRAPPA, there appears to be more noise outside the brain compared to the Fused reconstructed magnitude images.

The MSE for inside the brain along with the entropy for each of the reconstruction

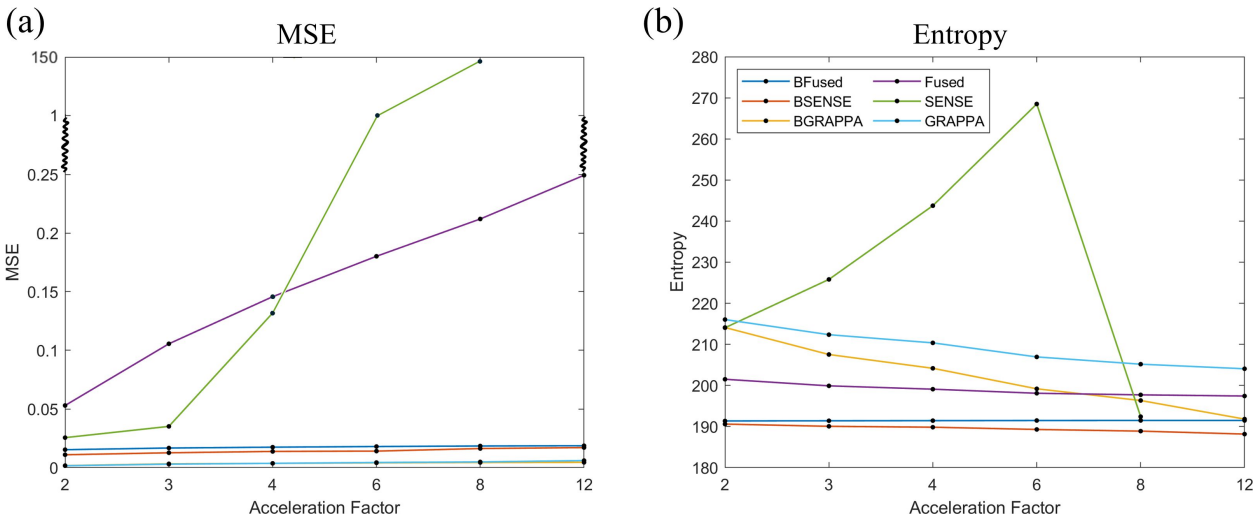

Figure 5.57: (a) MSE for inside the brain for each reconstruction technique compared to the square norm reference magnitude image or the averaged coil k-space arrays reference magnitude image for different acceleration factors. (b) Entropy plot for each reconstruction technique applying different acceleration factors. For both plots, BSENSE is the orange line, BGRAPPA is the yellow line, BFused is the blue line, SENSE is the green line, GRAPPA is the light blue line, and Fused is the purple line.

techniques for different acceleration factors were calculated to quantify the results shown in Figure 5.56. From Figure 5.57a, the MSE estimates for SENSE reconstruction techniques are larger than 0.25 at acceleration factors larger than $n_A = 4$, causing the change in the y-axis the plot. The MSE plot evidently shows that the MSE for BSENSE and BFused are smaller than the SENSE and Fused techniques as they are compared to the square norm reference magnitude image. In Figure 5.57a, BGRAPPA and GRAPPA have smaller MSE estimates than the other reconstruction techniques. The BGRAPPA and GRAPPA techniques, however, are compared to the averaged k-space reference magnitude image which is not a good indicating of accurate reconstructing the signal intensities. For the entropy plot in Figure 5.46b, the BSENSE and BFused have the smallest entropy values with BSENSE slightly decreasing as the acceleration factor increases. This plot also shows that the Fused technique has smaller entropy values compared to BGRAPPA (except for $n_A = 8$ and $n_A = 12$), which has smaller entropy values compared to SENSE and GRAPPA. The entropy values for BGRAPPA and GRAPPA decrease as the number of calibration time points increases.

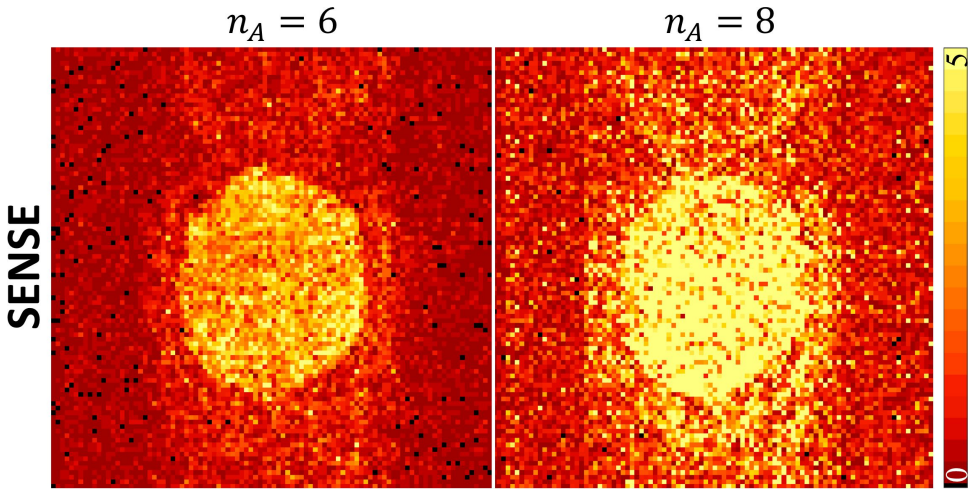

Figure 5.58: SENSE magnitude reconstructed images with $n_A = 6$ (left) and $n_A = 8$ (right) for the experimental data.

Figure 5.58 displays the magnitude of the reconstructed experimental images using SENSE for acceleration factors $n_A = 6$ (left) and $n_A = 8$ (right). This figure shows that the

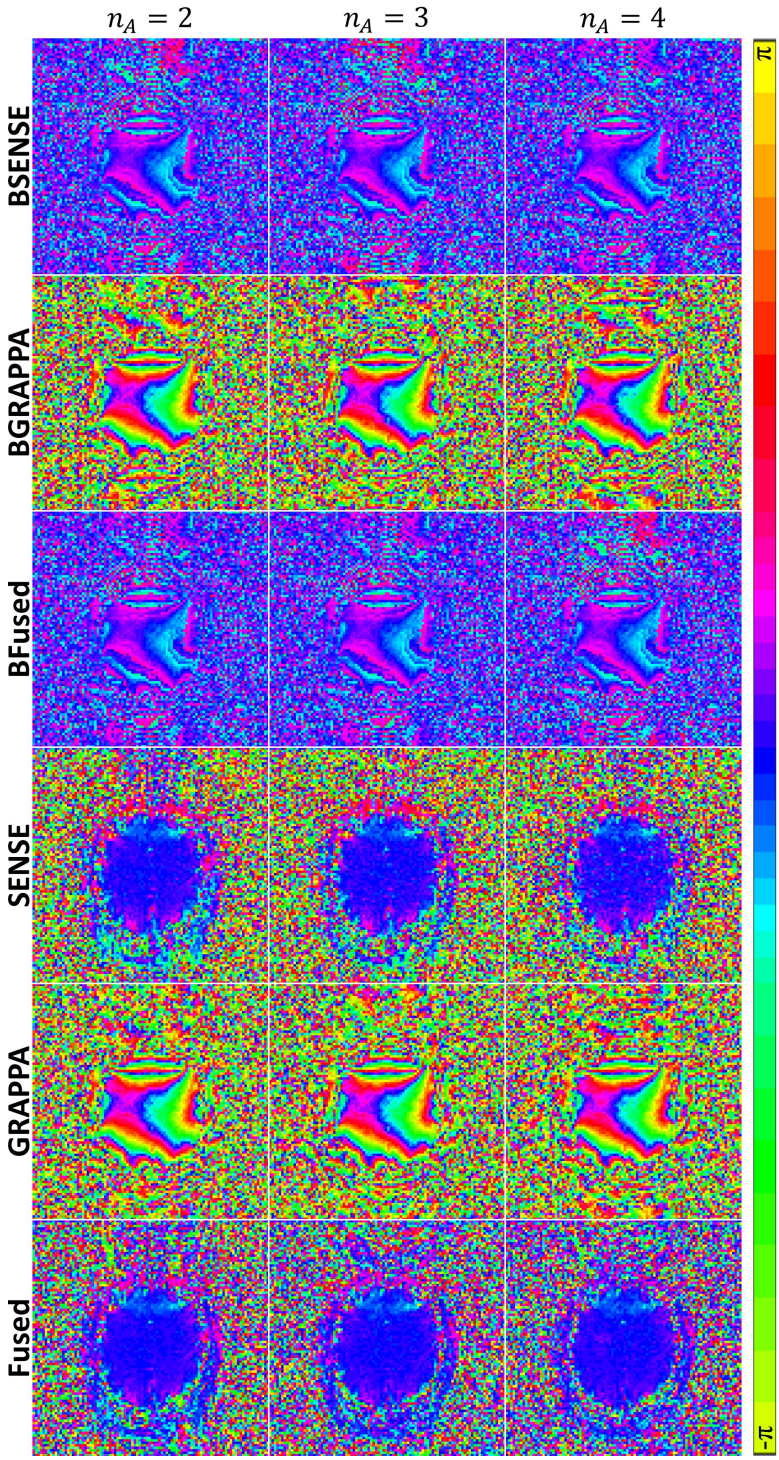

Figure 5.59: Reconstructed phase images for different acceleration factors using the traditional and Bayesian image reconstruction techniques for the experimental data. Due to the circular nature of phase angles, the color bar for the phase images have wrap-around.

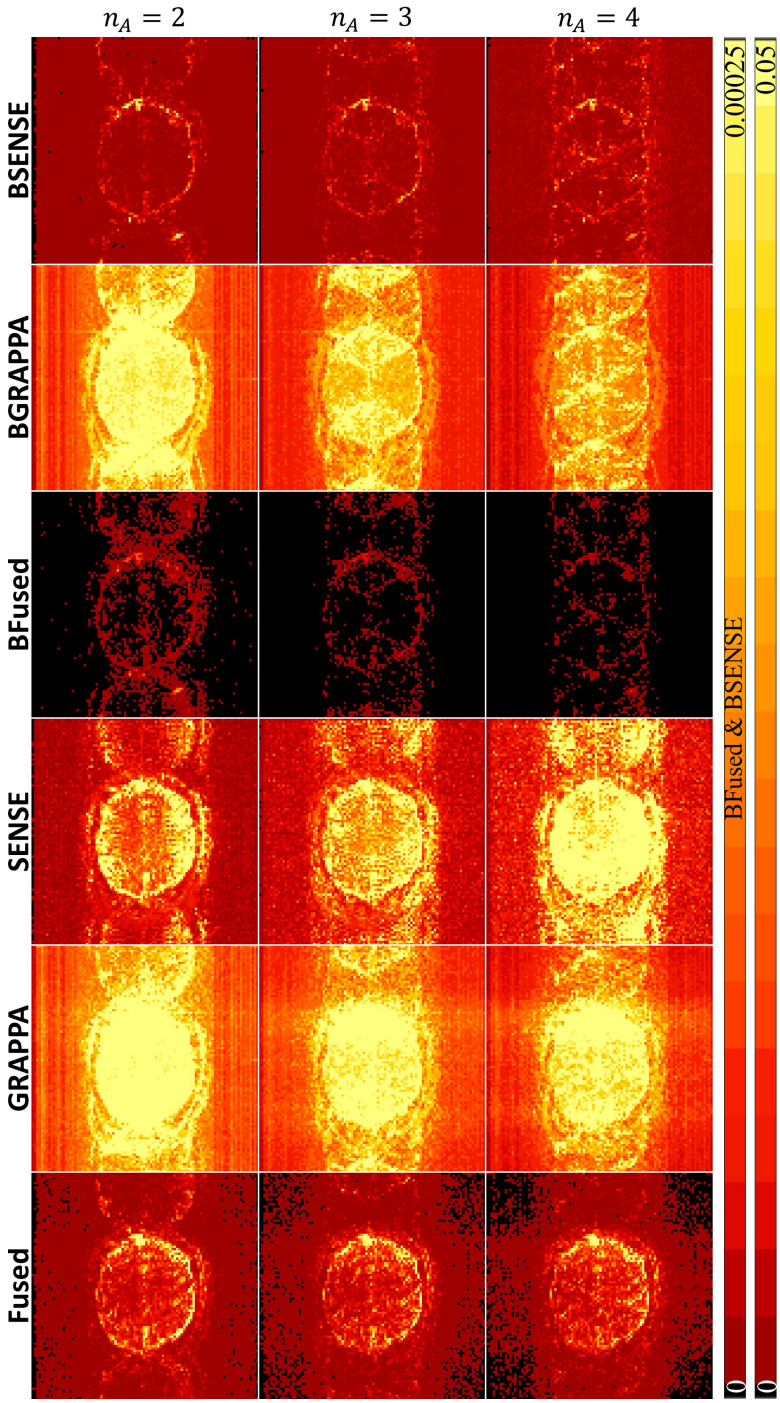

Figure 5.60: Temporal variance for different acceleration factors using the traditional and Bayesian image reconstruction techniques for the experimental data. The left color bar shows the scale for the BSENSE and BFused techniques while the right color bar shows the scale for the other techniques.

MSE plot (Figure 5.57a) is noticeably higher for SENSE as the magnitude images appear to lose anatomical structure due to the higher noise level. This also explains why the SENSE line (green) in the entropy plot (Figure 5.17b) drops substantially when the acceleration factor increases $n_A = 8$.

The appearance of the phase reconstructed images for different acceleration factors is similar to the those shown in Figures 5.40 and 5.47 where the BSENSE, BGRAPPA, BFused, and GRAPPA reconstructed phase images show the imperfections of the shims and the SENSE and Fused are close to zero inside the brain. These reconstructed phase images for different acceleration factors are shown in Figure 5.59. From Figure 5.59, we can see that increasing the acceleration factor has little to no effect on the reconstructed phase images except for SENSE where the noise level inside the brain increases. For SENSE, the noise level overtakes the phase image and makes the entire completely noisy, leaving no trace of even a brain outline.

Figure 5.60 displays the temporal variance for each technique reconstructing with different acceleration factors applied to the experimental data. Like Figures 5.41 and 5.48, this figure has one scale for the color bars that BSENSE, BGRAPPA, BFused, and GRAPPA techniques are on which go to 0.00025 and one scale for the SENSE and Fused techniques that go to 0.05. Since BGRAPPA has smaller temporal variance compared to GRAPPA for each acceleration factor, the Bayesian reconstruction techniques, again, produce more accurate reconstructed images through time compared to the traditional techniques. Evaluating Figure 5.60, we see that BFused has a much smaller temporal variance than BSENSE. Also, increasing the acceleration factor decreases the temporal variance for BSENSE, BGRAPPA, BFused, and GRAPPA reconstruction techniques while increasing the temporal variance for the SENSE and Fused techniques.

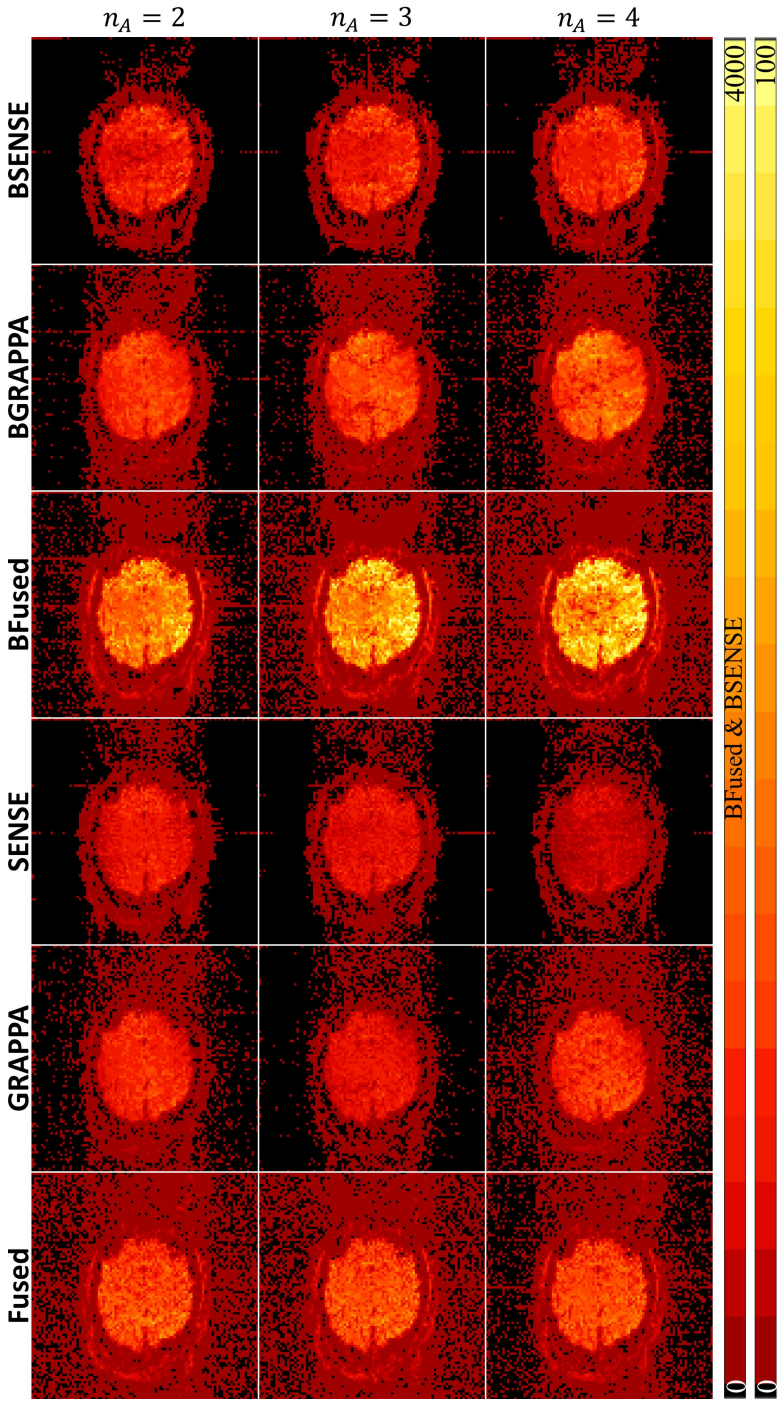

Figure 5.61: SNR for different acceleration factors using the traditional and Bayesian image reconstruction techniques for the experimental data. The left color bar shows the scale for the BSENSE and BFused techniques while the right color bar shows the scale for the other techniques.

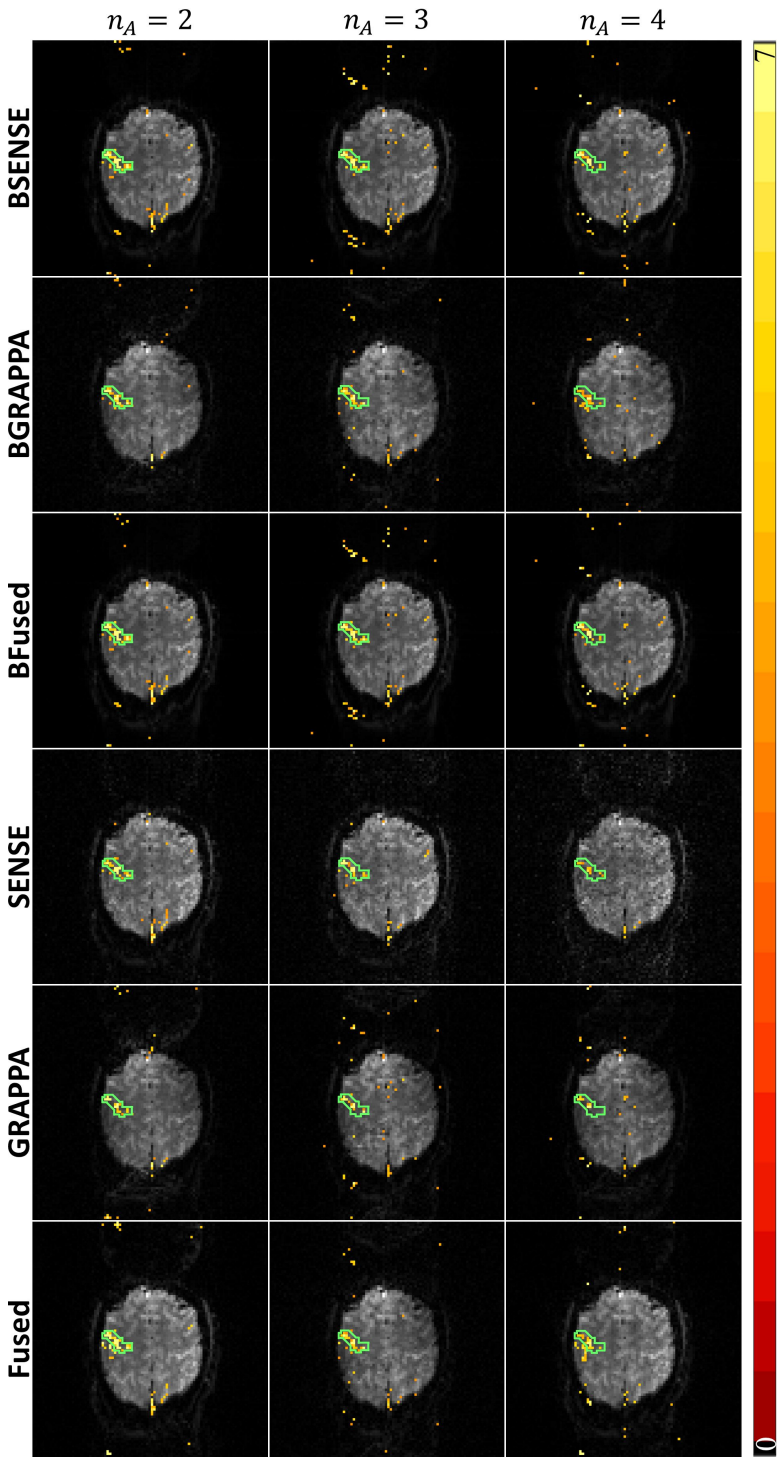

Figure 5.62: Statistically significant voxels in the ROI using FDR for the Bayesian reconstructed magnitude images (rows 1-3), and significant voxels in the ROI using FDR for the reconstructed magnitude images using traditional techniques (rows 4-6) for different acceleration factors for the experimental data.

Similar to Figures 5.42 and 5.49, Figure 5.61 has two scales for the color bars: one that BSENSE and BFused follows that goes up to 4000 and one that the other techniques follow the color bar that go up to 100. This, again, indicates that BSENSE and BFused produce substantially larger SNR values compared to the other reconstruction techniques. In Figure 5.61, it appears that the BGRAPPA and Fused techniques produce similar SNR values for different acceleration factors with SENSE having the smallest SNR values. Figure 5.61 shows that increasing the acceleration factor increases the SNR inside the brain for the BSENSE, BGRAPPA, BFused, and GRAPPA. For SENSE and Fused, the SNR values inside the brain appear to slightly decrease as the acceleration factor increases.

To further evaluate the effects of different acceleration factors, analysis of magnitude-only task detection for each reconstruction technique is analyzed in Figure 5.62. Analyzing Figure 5.62, each reconstruction technique captures activation in the ROI, outlined in green, but the BSENSE and BFused techniques appear to have stronger detection power than the rest of the methods. Visually, it appears that increasing the acceleration factor noticeably decreases task detection for GRAPPA and SENSE but only slightly decreases for the other reconstruction techniques.

Figure 5.63a shows a plot of the number of task voxels identified as active in the ROI for different acceleration factors for each reconstruction technique. From this, we can see that BSENSE and BFused produce similar results as the number of task voxels are the same (except for $n_A = 8$ and $n_A = 12$). Also, for each acceleration factor, BSENSE and BFused detected the most task active voxels compared to the other techniques. The plot shows that BGRAPPA captures the same amount or more task voxels than the Fused technique (except for $n_A = 6$) for each acceleration factor. Of all the reconstruction techniques, GRAPPA detects the least amount of task voxels for $n_A = 2, 3, 4$ while SENSE detects the least amount of task voxels for $n_A = 6, 8$ and Fused for $n_A = 12$. In Figure 5.63b, BSENSE and

BFused clearly have the highest mean t-values with BSENSE being slightly higher at each point (except at $n_A = 12$). Despite having more voxels identified as task, BGRAPPA has slightly smaller mean t-values than SENSE for each acceleration factor except $n_A = 8$. This, again, could mean that there is less variation between the t-statistic values in the ROI for BGRAPPA. Overall, increasing the acceleration factor decreases effectively capturing task activation for each reconstruction technique in both plots.

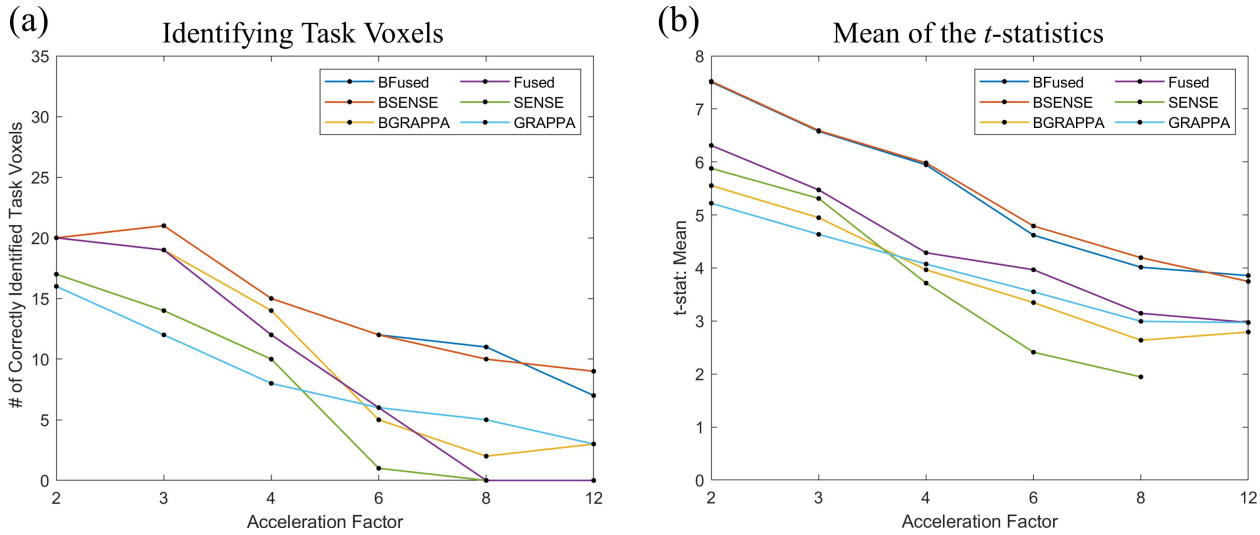

Figure 5.63: (a) Plot of correctly identified magnitude-only task voxels and (b) a plot of the mean values for the t-statistics for each reconstruction technique using different acceleration factors for the experimental data.

CHAPTER 6: Discussion

For MR imaging, Parallel imaging techniques such as SENSE (Pruessmann et al., 1999) and GRAPPA (Griswold et al., 2002) have facilitated subsampling of k-space and reduced image acquisition times. This allows practitioners to reduce acquisition time with each slice, increase the number of images or slices, reconstruct higher resolution images, or a combination of these in the same time as fully sampled k-space depending on the acceleration factor. The acceleration factor in an fMRI experiment is determined by how important time is in completing a scan. The number of coils used in an experiment is dependent on the facility and the coil configurations that facility possesses.

Applying an acceleration factor in an fMRI experiment can significantly reduce the acquisition time of spatial frequency arrays and volume images, but taking the IFT of the subsampled k-space yields aliased coil images. SENSE parallel image reconstruction simultaneously unaliases and combines the aliased coil images, resulting a full FOV single, composite brain image. This image reconstruction method can be difficult in the presence of an ill-conditioned design matrix. GRAPPA is another parallel image reconstruction that estimates the unacquired spatial frequencies that are skipped during the acquisition of the subsampled k-space arrays yielding full FOV coil spatial frequency arrays. However, GRAPPA has its drawbacks which include low image quality, low SNR, and weakened task detection power at higher acceleration factors. Here, we include a model that fuses both GRAPPA and SENSE since GRAPPA operates in the spatial frequency domain and SENSE operates in the image domain. Despite this Fused model, there are still discrepancies with applying this Fused model as valuable prior information that can incorporated into the image reconstruction is discarded. Hence, we introduce a Bayesian approaches to GRAPPA, SENSE, and the Fused method. Using more available information from the calibration spatial frequencies

and images to assess the hyperparameters, our proposed Bayesian approaches successfully reconstructed a series of simulated non-task images without any aliasing artifacts. These Bayesian reconstructed images were also shown to have numerous improvements over the reconstructed images of the traditional techniques when applied to both simulated and experimental fMRI data.

6.1 Summary of Reconstruction Results

The simulated non-task results show that overall, the Bayesian techniques outperform the traditional techniques. The BFused and BSENSE techniques appear to reconstruct magnitude images more accurately with having lower MSE values while closely resembling the true simulated phase image. The Bayesian techniques also decrease the temporal variance which increases the SNR values with BFused being the best of three Bayesian methods. Despite BGRAPPA being the weakest of the three Bayesian methods, it still produces better results compared to the three traditional techniques. Having more calibration time points for hyperparameter assessment improves the results for BFused and BSENSE while increasing the acceleration factor has negligible effects on the non-task results for the Bayesian techniques.

For the task analysis of the simulated fMRI data, BSENSE and BFused, by far, outperformed the other techniques while BGRAPPA still had better results than the traditional techniques. These methods identified more task voxels in the ROI and had higher mean t-statistic values for both magnitude-only and phase-only task activation models. For the experimental fMRI analysis, BSENSE and BFused had lower MSE and entropy values for the reconstructed magnitude images, had lower temporal variance, high SNR values, and had the highest power of task detection.

The Bayesian approaches did have a higher correlation with previously aliased voxels and task leakage, so sampling of the calibration time points was deployed to possibly mitigate these issues. It effectively reduced the correlation and task leakage for BSENSE (except for the simulated magnitude-only task activation), but hardly had positive results for BGRAPPA and BFused. This sampling study is somewhat limited with using $n_{cal} = 30$ calibration time points. Increasing the total number of calibration time points could potentially improve the results for the Bayesian reconstruction techniques.

Considering all the results in this dissertation, from a practical standpoint, the BFused image reconstruction would be the best technique to use for real-world applications. This model utilizes both spatial frequency and image information to reconstruction the subsampled fMRI data. It is set up to be objectively automated, but also allows flexibility for subjective prior information to be implemented as well. This statement is backed by the results shown throughout this dissertation.

6.2 Other Completed Work

The BSENSE model used for this dissertation assumed that is no covariance between the n_C coils. This is common practice in fMRI but is not necessarily a correct assumption (Bruce et al., 2012). A model has been written out that incorporates coil covariance and aliased voxel covariance. This model just needs further testing with the simulated and experimental data. This has not but can also be applied to the BFused model as well.

This dissertation used the full posterior distribution for reconstructing images, meaning available prior information was quantified on all three parameters for BSENSE (v, S, and σ^2), and inherently BFused, and utilized for parameter estimation. We also analytically integrated out σ^2 yielding a marginal posterior where v and S are the only two unknowns to

be estimated. Integrating out σ^2 produces a joint Student-t posterior for S and v from which we obtained Gibbs sampling based marginal estimates consistent with the three-parameter model.

From the Bayesian models, we evaluated the estimation of the coil sensitivities (S in BSENSE and BFused), the noise variance of the aliased coil measurements (σ^2 in BSENSE and BFused). This extended work is exhibited in Appendix A. We also examine the different coil sensitivity information that is utilized between SENSE and BSENSE, and innately Fused and BFused.

6.3 Future Work

More work can be completed with what prior information is incorporated in the reconstruction. With more available calibration time points, the sampling of this calibration information can include more sampling scenarios. For BGRAPPA and BFused, instead of sampling entire coil spatial frequency arrays, we can sample frequencies individually. Suppose we wanted to sample 15 of the 30 calibration time points for hyperparameter assessment. For the sampling experiment completed in Sections 5.1.2, 5.1.5, and 5.2.2, we used the same 15 sampled calibration time points to assess the hyperparameters for every unacquired spatial frequency in each array and then sample another 15 for the next point in the time series and so on. For sampling the frequencies individually, we would sample 15 calibration time points for a single unacquired spatial frequency in the array, assess the hyperparameters, and then for the next point in the array, we would sample another 15. This process would be repeated until the hyperparameters are assessed for all the unacquired spatial frequencies in the array at a single point in the time series. This means that every unacquired spatial frequency in the array at every point in the time series would have different assessed hyperparameters. We can also obtain calibration time points that has some task information and incorporate

those in the reconstruction at the points in the time series where the task performed.

The reason for sampling the calibration time points was to potentially reduce the task leakage experienced by the Bayesian approaches in Sections 5.1.5 and 5.2.2. Another method that can be used to reduce the task leakage voxels is to place a Lagrange optimization constraint that is set to minimize the correlation between the previously aliased voxels.

In the Bayesian models, time is independent when reconstructing the subsampled k-space arrays. For future work, we may also need to consider a time dimension in our models to more accurately reconstruct images as the series is acquired.

For this dissertation, only the MAP estimate using the ICM algorithm was used to reconstruct the time series for both the simulated and experimental data. Since we have posterior conditionals for each of the parameters, this allows us to use other estimation techniques such as the MCMC Gibbs sampling method. This method was not presented due to the Gibbs sampler being more computationally expensive when running a long series of images so it is not as practical to use compared to evaluating the MAP estimate. This does not mean there is no value in running a Gibbs sampler, as it has the additional benefit of quantifying uncertainty. For instance, it can be utilized on a shorter series of images, providing us with more statistical information about any voxel, hypothesis testing between two reconstructed images, or identifying which voxels are outside the brain for masking. We could also hybridize the ICM and Gibbs sampler where we start with a few iterations of the ICM algorithm followed by a short, no-burn Gibbs sampler. For the BFused technique, the ICM algorithm was used for estimation in both k-space and image space. However, this would allow some flexibility with using Gibbs sampler at either or both estimation points (k-space and image space). Our Bayesian approaches allows for more options of how to run an fMRI experiment based on the objective of the scan compared to the traditional techniques.

APPENDIX A

Coil Sensitivity and Residual Noise

In this chapter of the appendix, we analyze the estimated coil sensitivities and the residual noise from BSENSE reconstruction.

A.1 BSENSE Estimated Coil Sensitivities

Along with the unaliased voxel values, v, BSENSE estimated the coil sensitivities, S, for each TR in the time series. Figure A.1a displays the true magnitude image (center) and the true magnitude coil sensitivities starting with coil 1 on the top middle and going clockwise to coil 8 in the top left. Figure A.1b has the same setup as the BSENSE magnitude reconstructed image and coil sensitivities for the first TR of the 490 reconstructed non-task time series (outlined in Section 5.1.2) using $n_{cal} = 30$ and an acceleration factor of $n_A = 3$.

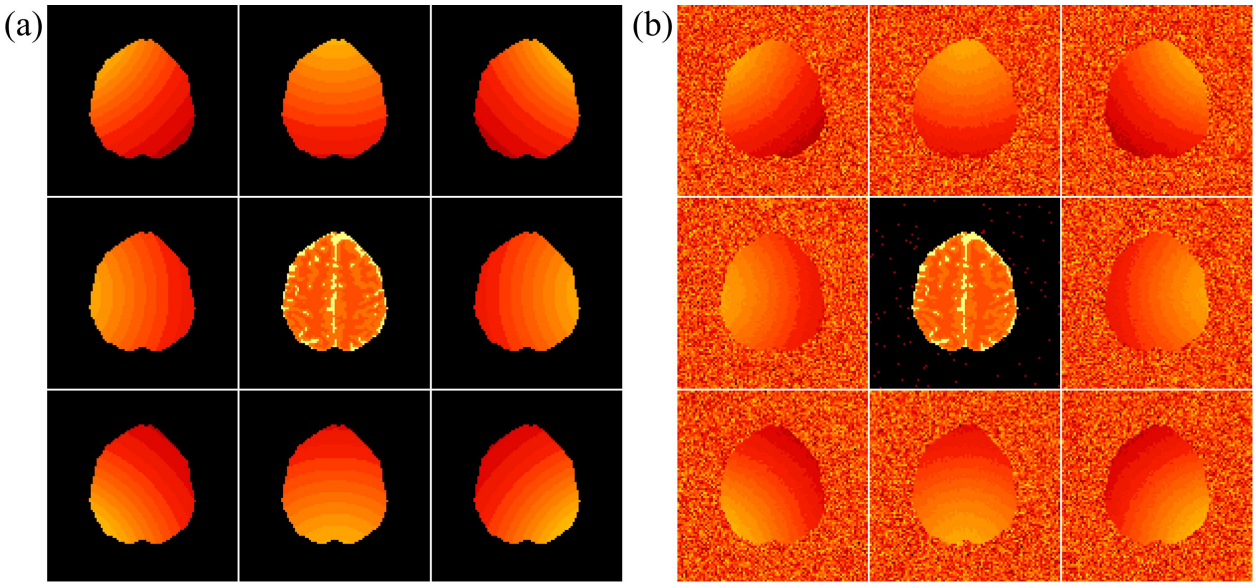

Figure A.1: (a) True magnitude coil sensitivities surrounding the true magnitude image and (b) BSENSE estimated magnitude coil sensitivities surrounding the reconstructed magnitude image.

The estimated BSENSE coil sensitivities appear to be similar to the the true coil sensitivities inside where the brain would be.

The estimated coil sensitivities were also analyzed using different number of calibration images (5, 10, 15, 20, 25, 30) and acceleration factors (2, 3, 4, 6, 8, 12). With fixing $n_A = 3$, Figure A.2a exhibits the MSE for the different number of calibration images for each coil inside the brain. The MSE for each coil is very small and decreases as the number of calibration images increase, similar to the MSE decreasing outside the brain in the BSENSE magnitude reconstructed images. With fixing $n_{cal} = 30$, Figure A.2b exhibits the MSE for the different acceleration factors for each coil inside the brain. Again, the MSE for each coil is very small with a slight increase as the acceleration factor increases. This illustrates that our BSENSE approach accurately estimates the simulated coil sensitivities as well.

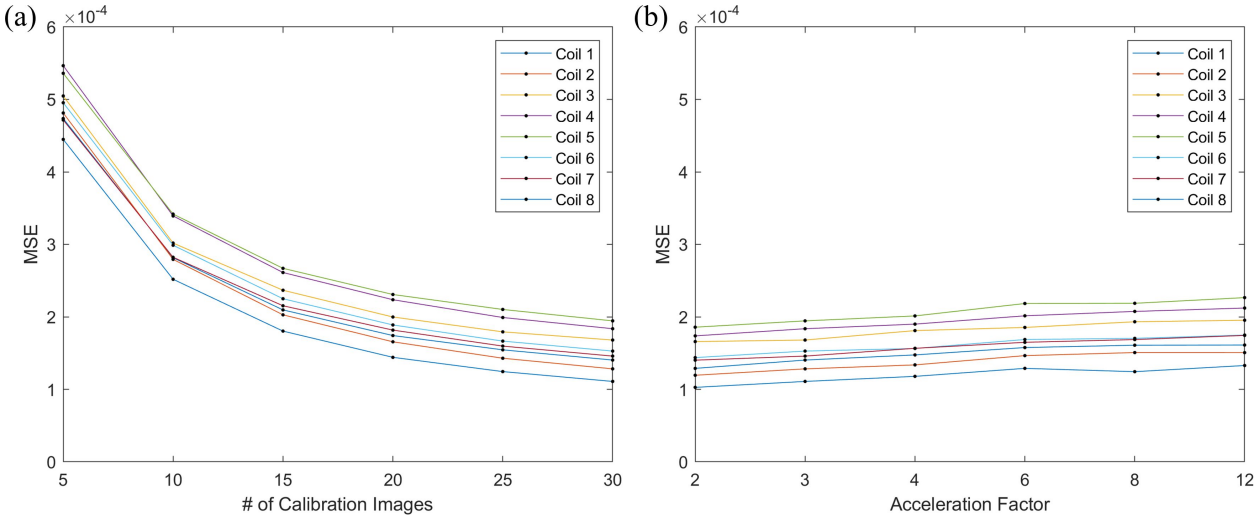

Figure A.2: (a) MSE for each of the $n_C = 8$ coils using a different number of calibration images and (b) MSE for each of the $n_C = 8$ coils using different acceleration factors.

A.2 BSENSE Estimated Residual Noise

Our BSENSE technique also estimated the residual variance for the aliased coil measurements. We evaluated the effects of the number of calibration images and acceleration

factors on the residual variances. Figure A.3a shows the residual variances of the coil measurements for each number of calibration images with $n_A = 3$. The residual variance appears to increase as the number of calibration images increase. This is due to the n_v and n_S scalar coefficients for the estimation of σ^2, outlined in Section 2.3.3, increasing with the number of calibration images. Figure A.3b shows the residual variances of the coil measurements for each acceleration factor with $n_{cal} = 30$. The residual variance appears to decrease as the acceleration factor increases because the denominator of the Iterated Conditional Modes (ICM) estimate of σ^2 (Eq. 2.15) is increasing. All residual variances appear to be uniform across the aliased images in Figure A.3 which is expected as noise is anticipated to be uniform across the image.

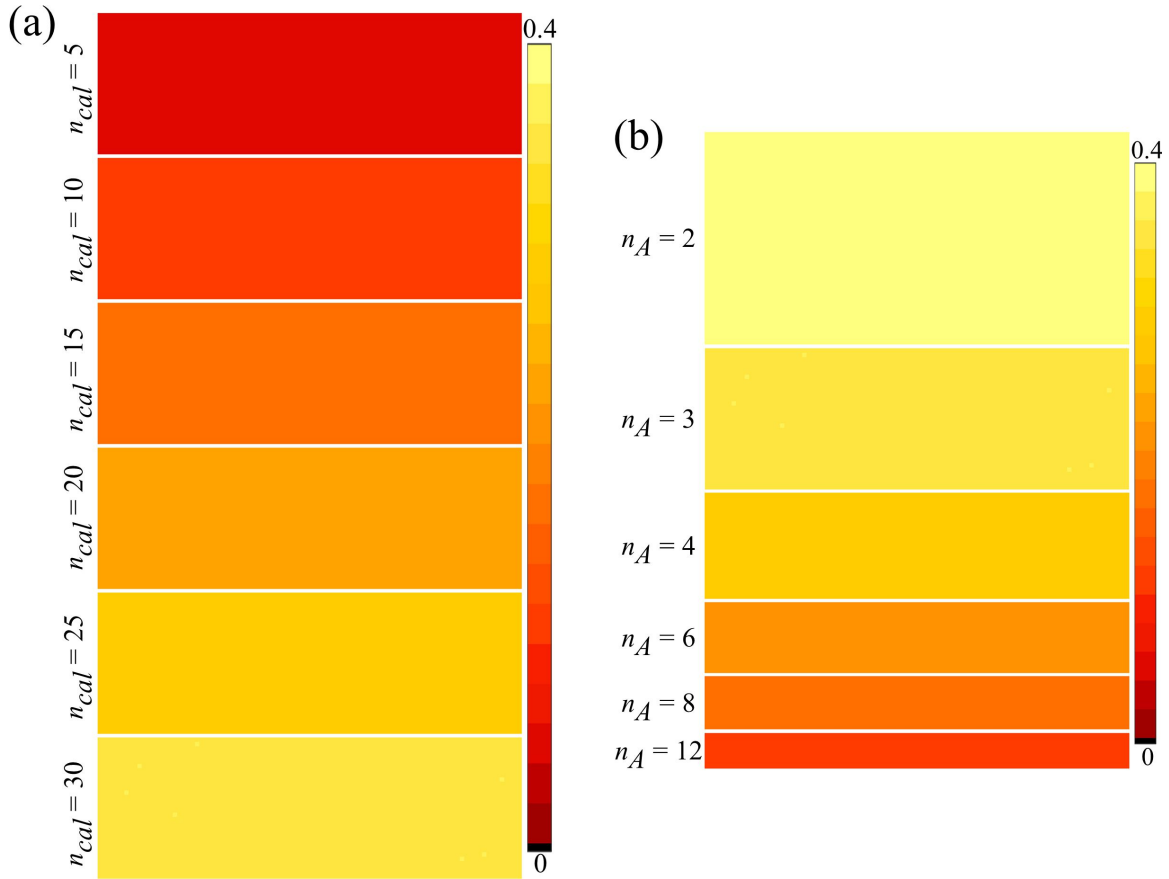

Figure A.3: (a) Residual variance of the aliased coil images for each number of calibration images and (b) Residual variance of the aliased coil images for each acceleration factor.

APPENDIX B

SENSE Coil Sensitivity Information

When estimating prior means for the coil sensitivities H_0, the n_c averaged coil calibration images are first point-wise divided by v_{0M} to obtain a prior mean for the real and imaginary coil sensitivities (as mentioned in Section 2.3.2). The real and imaginary parts are then utilized to estimate the phase by the equation $arctan(I/R)/2$. Dividing the $arctan(I/R)$, which is the equation for converting to polar coordinates, by two incorporates the information from the imaginary component of the coil sensitivities into the reconstructed image while not dividing by two does not.

For SENSE reconstruction, the information for the coil sensitivities uses the phase equal to $arctan(I/R)$ while BSENSE divides the phase by two. This is due to the poor reconstruction results of the experimental data, shown in Figure B.1. The simulated and experimental magnitude and phase reconstructed images at the first TR of the 490 non-task time series using SENSE in Figure B.1 used $n_{cal} = 30$ calibration time points with a $n_A = 3$ acceleration factor. From Figure, B.1, it appears that the magnitude of the SENSE reconstructed simulated image (top left) is unchanged with the $arctan(I/R)/2$ phase coil information. We can also see that using the $arctan(I/R)/2$ improves the phase of the reconstructed simulated image (top right) but is still much more noisy compared to the phase of the BSENSE reconstructed simulated image in Figure 5.5. However, the magnitude of the SENSE reconstructed experimental image (bottom left of Figure B.1) is severely affected by incorporating more imaginary information into the coil sensitivities. The reconstructed image shows unaliasing artifacts strong enough to render the magnitude image unusable. The phase of the SENSE reconstructed experimental image (bottom right) also appears a

little improved, like the simulated phase image, but has much less quality compared to the BSENSE reconstructed phase image in Figure 5.5.

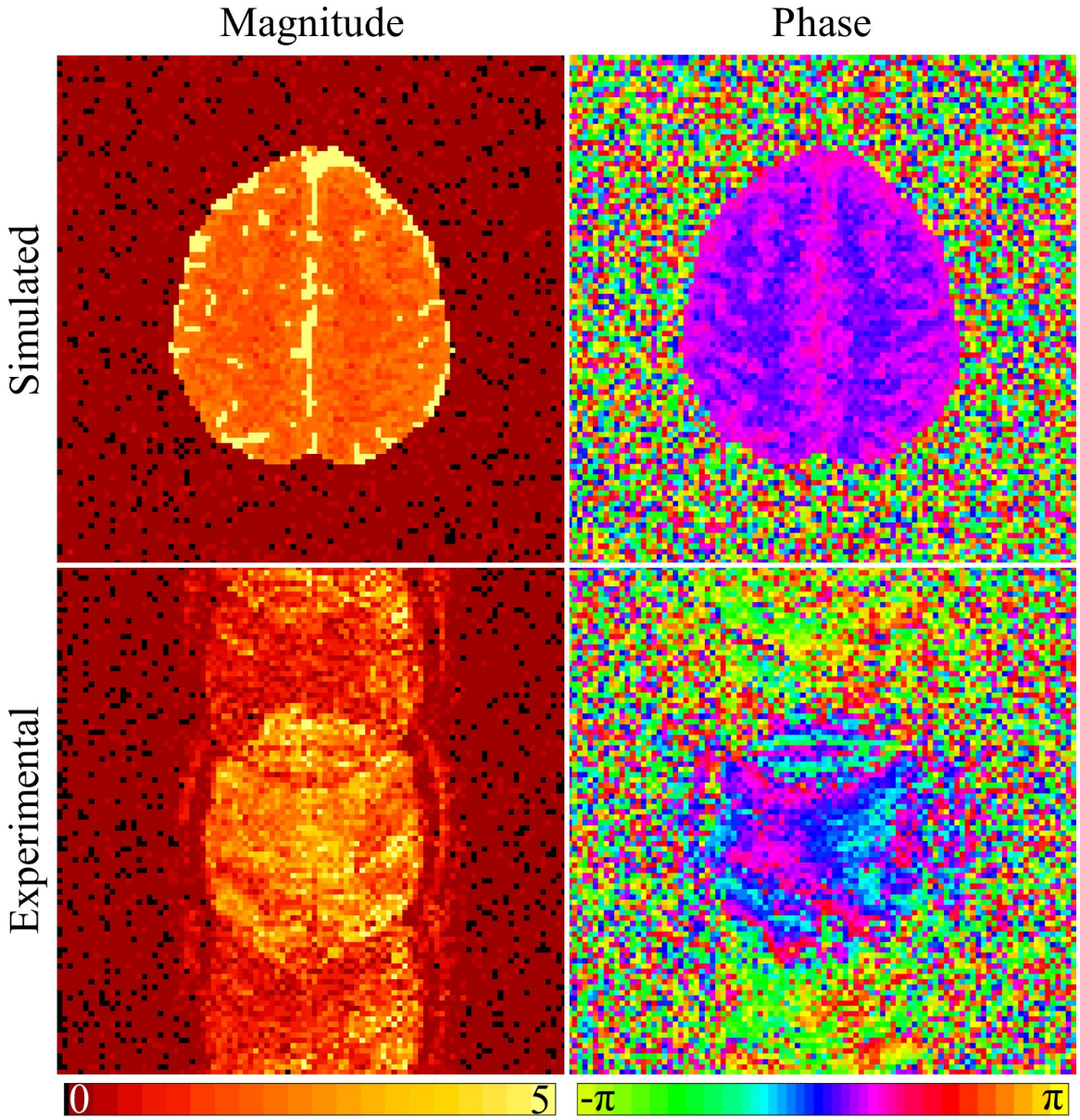

Figure B.1: SENSE simulated magnitude (top left) and phase (top right) reconstructed images and SENSE experimental magnitude (bottom left) and phase (bottom right) reconstructed images with the same coil information used for BSENSE.

These results in Figure B.1 show that SENSE relies on larger numbers of coil sensitivities (Pruessmann et al., 1999) or close to perfect homogeneity between the coils, which is not

realistic. This further indicates that BSENSE can more precisely reconstruct aliased images with decreased temporal variance, increased SNR, and improved task detection compared to SENSE with less information. By using the phase coil information that is not divided by two, we maximize the results for the magnitude of the SENSE reconstruction technique. Even with the maximized results for SENSE, they are still inferior to the BSENSE results as exhibited in Sections 5.1.2, 5.1.5, and 5.2.2.

BIBLIOGRAPHY

Atkinson, D., Hill, D. L. G., Stoyle, P. N. R., Summers, P. E., and Keevil, S. F. (1997). Automatic correction of motion artifacts in Magentic Resonance images using an entropy focus criterion. *IEEE Transactions on Medical Imaging* **16,** 903–910.

Bandettini, P., Jesmanowicz, A., Wong, E., and Hyde, J. S. (1993). Processing strategies for time-course data sets in functional MRI of the human brain. *Magnetic Resonance in Medicine* **30,** 161–173.

Benjamini, Y. and Hochberg, Y. (1995). Controlling the false discovery rate: a practical and powerful approach to multiple testing. *Journal of the Royal Statistical Society, Series B* **57,** 289–300.

Bruce, I. P., Karaman, M. M., and Rowe, D. B. (2011). A statistical examination of SENSE image reconstruction via an isomorphism representation. *Magnetic Resonance Imaging* **29,** 1267–1287.

Bruce, I. P., Karaman, M. M., and Rowe, D. B. (2012). The SENSE-Isomorphism Theoretical Image Voxel Estimation (SENSE-ITIVE) model for reconstruction and observing statistical properties of reconstruction operators. *Magnetic Resonance Imaging* **30,** 1143–1166.

Gelfand, A. E. and Smith, A. F. M. (1990). Sampling-based approaches to calculating marginal mensities. *Journal of American Statistical Association* **85,** 398–409.

Geman, S. and Geman, D. (1984). Stochastic relaxation, Gibbs distributions, and the Bayesian restoration of images. *IEEE Transactions on Pattern Analysis and Machine Intelligence* **6,** 721–741.

Genovese, C. R., Lazar, N. A., and Nichols, T. E. (2002). Thresholding of statistical maps in functional neuroimaging using the false discovery rate. *Neuroimage* **15,** 870–878.

Griswold, M. A., Jamob, P. M., Heidemann, R. M., Nittka, M., Jellus, V., Wang, J., Kiefer, B., and Haase, A. (2002). Generalized autocalibrating artially parallel acquisition (GRAPPA). *Neuroimage* **15,** 870–878.

Hahn, A. D., Nencka, A. S., and Rowe, D. B. (2012). Enhancing the utility of complex-valued functional magnetic imaging detection of neurobiological processes through postacquisition estimation and correction of dynamic B_0 errors and motion. *Human Brain Mapping* **33,** 288–306.

Henkelman, R. M. (1985). Measurement of signal intensities in the presence of noise in MR images. *Medical Physics* **12,** 232–233.

Hyde, J. S., Jesmanowicz, A., Froncisz, W., Kneeland, J. B., Grist, T. M., and Campagna, N. F. (1986). Parallel image acquisition from noninteracting local coils. *Journal of Magnetic Resonance Imaging* **70,** 512–517.

Karaman, M. M., Bruce, I. P., and Rowe, D. B. (2014). A statistical fMRI model for differential T_2* contrast incorporating T_1 and T_2* of gray matter. *Magnetic Resonance Imaging* **32,** 9–27.

Karaman, M. M., Bruce, I. P., and Rowe, D. B. (2015). Incorporating relaxivities to more accurately reconstruct MR images. *Magnetic Resonance Imaging* **33,** 374–384.

King, K. F. and Angelos, L. (2001). SENSE image quality improvement using matrix regularization. *Proceedings of the 9th Annual Meeting of ISMRM* page 1771.

Kornak, J., Young, K., Schuff, N., Du, A., Maudsley, A. A., and Weiner, M. W. (2010). K-Bayes reconstruction for perfusion MRI. I: concepts and application. *Journal of Digital Imaging* **23,** 277–286.

Kumar, A., Welti, D., and Ernst, R. R. (1975). NMR Fourier zeugmatography. *Journal of Magnetic Resonance* **18,** 69–83.

Liang, Z. P., Bammer, R., Ji, J., Pelc, N. J., and Glover, G. H. (2001). Making better SENSE: wavelet denoising, Tikhonov regularization, and total least squares. *Proceedings of the 10th Annual Meeting of the ISMRM* page 2388.

Lin, F. H., Kwong, K. K., Belliveau, J. W., and Wald, L. L. (2004). Parallel imaging reconstruction using automatic regularization. *Magnetic Resonance in Medicine* **51,** 559–567.

Lindley, D. V. and Smith, A. F. M. (1972). Bayes estimates for the linear model. *Journal of the Royal Statistical Society, Series B* **34,** 1–18.

Lindquist, M. A. (2008). The statistical analysis of fMRI data. *Statistical Science* **23,** 439–464.

Liu, B., King, K., Steckner, M., Xie, J., Sheng, J., and Ying, L. (2009). Regularized sensitivity encoding (SENSE) reconstruction using Bregman iterations. *Magnetic Resonance in Medicine* **61,** 145–152.

Logan, B. R. and Rowe, D. B. (2004). An evaluation of thresholding techniques in fMRI analysis. *Neuroimage* **22,** 95–108.

Nencka, A. S., Hahn, A. D., and Rowe, D. B. (2008). The use of three navigator echos in Cartesian EPI reconstruction reduces Nyquist ghosting. *Proceedings of the 16th Annual Meeting of the ISMRM* **3032,**.

Ogawa, S., Lee, T. M., Nayak, A. S., and Glynn, P. (1990). Oxygenation-sensitive contrast in magnetic resonance image of rodent brain at high magnetic fields. *Magnetic Resonance in Medicine* **14,** 68–78.

O'Hagan, A. (1994). *Kendall's Advanced Theory of Statistics, vol. 2B*. Wiley, New York.

Pruessmann, K. P., Weiger, M., Scheidegger, M. B., and Boesiger, P. (1999). SENSE: sensitivity encoding for fast MRI. *Magnetic Resonance in Medicine* **42,** 952–962.

Rowe, D. B. (2005). Modeling both the magnitude and phase of complex-valued fMRI data. *Neuroimage* **25,** 1310–1324.

Rowe, D. B. and Logan, B. R. (2004). A complex way to compute fMRI activation. *Neuroimage* **23,** 1078–1092.

Rowe, D. B., Meller, C. P., and Hoffmann, R. G. (2007). Characterizing phase-only fMRI data with an angular regression model. *Journal of Neuroscience Methods* **161,** 331–341.